Synthesis, Structural and Ferroelectric Properties of Perovskite-Like Layered Structured Materials

Chen Chen

Submitted in partial fulfilment of the requirements of the Degree of Doctor of Philosophy

School of Engineering and Materials Science,

Queen Mary, University of London

London, United Kingdom

August 2015

Declaration

I hereby declare that the present work in prepared solely by myself during the course of my doctoral studies at the Queen Mary, University of London. It has not been submitted anywhere for any award. Work of other people is fully acknowledged according to standard referencing.

This thesis fully complies with the regulations set by the University of London and the Queen Mary, University of London.

Chen Chen

April 2015

Abstract

Perovskite-like layered structured (PLS) compounds display a range of interesting physical and chemical properties, including photocatalysis, photoluminescence, ion conductivity, electrochemical stability, magnetic properties, ferroelectricity and piezoelectricity. There are mainly three homologous series of PLS compounds distinguished by their different BO_6 octahedra orientation: the Dion-Jacobson phase ($A'A_{n-1}B_nO_{3n+1}$); the $A_nB_nO_{3n+2}$ phase; and the hexagonal phase ($A_nB_{n-1}O_{3n}$). Some of the 4-layer $A_nB_nO_{3n+2}$ compounds, like $La_2Ti_2O_7$ and $Sr_2Nb_2O_7$, have been reported to be ferroelectrics with super high Curie point (above 1300 °C), but no ferroelectric properties have been reported for the 2-layer and 3-layer $A_nB_nO_{3n+2}$ compounds, and also there are few reports on the ferroelectric properties of compounds with Dion-Jacobson structure and hexagonal structure. Consequently, in this work, the crystallographic structures, microstructures, dielectric, ferroelectric and piezoelectric properties of $(A_xLa_{1-x})Ti_2O_7$ (A = Sm and Eu) solid solutions with 4-layer $A_nB_nO_{3n+2}$ structure, $Pr_3Ti_2TaO_{11}$ with 3-layer $A_nB_nO_{3n+2}$ structure, $LaTaO_4$ with 2-layer $A_nB_nO_{3n+2}$ structure, $ABiNb_2O_7$ (A = Rb and Cs) with Dion-Jacobson structure and $Sr_6TiNb_4O_{18}$ with hexagonal structure were studied. Spark plasma sintering (SPS) was used to sinter ceramics with high density and preferred orientation. X-ray diffraction refinement (XRD) and transmission electron microscopy (TEM) were used to study the crystallographic structures and microstructures of the layer structured compounds. The ferroelectricity was studied using the current-electric field and polarization-electric field hysteresis loops. The Curie point and phase transitions were studied using the temperature dependence of the dielectric constant and loss. Piezoresponse force microscopy (PFM) was also used to study the ferroelectric domain structure of some layer structured compounds.

Abstract

In the first part of this work, the piezoelectric constant of $La_2Ti_2O_7$ was improved by doping Sm. The crystallographic structure of $(Eu_{1-x}La_x)_2Ti_2O_7$ and $(Sm_{1-x}La_x)_2Ti_2O_7$ solid solutions were well studied. $(A_xLa_{1-x})Ti_2O_7$ solid solutions were isomorphous with $La_2Ti_2O_7$ when x was less than 0.5 for $(Eu_xLa_{1-x})Ti_2O_7$ and 0.8 for $(Sm_xLa_{1-x})Ti_2O_7$. When x was above their solubility limit, a biphase was observed. The XRD and Raman data suggested that the biphase consisted of $(A_xLa_{1-x})_2Ti_2O_7$ perovskite-like layered structure and pure $Sm_2Ti_2O_7$ pyrochlore structure. Ferroelectric domain switching was observed in the *I-E* and *P-E* hysteresis loops for textured $(Sm_xLa_{1-x})Ti_2O_7$ ($x < 0.2$). The highest d_{33} was 2.8 pC/N for $(Sm_{0.1}La_{0.9})Ti_2O_7$.

In the second part, The $Pr_3Ti_2TaO_{11}$ compound was demonstrated to have a 3-layer type II $A_nB_nO_{3n+2}$ PLS structure belonging to space group $Pmc2_1$ with unit cell parameters $a = 3.8689(3)$ Å, $b = 20.389(2)$ Å, $c = 5.5046(5)$ Å, and its ferroelectric properties were investigated. Analysis of the XRD and TEM results showed that $Pr_3Ti_2TaO_{11}$ ceramics have an $n = 3$ (type II) heteroblock structure consisting of alternating $n = 2$ and $n = 4$ octahedral oxide layers. High resolution electron microscopy revealed the layered structure to be highly disordered, with faulting of the heteroblock structure and the coexistence of a $n = 4$ phase on a fine scale (nm), which was evident as a broadening of the XRD peaks of the ceramics. $Pr_3Ti_2TaO_{11}$ ceramic exhibits a super-high Curie point (1415 ± 5 °C). A small, but measurable piezoelectric constant d_{33} between 0.1 and 0.2 pC/N was detected for the samples poled above 900 °C under an electric field of 100~200 V/cm. Pure $LaTaO_4$ powders with orthorhombic phase were be prepared by co-precipitation method. The orthorhombic $LaTaO_4$ powders have a 2-layer perovskite-like layered structure with space group $A2_1am$, which was refined using Rietveld method. The single phase O-$LaTaO_4$ ceramic was prepared using SPS with a slow cooling rate (20 °C/min). A d_{33} of 0.3 pC/N was obtained from the electric field induced orthorhombic phase.

Abstract

In the second part of this work, the ferroelectricity and piezoelectricity of $CsBiNb_2O_7$ with Dion-Jacobson type PLS structure was successfully demonstrated for the first time. The ferroelectricity and piezoelectricity of $RbBiNb_2O_7$, which have similar structure with $CsBiNb_2O_7$, were also fully studied. Highly textured 2-layer Dion-Jacobson ceramics $ABiNb_2O_7$ (A = Rb and Cs) were prepared by one-step SPS. High resolution TEM showed well ordered (0 0 1) lattice planes. Striped ferroelectric domains were observed using PFM. The ferroelectricity and piezoelectricity of $CsBiNb_2O_7$ has been demonstrated for the first time. The T_c of $RbBiNb_2O_7$ and $CsBiNb_2O_7$ are 1098 ± 5 and 1033 ± 5 ℃, respectively. The piezoelectric constant of $RbBiNb_2O_7$ and $CsBiNb_2O_7$ were approximately 5 and 8 pC/N. Thermal depoling studies confirmed the Curie point and the stability of the piezoelectricity. $Sr_6Nb_4TiO_{18}$ ceramics with non-centrosymmetric structure were successfully prepared, but no obvious evidence was found to prove its ferroelectricity. The untextured and textured 6-layer Hexagonal compound $Sr_6Nb_4TiO_{18}$ was prepared by solid state reaction and spark plasma sintering. Its Curie point was found to be greater than 1500 ℃. No ferroelectric properties were observed by studying of I-E and P-E loops, and no d_{33} was observed after poling.

Acknowledgement

I would like to gratefully and sincerely thank my supervisor Professor Dr. Michael John Reece for his understanding, patience, and most importantly, his insightful guidance during my PhD studies at Queen Mary, University of London. As an excellent mentor, he not only helped me to complete my PhD, but also encouraged me to grow as an optimistic research scientist and an independent thinker. I would also like to thank Dr. Haixue Yan, my secondary supervisor. He helped me to obtain the opportunity to study at this great city, London, and introduced me a great supervisor. He also gave me lots of useful suggestions to my work, which helped me to finish my study.

I would specially like to thank Prof. Xiaoyong Wei, Dr Qinghui Jiang, Dr. Huanpo Ning and Dr. Zhipeng Gao for their ideas, discussions and help with my experiments and papers.

I would like to thank Dr. Zofia Luklinsaka, Dr. Rory Wilson and Dr. Isaac Abrahams for their generous help.

I am also grateful to the discussions, ideas, collaboration and friendship provide by members of our ceramics group: Dr. Salvatore Grasso, Dr. Giuseppe Viola, Dr. Baoli Du, Jibran Khaliq, Chuying Yu, Harshit Porwal, Xiaojing Zhu, Ruth Mckinnon, Zheng Li, Kan Chen, Nan Meng, Theo Saunders.

I gratefully acknowledge the funding sources that made my PhD work possible. I was founded by the Chinese Scholarship Council. My work was also partly supported by Meggitt Sensing Systems in Fribourg, Switzerland. I specially acknowledge Bertrand Picon from Meggitt Sensing Systems.

Lastly, I would like to thank my family and friends. Words cannot express how grateful I am to my parents for all the sacrifices that you have made to raise me and make me well educated.

Table of Contents

Chapter I. Introduction

Ferroelectrics, being also pyroelectrics and piezoelectrics, play an important role in sensing technology due to their ability to convert between electrical and mechanical energy.[1] Currently, the best ferroelectrics are lead-containing materials like PZT (lead zirconate titanate). However, due to the toxicity of lead there is a drive to develop lead-free materials to replace them. The most promising lead-free ferroelectrics are based on $BaTiO_3$, $(Na,Bi)TiO_3$, $KNbO_3$-$NaNbO_3$ (KNN) and their modifications.[2-4] However, their relatively low Curie points T_c (< 500 ℃) limits their applications at high temperatures. Materials with stable piezoelectric response at high temperatures are required for sensors in automotive electronics, aerospace, chemical and material processing, and power generating industries.[5, 6] The operational temperature of piezoelectric sensors is limited by their Curie points, at which temperature they transform from a ferroelectric phase to a paraelectric phase and lose their piezoelectric activity. Consequently, for high-temperature sensor applications, lead-free ferroelectric materials with high Curie points are desirable. In the last 50 years, research on high-temperature piezolelectrics has focused on some piezoelectric single crystals, such as $LiNbO_3$, $Sr_2Nb_2O_7$, $GaPO_4$, langasites (with general formula $A_3BC_3D_2O_{14}$) and oxyborate $(ReCa_4O(BO_3)_3)$.[5, 7] However, the high cost and poor mechanical properties of single crystals limit their introduction into commercial applications. Compared with single crystals, the cost of polycrystalline piezoelectrics is lower, and the compositions and properties of polycrystalline piezoelectrics are easier to improve.

Perovskite-like layered structured (PLS) compounds display a range of amazing physical and chemical properties.[5, 8, 9] Generally, the perovskite layers of PLS materials are formed by corner-shared BO_6 octahedra separated by oxygen rich layers. There are mainly three homologous series of PLS compounds according to their different BO_6

octahedra orientation, the Dion-Jacobson type phase ($A'A_{n-1}B_nO_{3n+1}$), the $A_nB_nO_{3n+2}$ type phase and the hexagonal phase ($A_nB_{n-1}O_{3n}$).[9] The $A_nB_nO_{3n+2}$ type PLS materials have been studied recently.[10] Some of them have been shown to be ferroelectrics with super high Curie point, especially the 4-layer $La_2Ti_2O_7$ and $Sr_2Nb_2O_7$, which have Curie point above 1300 ℃ and reasonable piezoelectric constant d_{33} (between 2 to 3 pC/N).[7, 11, 12] But materials with Dion-Jacobson structure and Hexagonal structure have been seldom reported to present ferroelectricity.

The previous work in our group has studied the ferroelectric and dielectric properties of 4-layer $A_2B_2O_7$ type PLS ceramics. Super high Curie point and piezoelectric constant d_{33} were obtained from some compounds, such as $Nd_2Ti_2O_7$ (T_c = 1482±5 ℃), $Ca_2Nb_2O_7$ (T_c > 1525 ℃), $La_2Ti_2O_7$ (T_c = 1461±5 ℃, d_{33} = 2.6 pC/N) and $Sr_2Nb_2O_7$ (T_c = 1327±5 ℃, d_{33} = 2.8±0.2 pC/N).[7, 12, 13] The previous work was mainly focused on the rare-earth titanates $Ln_2Ti_2O_7$ (Ln = La, Ce, Pr, Nd). $Ln_2Ti_2O_7$ crystals have a perovskite-like layered structure with polar symmetry and could have ferroelectric properties only when Ln is between La and Nd. $Ln_2Ti_2O_7$ (Ln = Sm, Eu, …, Lu) crystals have a pyrochlore structure, which belongs to the centrosymmetric group $Fd3m$ and do not have ferroelectric properties.[9, 14] As $La_2Ti_2O_7$ has the perovskite-like layered structure and $Eu_2Ti_2O_7$ and $Sm_2Ti_2O_7$ have the pyrochlore structure, it is interesting to investigate the phase stability of the $(Eu_{1-x}La_x)_2Ti_2O_7$ and $(Sm_{1-x}La_x)_2Ti_2O_7$ solid solutions, then to study the ferroelectric and piezoelectric properties of those solid solutions with perovskite-like layered structure.

Some of the 4-layer $A_2B_2O_7$ PLS compounds are well known to be ferroelectrics, but the 3-layer $A_3B_3O_{11}$ compounds and 2-layer ABO_4 are largely unexplored and it has not yet been demonstrated if they are ferroelectrics. For n = 3 compounds, there are two different types of structure. The n = 3 (I) structure is made up of blocks of three

identical octahedral perovskite layers. In contrast, the $n = 3$ (II) structure is a heteroblock structure made up of alternating blocks of two and four perovskite layers (i.e. effectively alternating between $n = 2$ and $n = 4$ blocks).[9] The two different types of 3-layer $A_3B_3O_{11}$ compounds ($Sr_2LaTa_3O_{11}$ type I, $La_3Ti_2TaO_{11}$ type II) were first reported by Titov *et al.*.[15-17] According to their work, based only on powder diffraction, the $n = 3$(I) structure belongs to a centrosymmetric space group (*Immm*), while the $n = 3$(II) structure belongs to a non-centrosymmetric group (*Pmc*2_1 or *P2cm*), which possibly suggests that only compounds with $n = 3$(II) structure may exhibit ferroelectric properties. However, no information on the microstructure and ferroelectric properties of ceramics of $n = 3$(II) type compounds has been reported.

Present work focuses on understanding the crystallographic structure and ferroelectric properties of materials with perovskite-like layered structure. This work is divided into three parts. The first part is to improve the ferroelectric properties of $La_2Ti_2O_7$, which is the mostly studied 4-layer $A_nB_nO_{3n+2}$ type PLS compounds, by doping Sm and Eu. Meanwhile, it is necessary to understand the crystallographic structure of $(Eu_{1-x}La_x)_2Ti_2O_7$ and $(Sm_{1-x}La_x)_2Ti_2O_7$ solid solutions. The second part is to explore the ferroelectric properties of compounds with 2-layer and 3-layer $A_nB_nO_{3n+2}$ type PLS structure. The last part of this work is to demonstrate the ferroelectric properties of materials with the other two type of PLS structure (the Dion-Jacobson phase and Hexagonal phase), which have been reported to have the potential to be ferroelectrics, but no evidences have been reported.

Chapter II. Literature Review

2.1 Background of Ferroelectrics

All crystals can be divided into 32 crystal point groups by using different symmetry elements, such as centre of symmetry, axes of rotation, mirror planes and their combinations. Among the 32 point groups, 21 groups are non-centrosymmetric, which is necessary for the existence of piezoelectricity. Excluding the point group 432, the remaining 20 non-centrosymmetric groups can present piezoelectric properties, and 10 of them exhibit spontaneous polarization, which means that they are pyroelectrics. The difference between ferroelectrics and pyroelectrics is that the spontaneous polarization of ferroelectrics can be reversed by applying an external electric field. Thus, all ferroelectrics are also pyroelectrics, and all pyroelectrics are piezoelectrics. The two important characteristics of ferroelectrics are the presence of spontaneous polarization and reversibility of the polarization under external electric field.[18-20]

In 1921, ferroelectricity was first discovered in Rochelle salt (potassium sodium tartrate tetrahydrate, $KNa(C_4H_4O_6) \cdot 4H_2O$), but the applications on its ferroelectric properties is largely limited due to its water solubility.[19, 21] During the early to mid-1940s, the discovery of barium titanate ceramic ($BaTiO_3$) provided the possibility to use ferroelectric materials in commercial applications. With the discovery of new ferroelectric materials and the development of science and technology, the ferroelectric phenomenon has been applied to many industrial and commercial applications, such as capacitors, dynamic random access memories (DRAM), thermistors, electro-optic materials for data storage applications, switches known as transchargers or transpolarizers, pyroelectric detectors and sensors, piezoelectrics for ultrasound imaging and actuators.[5, 6, 19, 22-24]

So far a number of materials have been reported to possess ferroelectric properties. Fig. 2.1.1 shows the dielectric and piezoelectric properties of some typical ferroelectric ceramics. Ferroelectrics like PZT and their modifications have been widely used as actuators, sensors, and transducers in some low temperature (< 400 ℃) industrial applications.[23] Ferroelectrics with Aurivillius structure $((Bi_2O_2)(A_{n-1}B_nO_{3n+1}))$ and perovskite-layered structure have been found to have the highest Curie points as shown in Fig. 2.1.1. According to the recent report,[7, 12] ferroelectrics with perovskite-layered structure show much higher Curie points and more stable electrical properties below their Curie points than Aurivillius ferroelectrics.
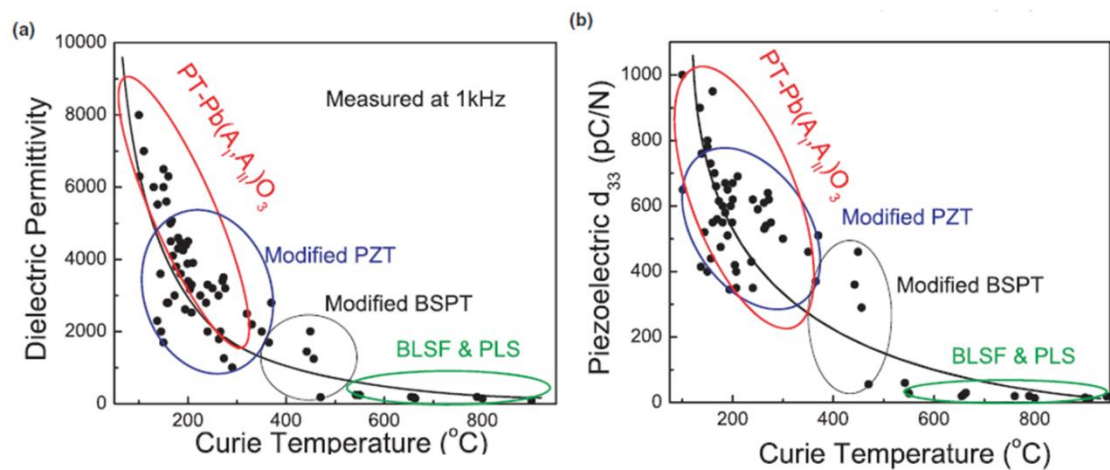

Fig. 2.1.1 Dielectric permittivity (a) and piezoelectric coefficient d_{33} (b) as a function of Curie point for ferroelectric ceramics: PT ($PbTiO_3$); PZT ($Pb(Zr,Ti)O_3$); BSPT (Mn modified $BiScO_3$-$PbTiO_3$); BLSF (Aurivillius structure); PLS (perovskite-layered structure).[5]

2.2 Perovskite-like Layered Structured Compounds

Perovskite-like layered structured (PLS) compounds display a range of interesting physical and chemical properties, including photocatalysis, photoluminescence, ion conductivity, electrochemical stability, magnetic properties, ferroelectricity and piezoelectricity.[5, 8, 9, 25-27] Fig 2.2.1 shows the sketch of the idealized crystal structure of the three homologous series PLS compounds. The subscript n in the formulas means the number of BO_6 octahedra layers contained in each perovskite layer. All of the three structures have the idealized perovskite structure when n is equal to infinity. As shown in Fig 2.2.1, the crystal structure of Dion-Jacobson phase can be regarded as a result of cutting the idealized perovskite structure across the $(1\ 0\ 0)_{perovskite}$ plane, and the crystal structure of $A_nB_nO_{3n+2}$ phase and the hexagonal phase can be regarded as a result of cutting the perovskite structure across the $(1\ 1\ 0)_{perovskite}$ and $(1\ 1\ 1)_{perovskite}$ planes, respectively.[8, 9, 14] Some of the $A_2B_2O_7$ ($A_nB_nO_{3n+2}$, $n = 4$) materials, such as La$_2$Ti$_2$O$_7$ [7, 11], Sr$_2$Nb$_2$O$_7$ [10, 12, 13], Nd$_2$Ti$_2$O$_7$ [7] and Ca$_2$Nb$_2$O$_7$ [12, 28], were reported to be ferroelectrically and piezoelectrically active with super-high Curie point (>1300 ℃), and have good thermal stability at high temperature, which makes them one of the promising materials for high-temperature sensing applications. Materials with Dion-Jacobson and Hexagonal structure have seldom been reported to be non-centrosymmetric and present ferroelectricity.[29, 30]
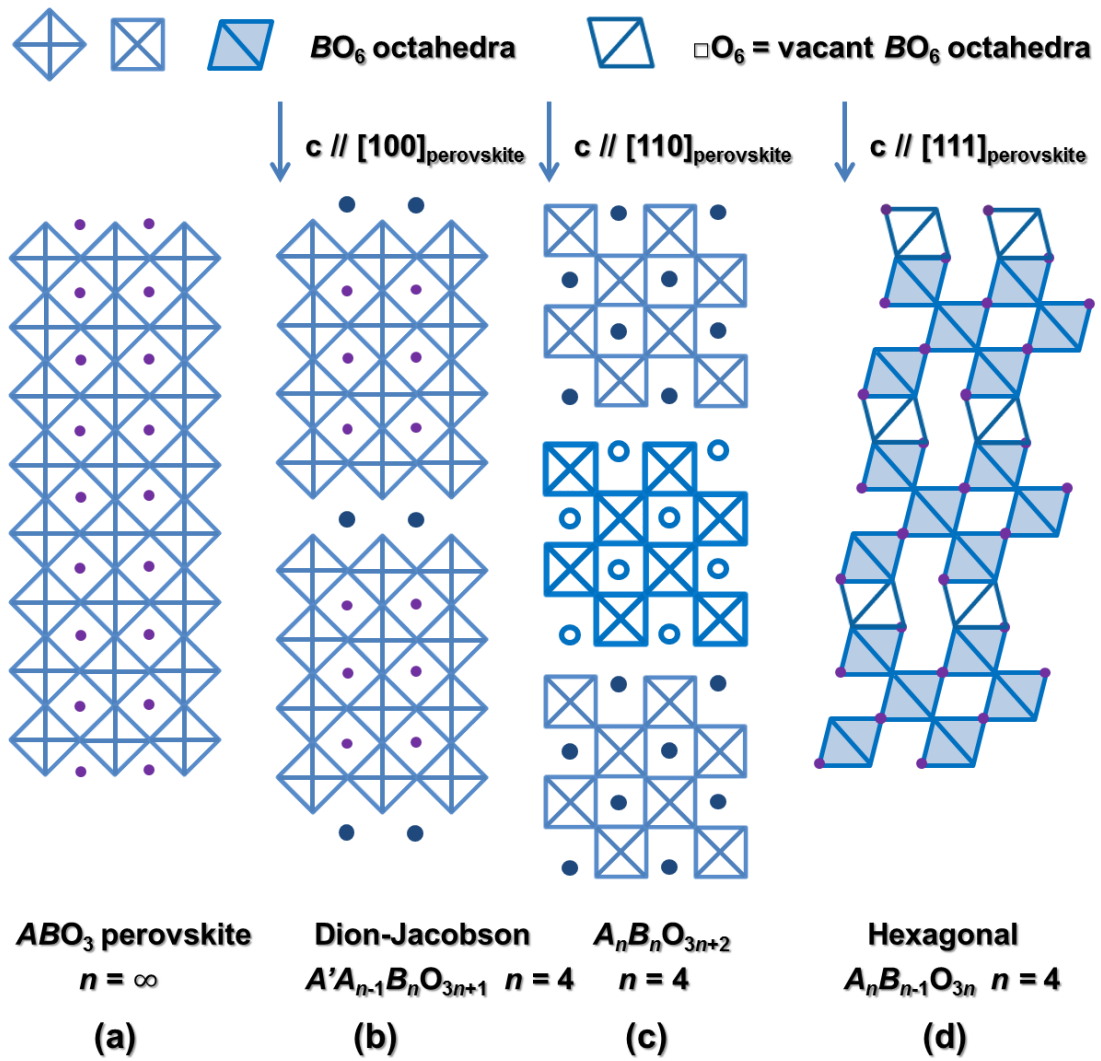
Fig. 2.2.1 Schematic representation of the idealized crystal structure of the PLS materials.

2.3 $A_nB_nO_{3n+2}$ Compounds

For the $A_nB_nO_{3n+2}$ structure, A sites can be occupied by Na^+, Ca^{2+}, Sr^{2+}, Cd^{2+}, La^{3+}-Sm^{3+}, and B sites can be occupied by Ga^{3+}, Fe^{3+}, Cr^{3+}, Al^{3+}, Ti^{4+}, Nb^{5+}, Ta^{5+}.[15-17] Fig. 2.3.1 and 2.3.2 show sketches of the $A_nB_nO_{3n+2}$ structure when n equals 2, 3, 4, 4.5, 5, 6, and ∞. The $n = 2$, 4, 5 and 6 $A_nB_nO_{3n+2}$ structures consist of identical perovskite-like layers. The $n = 4.5$ structure consists of an ordered stacking sequence of perovskite-like layers with different thickness ($n = 4$ and $n = 5$). For the $n = 3$ structures there are two different types: type I and type II. The type I structure is made up of blocks of three identical perovskite-like layers which is similar to the $n = 2$, 4, 5 and 6 structures. The type II structure is a heteroblock structure made up of alternating blocks of two and four octahedral perovskite-like layers.[8, 9]

As mentioned in chapter 2.2, some 4-layer $A_nB_nO_{3n+2}$ materials, e.g. $La_2Ti_2O_7$, present ferroelectricity and piezoelectricity with super-high Curie point (>1300 °C). However, there are few reports of ferroelectricity for $A_nB_nO_{3n+2}$ compounds when n equals 2, 3, 5, 6 or more than 6. One important characteristic of ferroelectric materials is their non-centrosymmetric structures. Table 2.3.1 shows the symmetry of some compounds with $A_nB_nO_{3n+2}$ structures. It seems to be a general rule that the uneven types $n = 3$ (I), $n = 5$, and $n = 7$ have centrosymmetric structures, and the even types $n = 2$, $n = 3$ (II), $n = 4$, and $n = 6$ have non-centrosymmetric structures, which means that they have the potential to present ferroelectricity.[9]

$\boxtimes$ = BO_6 octahedra (O located at the corners, B hidden in the center)

• A

b

$c \parallel [110]_{perovskite}$

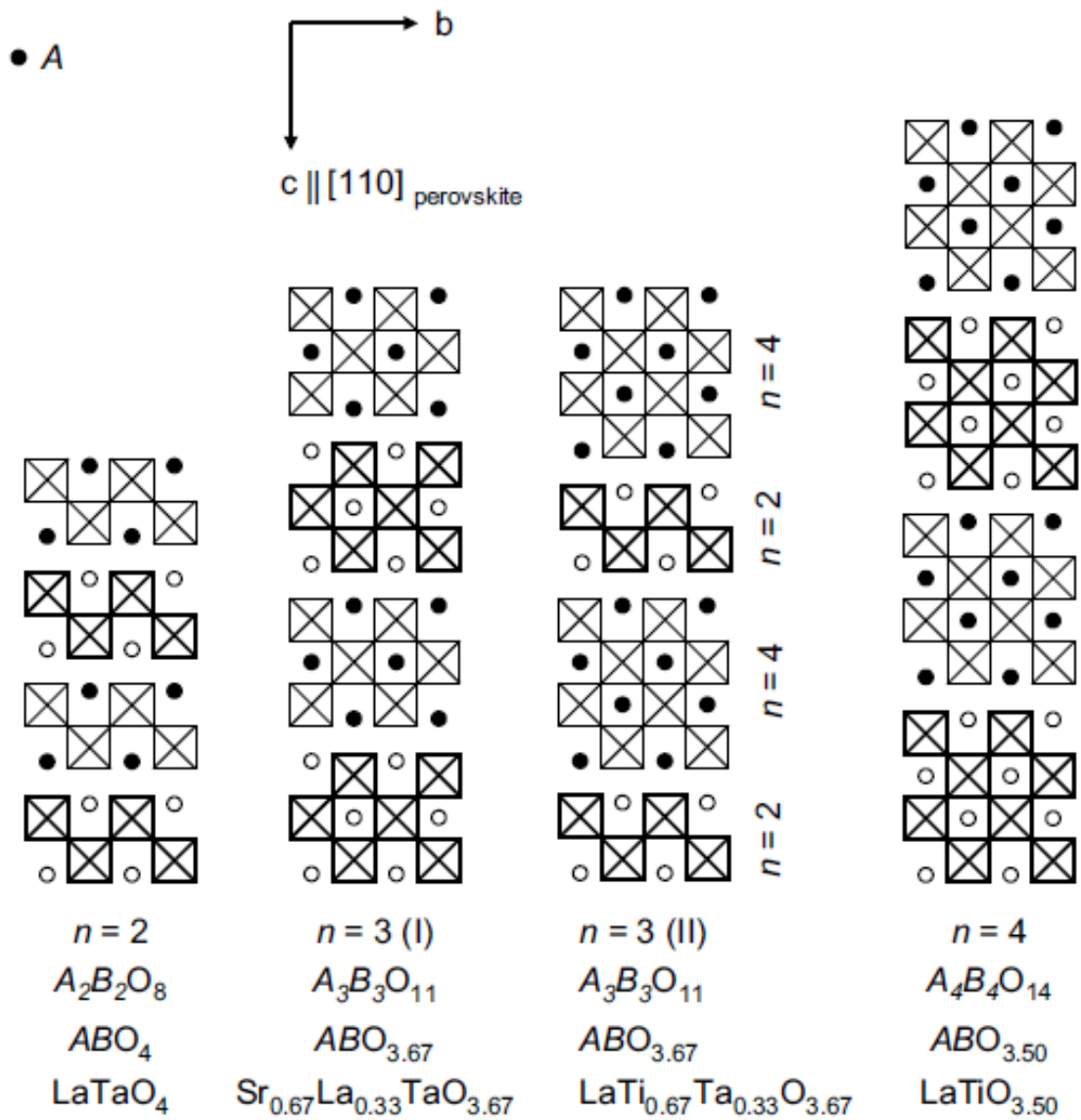| $n = 2$	$n = 3$ (I)	$n = 3$ (II)	$n = 4$
$A_2B_2O_8$	$A_3B_3O_{11}$	$A_3B_3O_{11}$	$A_4B_4O_{14}$
ABO_4	$ABO_{3.67}$	$ABO_{3.67}$	$ABO_{3.50}$
$LaTaO_4$	$Sr_{0.67}La_{0.33}TaO_{3.67}$	$LaTi_{0.67}Ta_{0.33}O_{3.67}$	$LaTiO_{3.50}$

Fig. 2.3.1 Schematic representation of the idealized crystal structures of the $n = 2$, 3, and 4 members of the $A_nB_nO_{3n+2}$ type structures.[9]
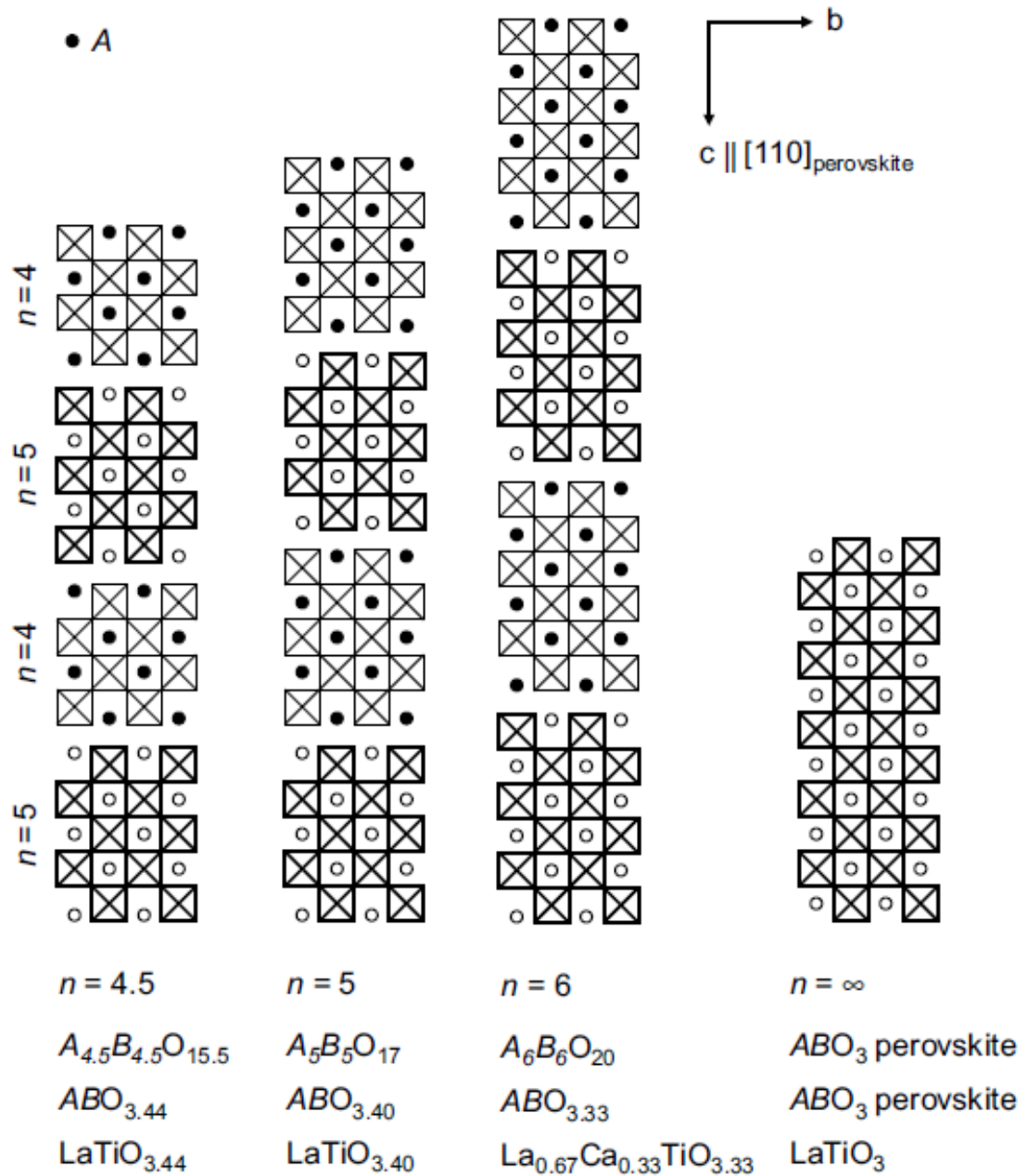
Fig. 2.3.2 Schematic representation of the idealized crystal structures of the $n = 4.5, 5, 6,$ and ∞ members of the $A_nB_nO_{3n+2}$ type structures.[9]

Table 2.3.1 Symmetry of some compounds with $A_nB_nO_{3n+2}$ structures.

Compounds	n	Space group	Symmetry
LaTaO$_4$[31, 32]	2	$P2_1/c$ (room temperature)	Centrosym.
		$A2_1am$ (>175 ℃)	Non-centrosym.
La$_3$Ti$_2$TaO$_{11}$[15, 16]	3 (II)	$Pmc2_1$	Non-centrosym.
Sr$_2$LaTa$_3$O$_{11}$[17]	3 (I)	$Immm$	Centrosym.
La$_4$Ti$_4$O$_{14}$[11]	4	$P2_1$	Non-centrosym.
Sr$_{4.5}$Nb$_4$Ti$_{0.5}$O$_{15.5}$[9]	4.5	$P2_1/c$	Centrosym.
Sr$_5$Nb$_5$O$_{17}$[9, 33]	5	$Pnnm$	Centrosym.
Sr$_6$Nb$_4$Ti$_2$O$_{20}$[34]	6	$Cmc2_1$	Non-centrosym.
Sr$_7$Nb$_4$Ti$_3$O$_{23}$[9]	7	$Pnnm$	Centrosym.

2.3.1 $A_2B_2O_7$ Compounds

There have been a number of publications in recent years on $A_2B_2O_7$ (4-layer $A_nB_nO_{3n+2}$) compounds, such as Sr$_2$Nb$_2$O$_7$ and La$_2$Ti$_2$O$_7$, because these compounds represent the ferroelectrics with the highest T_c, which gives them the potential to be used in high temperature sensors, especially in the aerospace industry.[35] Table 2.3.2 shows the structures and properties of some reported $A_2B_2O_7$ compounds. Most of them with non-centrosymmetric structures show super-high Curie point (>1300 ℃), which are much higher than that of other types of ferroelectrics. Because of their high Curie point, their coercive field are also very high, this means that they are difficult to pole to present

piezoelectric properties. As shown in Table 2.3.2, $Sr_2Nb_2O_7$ and $La_2Ti_2O_7$ have a small

piezoelectric constant d_{33}.

Table 2.3.2 Summary of the structures and properties of some $A_2B_2O_7$ compounds.

Compounds	Space Group	Structure (room temperature)	T_c (°C)	d_{33} (pC/N)
$Sr_2Nb_2O_7$[12]	$Cmc2_1$	Orthorhombic	1327±5	2.8±0.2
$Ca_2Nb_2O_7$[12]	$P2_1/Pbn2_1$	Monoclinic/ orthorhombic	>1525	/
$La_2Ti_2O_7$[7, 11]	$P2_1/Pbn2_1$	Monoclinic/ orthorhombic	1461±5	2.6±0.2
$Pr_2Ti_2O_7$[36]	$P2_1$	Monoclinic	>1555	0.5±0.1
$Nd_2Ti_2O_7$[7]	$P2_1$	Monoclinic	1482±5	/
$Sm_2Ti_2O_7$[37]	$Fd3m$	Cubic	N/A	N/A
	$P2_1$	Monoclinic (HPM) [38, 39]	1077	/
$Eu_2Ti_2O_7$[40]	$Fd3m$	Cubic	N/A	N/A
	$P2_1$	Monoclinic (HPM) [38, 39]	1247	/

*HPM-high pressure modification

(a) La$_2$Ti$_2$O$_7$

The piezoelectricity and ferroelectricity of $La_2Ti_2O_7$ were first discovered in single

crystals by Kimura and Nanamatsu *et al*. between 1972 and 1974.[11, 41] Some typical

piezoelectric and ferroelectric properties of single crystal $La_2Ti_2O_7$ are shown in Table

2.3.3. The ferroelectric polarization was determined from the *D-E* hysteresis loop shown in Fig. 2.3.3(a). Ferroelectric domains were also observed from the etched crystal (Fig.2.3.3(b)). The Curie point was determined as 1500 ℃ by a dielectric anomaly in dielectric constant ε_{22}.

Table 2.3.3 Piezoelectric and ferroelectric properties of sing crystal $La_2Ti_2O_7$.[11, 41]

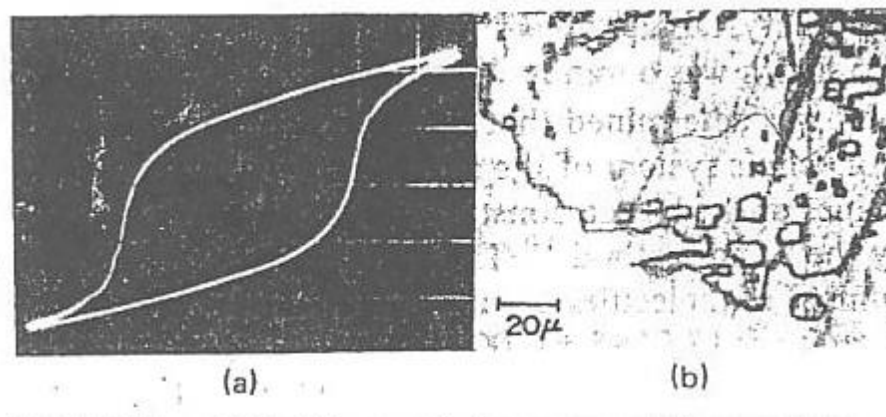| Properties	$La_2Ti_2O_7$
Eletromechanical coupling factor k_{22}	0.29
Piezoelectric constant d_{22} (pC/N)	16
Spontaneous polarization P_s ($\mu C/cm^2$)	5
Coercive field E_c (kV/cm)	45
Curie point T_c (℃)	1500

Fig. 2.3.3 (a) *D-E* hysteresis loop at room temperature under 50 Hz, and (b) ferroelectric domain pattern in *c*-plate of single crystal $La_2Ti_2O_7$.[11]

$La_2Ti_2O_7$ has a ferroelectric phase at room temperature, which belongs to the monoclinic space group $P2_1$ with lattice constants $a = 0.781$ nm, $b = 1.302$ nm, $c = 0.555$ nm, and γ

= 98.43 °. Its spontaneous polarization is along its *c*-axis. Fig. 2.3.4(a) and (b) show the monoclinic structure of $La_2Ti_2O_7$ projected along the [1 0 0] and [0 0 1] directions, respectively. The structure contains parallel slabs, which are characterized by four corner-shared and distorted TiO_6 octahedra layers and 12-coordinated La^{3+} cations. The slabs are linked by a cleavage plane parallel to the (0 1 0) plane. Above its Curie point (~1500 °C), $La_2Ti_2O_7$ has a paraelectric phase, which belongs to the orthorhombic space group *Cmcm* shown in Fig. 2.3.5. There is another phase transition from monoclinic *P2*₁ ferroelectric phase to orthorhombic *Cmc2*₁ ferroelectric phase at approximately 780 °C.[42] The connection between the orthorhombic *Cmc2*₁ ferroelectric phase and orthorhombic *Cmcm* paraelectric phase is shown in Fig. 2.3.5. When a deformation and slight rotation of the TiO_6 octahedra is applied along the *x*-axis of the *Cmcm* structure, the mirror planes perpendicular to the *z*-axis are destroyed and a two-fold screw axis along *z*-axis is formed.[42]
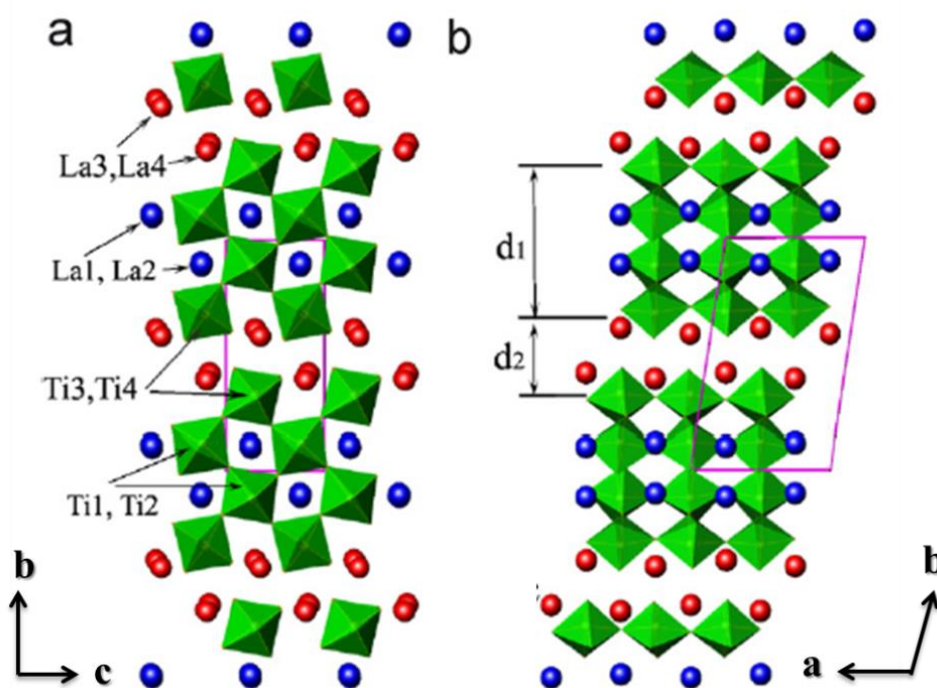

Fig. 2.3.4 The crystal structure of monoclinic (*P2*₁) $La_2Ti_2O_7$.[43]
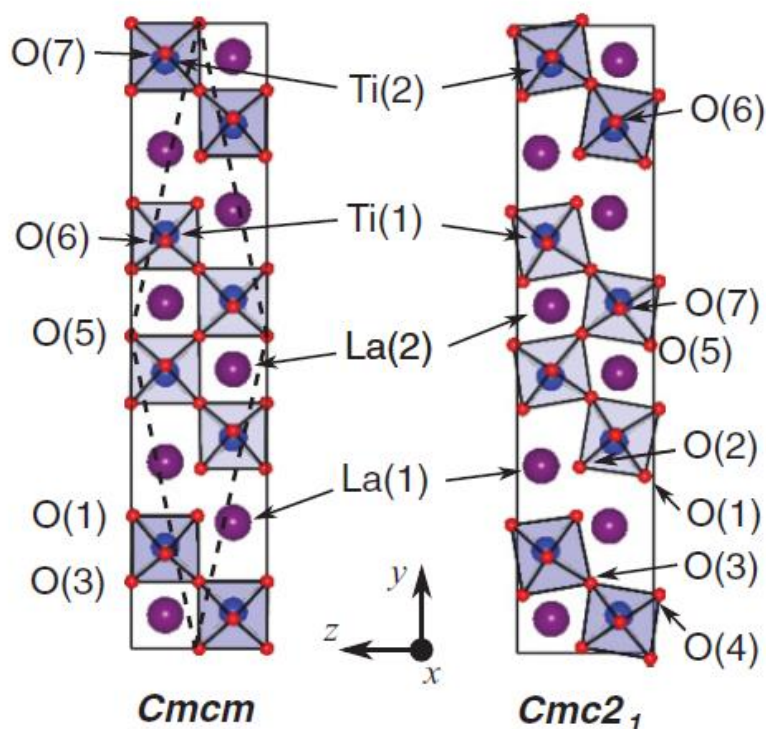
Fig. 2.3.5 The crystal structure of orthorhombic (*Cmcm* and *Cmc2*$_1$) La$_2$Ti$_2$O$_7$.[44]

Ferroelectricity in polycrystalline La$_2$Ti$_2$O$_7$ has been investigated in recent years. But due to the high coercive field E_c caused by the structure and highly randomly orientated grains, it is difficult to pole the ceramics to present ferroelectric and piezoelectric properties. One efficient method to reduce the coercive field of ferroelectric ceramics with randomly orientated grains is to texture them. Some texturing techniques, such as template grain growth,[45] hot forging,[46] and two-steps SPS method[7] have been used to improve the properties of La$_2$Ti$_2$O$_7$ ceramics. As shown in Fig 2.3.6, plate-like La$_2$Ti$_2$O$_7$ grains are highly oriented in the plane parallel the pressing direction. The ferroelectric polarization of La$_2$Ti$_2$O$_7$ is perpendicular to the thickness of its plate-like grains (*b*-axis). Domain switching is within the *a-c* plane in a single grain. This is why the orientated ceramics have a lower coercive field and higher remnant polarization along the direction perpendicular to the pressing direction. The piezoelectric and ferroelectric properties of

textured $La_2Ti_2O_7$ ceramic were first demonstrated by Yan, *et al.*[7] They used polarization-electric field (*P-E*) and current-electric field (*I-E*) hysteresis loops (Fig. 2.3.7) to show its ferroelectricity. The small peaks marked in the *I-E* loop are produced by the ferroelectric domain switching. The piezoelectric and ferroelectric properties of textured $La_2Ti_2O_7$ ceramics are shown in Table 2.3.4.
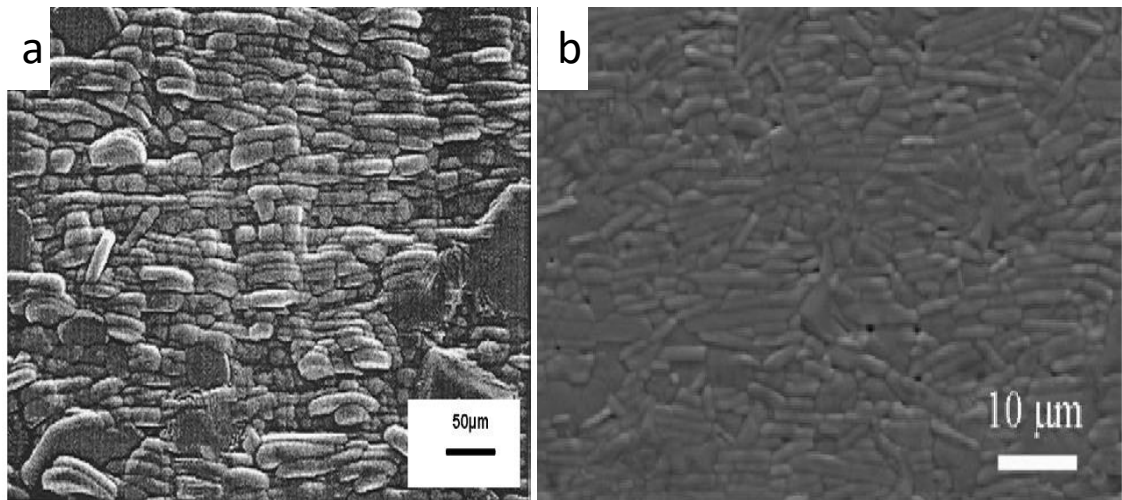

Fig. 2.3.6 SEM micrographs of the textured $La_2Ti_2O_7$ ceramics: (a) prepared by hot-forging method (plane parallel to hot-forging axis), [46] (b) prepared by two-step SPS (plane perperndicular to the SPS pressing direction).[7]
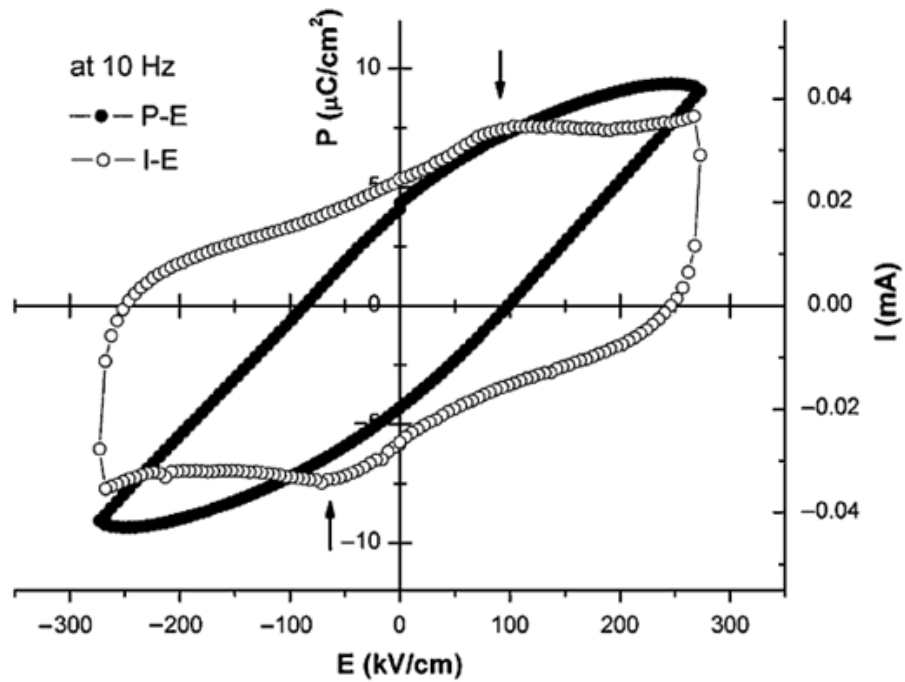
Fig. 2.3.7 Polarization-electric field (*P-E*) and current-electric field (*I-E*) hysteresis loops at

200 ℃ under 10 Hz along the direction perpendicular to the pressing directon for textured

$La_2Ti_2O_7$ ceramic [7].

Table 2.3.4 Piezoelectric and ferroelectric properties of textured $La_2Ti_2O_7$ ceramics.[7]

Properties	$La_2Ti_2O_7$
Lotgering factor of (*0k0*) planes	0.8
Spontaneous polarization P_s ($\mu C/cm^2$)	4
Coercive field E_c (kV/cm)	100
Curie point T_c (℃)	1461 ±5
Piezoelectric constant d_{33} (pC/N)	2.6 ±0.1

(b) $Eu_2Ti_2O_7$ and $Sm_2Ti_2O_7$

As shown in Table 2.3.2, $Eu_2Ti_2O_7$ and $Sm_2Ti_2O_7$ have the Cubic pyrochlore structure (*Fd*3*m*) at room temperature. $Ln_2Ti_2O_7$ (*Ln* represents the lanthanide metals) compounds have a PLS structure when *Ln* is between La and Nd, but when *Ln* is between Sm and Lu, they have a pyrochlore structure.[9, 47, 48] According to some reports,[37, 39, 49] the pyrochlore structured $Eu_2Ti_2O_7$ and $Sm_2Ti_2O_7$ ceramics can convert into a PLS modification under high pressure. Bocquillon *et al*. reported that the pyrochlore structured $Sm_2Ti_2O_7$ converted into the PLS modification under high pressure, 5.4 GPa at 1663 K.[39] Sych *et al*. reported that the pyrochlore structured $Eu_2Ti_2O_7$ converted into the PLS modification under high pressure, 8 GPa at 2020 K.[39] The P_s and T_c of high-pressure PLS $Sm_2Ti_2O_7$ and $Eu_2Ti_2O_7$ modifications at room temperature were estimated to be 2.1 $\mu C/cm^2$ (1350 K) and 2.7 $\mu C/cm^2$ (1520 K), respectively.[39]

Nathaniel *et al*. reported a low-temperature ambient-pressure method to synthesize the PLS modification of $Eu_2Ti_2O_7$.[50] Fig. 2.3.8 shows the synthesis process. The simple perovskite $EuTiO_3$ was used as a structural precursor. At first, $EuTiO_3$ was heated in air, it initially formed an amorphous intermediate phase (Fig. 2.3.8b), which is shown between 475 and 650 ℃. At 750 ℃, the PLS modification of $Eu_2Ti_2O_7$ began to crystallize, and it was stable up to 800 ℃. The reason for the formation of the PLS $Eu_2Ti_2O_7$ is as following: during heating in air, the Eu^{2+} ions in $EuTiO_3$ are oxidized into Eu^{3+} ions, and O^{2-} ions intercalates into the structure. The product $Eu_2Ti_2O_7$ retains the perovskite-like structure defined by the $EuTiO_3$ precursor and allows the crystallization of the PLS modification of $Eu_2Ti_2O_7$ before the formation of the more stable pyrochlore modification. By 900 ℃, impurities of pyrochlore $Eu_2Ti_2O_7$ were observed in the XRD results, and the sample converted entirely into the pyrochlore modification above 1000 ℃ (Fig. 2.3.8b). Thus, by using $EuTiO_3$ as a structural

precursor, the formation of pyrochlore $Eu_2Ti_2O_7$ is suppressed during the heating process, providing a narrow temperature window in which the PLS modification is stable at ambient pressure.[50]
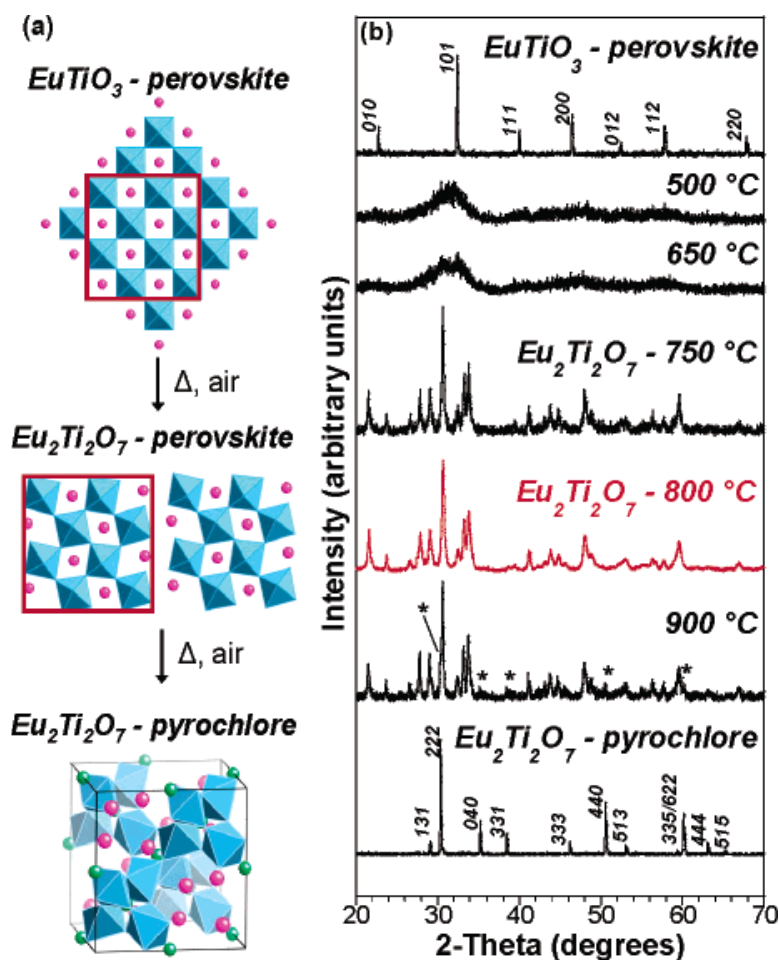
Fig. 2.3.8 (a) Overview of the ambient-pressure synthetic pathway: The light blue polyhedra represent TiO_6 octahedra, and the pink spheres represent Eu cations; In the pyrochlore structure, oxygen atoms that are not part of the TiO_6 octahedra are shown as green spheres. (b) Powder XRD data for the $EuTiO_3$ precursor, the amorphous perovskite-related intermediate (500 and 650 °C), the crystallization of perovskite-like $Eu_2Ti_2O_7$ (750, 800, and 900 °C), and the stable $Eu_2Ti_2O_7$ pyrochlore phase that forms at higher temperatures.[50]

Shao *et al.* recently reported the structure and photoluminescent properties of solid solutions between $La_2Ti_2O_7$ and $Sm_2Ti_2O_7$.[48] $(La_{1-x}Sm_x)_2Ti_2O_7$ solid solutions were synthesized by a sol-gel method. Fig. 2.3.9 shows the XRD patterns of $(La_{1-x}Sm_x)_2Ti_2O_7$ (x = 0-1) powders. Because $La_2Ti_2O_7$ has a PLS structure and $Sm_2Ti_2O_7$ has a pyrochlore structure, complete solid solution cannot be formed between them. As shown in Fig. 2.3.9, no additional peaks can be observed for $(La_{1-x}Sm_x)_2Ti_2O_7$ (0<x<0.8), which means that the solid solutions continue the PLS structure of $La_2Ti_2O_7$ ($P2_1$). When x is between 0.8 and 1, a biphase structure is formed between the $La_2Ti_2O_7$-like PLS phase and the pyrochlore $Sm_2Ti_2O_7$ phase.

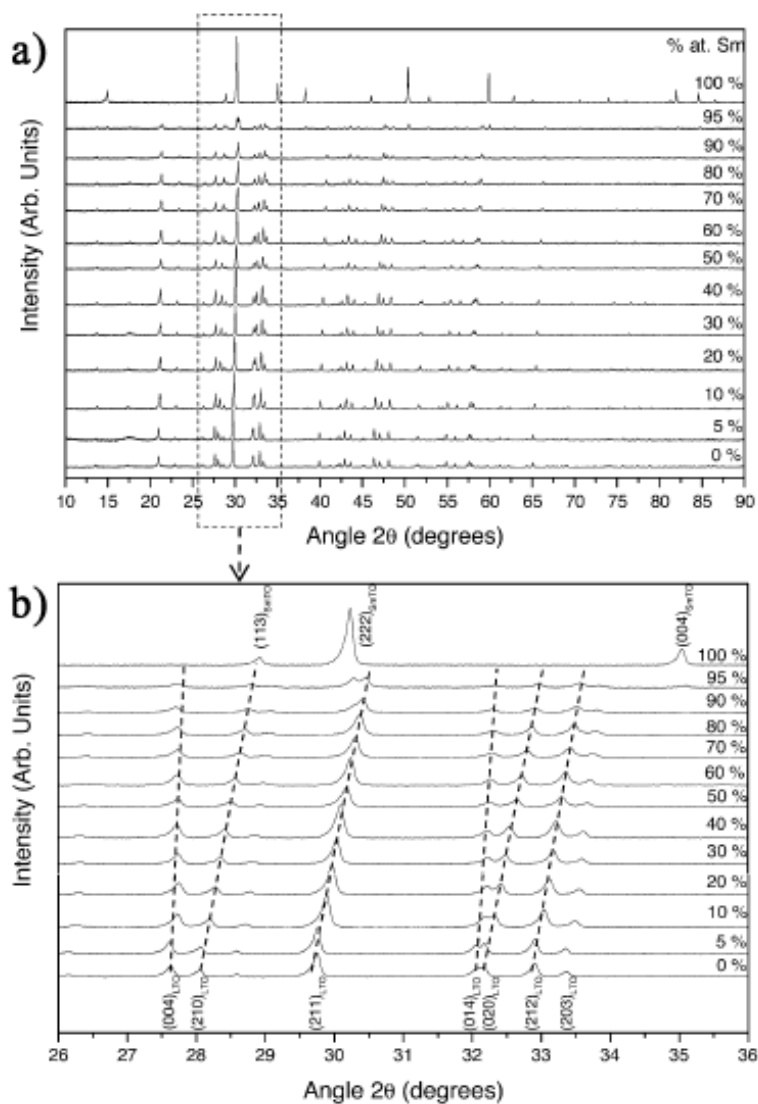

Fig. 2.3.9 XRD patterns of $(La_{1-x}Sm_x)_2Ti_2O_7$ powders.[48]

2.3.2 $A_3B_3O_{11}$ Compounds

The structure of 3-layer $A_3B_3O_{11}$ compounds was first reported by Titov *et al*. at 2001.[15, 16] They prepared polycrystalline $Ln_3Ti_2TaO_{11}$ (Ln = La, Pr, Nd and Sm) samples using the co-precipitation method. $Ln(NO_3)_3$, $TiCl_4$ and TaCl were used as the starting precursors, and an ammonia water solution was used as precipitator. According to their report, single-phase $Ln_3Ti_2TaO_{11}$ with PLS structure were obtained for Ln = La and Pr, but for Ln = Nd and Sm, $Ln_3Ti_2TaO_{11}$ with pyrochlore structure was obtained. Fig. 2.3.10 shows the possible structure models (type I (a) and type II (b)) of $Ln_3Ti_2TaO_{11}$ (Ln = La, Pr). The diffraction pattern of $La_3Ti_2TaO_{11}$ was calculated according to the two models, and the experimental data was consistent with the calculated pattern of mixed-layer model (type II). $La_3Ti_2TaO_{11}$ and $Pr_3Ti_2TaO_{11}$ contain the similar perovskite layers with $La_2Ti_2O_7$, and their crystal structures belong to a non-centrosymmetric space group ($Pmc2_1$), which means that they may present ferroelectricity. The P_s of $La_3Ti_2TaO_{11}$ and $Pr_3Ti_2TaO_{11}$ were estimated to be about 6 and 4 μC/cm^2, respectively, from their second-order nonlinear optical response $I_{2\omega}$.[15]
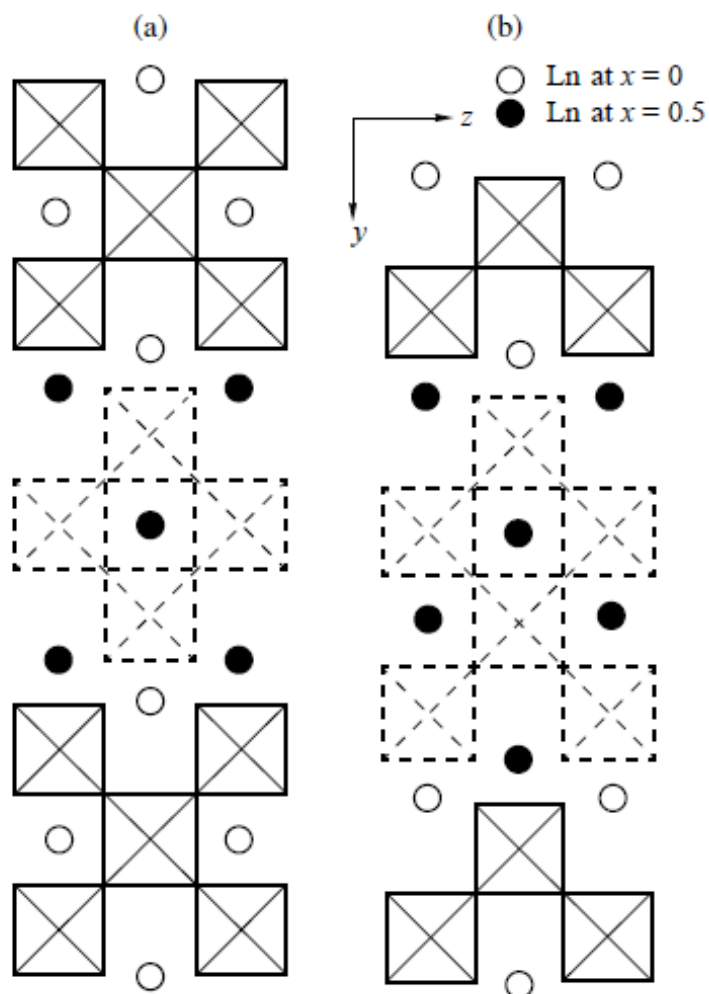
Fig. 2.3.10 Structure models of $Ln_3Ti_2TaO_{11}$ (Ln=La, Pr): (a) identical layers with $n = 3$ (Type I); (b) alternating layers with $n = 2$ and 4 (Type II, the solid and dashed lines delineate BO_6 octahedra at $x = 0.5$ and 0, respectively). [15]

$Sr_2LaTa_3O_{11}$ as the first 3-layer $A_3B_3O_{11}$ compounds with type I structure was also reported by Titov *et al*. in 2002.[17] The crystal structure of $Sr_2LaTa_3O_{11}$ is shown in Fig. 2.3.11. It is formed by two-dimensional perovskite-like blocks and three slabs of distorted TaO_6 octahedra in thickness. The Sr and La atoms are arranged orderly in the PLS layers. The structure of $Sr_2LaTa_3O_{11}$ belongs to the centrosymmetric space group *Immm*. No indications for spontaneous polarization from second harmonic generation

were found in $Sr_2LaTa_3O_{11}$.[9] So $Sr_2LaTa_3O_{11}$ with $A_3B_3O_{11}$ type I structure does not have ferroelectricity.
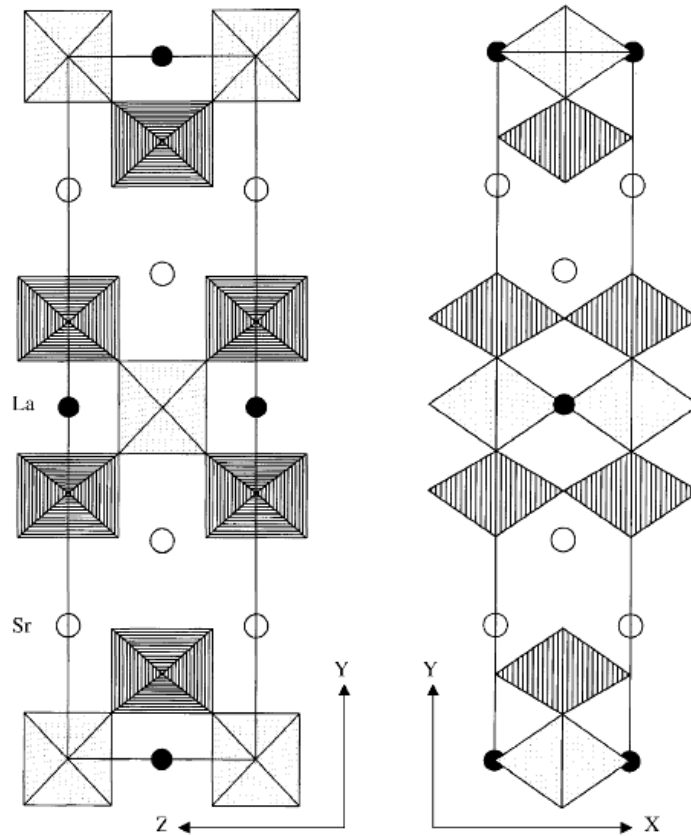
Fig. 2.3.11 Projections of $Sr_2LaTa_3O_{11}$ structure on the YZ and XY planes. [17]

Li *et al*. recently reported the microwave dielectric properties and complex impedance spectroscopy of $La_3Ti_2TaO_{11}$ ceramics.[51, 52] They prepared polycrystalline $La_3Ti_2TaO_{11}$ by conventional solid solute reaction using high-purity La_2O_3, Ta_2O_5, and TiO_2 powders as starting materials. Fig. 2.3.12 shows the XRD pattern of $La_3Ti_2TaO_{11}$ ceramic sintered at 1540 ℃. The crystal structure of $La_3Ti_2TaO_{11}$ ceramics was proved to be orthorhombic with space group *Pmc*2_1 through preliminary structural analysis.
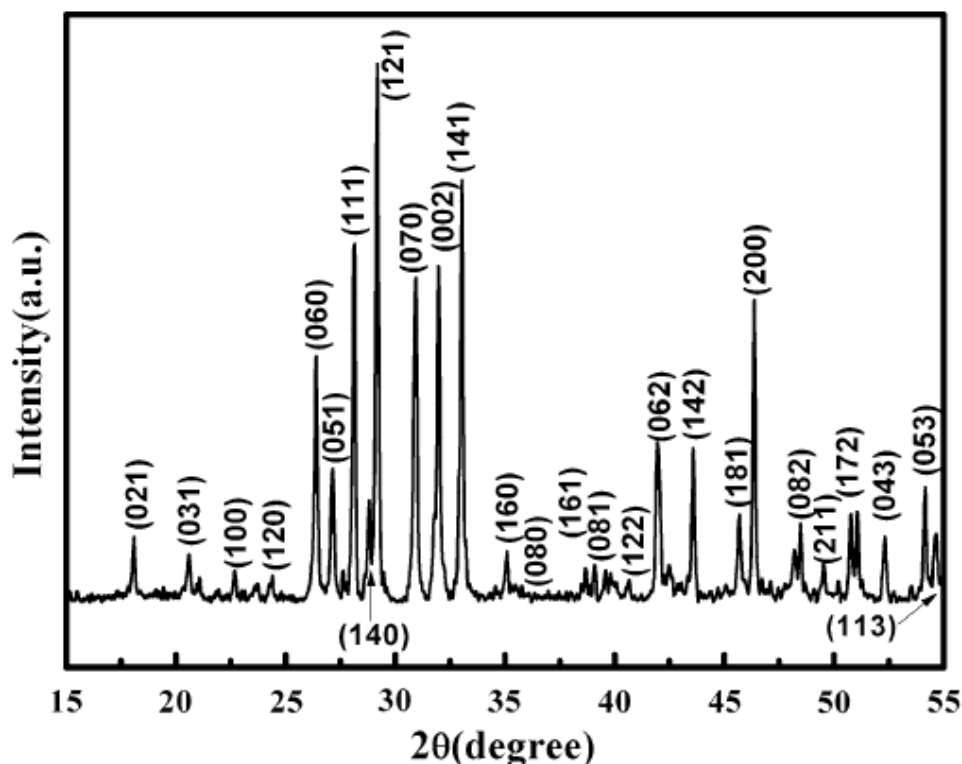
Fig. 2.3.12 Room temperature XRD pattern of $La_3Ti_2TaO_{11}$ ceramic sintered at 1540 °C.[51]

2.3.3 *AB*O$_4$ Compounds

There is no report on the ferroelectricity of 2-layer *AB*O$_4$ compounds ($A_nB_nO_{3n+2}$, $A = Ln$, B = Ta or Nb, $n = 2$). The majority of ABO$_4$ compounds have a centrosymmetric structure at room temperature as shown in Table 2.3.5. However, there is a non-centrosymmetric orthorhombic modification ($A2_1am$) for both LaTaO$_4$ and LaNbO$_4$, which is similar to the structure of multiferroic BaMnF$_4$.[32, 53] The non-centrosymmetric orthorhombic modification of LaNbO$_4$ was prepared at high pressure (8 GPa) and high temperature (1570 K) by Titov *et al*. in 2000.[53] The spontaneous polarization of high-pressure LaNbO$_4$ was evaluated to be 2 μC/cm^2.

The non-centrosymmetric orthorhombic modification of LaTaO$_4$ was reported to be stable above 175 °C by Cava *et al*..[31] Fig. 2.3.13 shows the structure of LaTaO$_4$ at 25

and 300 ℃. It has the $P2_1/c$ monoclinic PLS structure at 25 ℃ and the $A2_1am$ orthorhombic PLS structure at 300 ℃. The monoclinic to orthorhombic phase transition temperature on heating and cooling was reported to be 175/150 ℃. Titov *et al*. also studied the thermal stability limits of polar LaTaO₄.[32] According to their report, the orthorhombic modification is stable in the temperature from at least 20 to 1197 ℃, and coexists with the monoclinic modification below 150 ℃. The spontaneous polarization in orthorhombic LaTaO₄ was estimated to be 1.6 μC/cm^2 according to the second harmonic signal.[32]

In recent years, Vullum *et al*. reported the solid solubility and phase transition in LaNb$_{1-x}$Ta$_x$O₄. According to the differential scanning calorimetry (DSC) results shown in Fig. 2.3.14, the monoclinic to the orthorhombic phase transition of pure LaTaO₄ is observed at 240±5 ℃ on heating. The Nb doped composition LaNb$_{0.2}$Ta$_{0.8}$O₄ shows a decreased phase transition temperature at 100±5 ℃ on heating. Fig. 2.3.15 shows the phase diagram for the binary system LaNO₄-LaTaO₄. A biphase region is observed when 0.4<x<0.8. LaNb$_{1-x}$Ta$_x$O₄ solid solutions have a LaNbO₄-like monoclinic phase when x<0.4 and a LaTaO₄-like monoclinic phase when x>0.8.

Table 2.3.5 Summary of the structure of some ABO$_4$ materials.

Compounds	Symmetry	Structure	Tc/ ℃	Space Group
LaTaO$_4$[31, 32]	Non-centrosym.	Orthorhombic(T>175 ℃)	Unknown	$A2_1am$
	Centrosym.	Monoclinic	N/A	$P2_1/c$
LaNbO$_4$[53, 54]	Non-centrosym.	Orthorhombic (HPM)	Unknown	$A2_1am$
	Centrosym.	Monoclinic[55]	N/A	$I2/c$
	Centrosym.	Tetragonal[55]	N/A	$I4_1/a$
CeTaO$_4$[56]	Centrosym.	Monoclinic	N/A	$P2_1/c$
CeNbO$_4$[56]	Centrosym.	Monoclinic	N/A	$I2/a$
PrTaO$_4$[9]	Centrosym.	Monoclinic	N/A	$P2_1/c$
NdTaO$_4$[9, 57]	Centrosym.	Monoclinic	N/A	$P2_1/c$

*HPM-high pressure modification
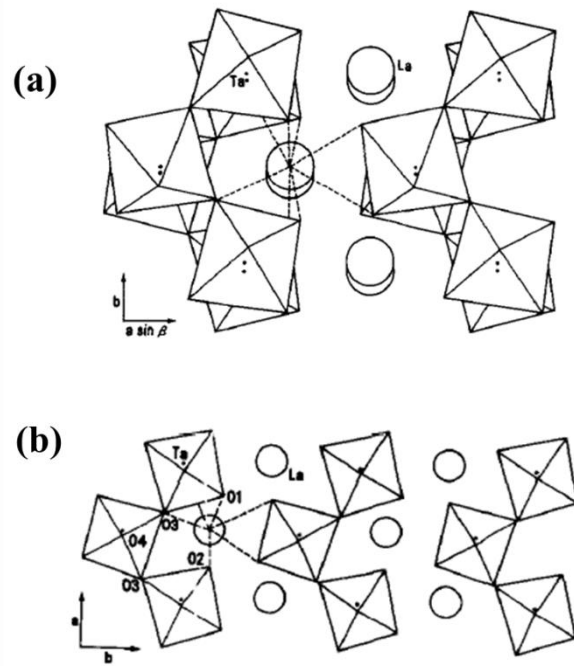
Fig. 2.3.13 (a) the monoclinic structure of LaTaO$_4$ at 25 ℃; (b) the orthorhombic structure of

LaTaO$_4$ at 300 ℃.[31]
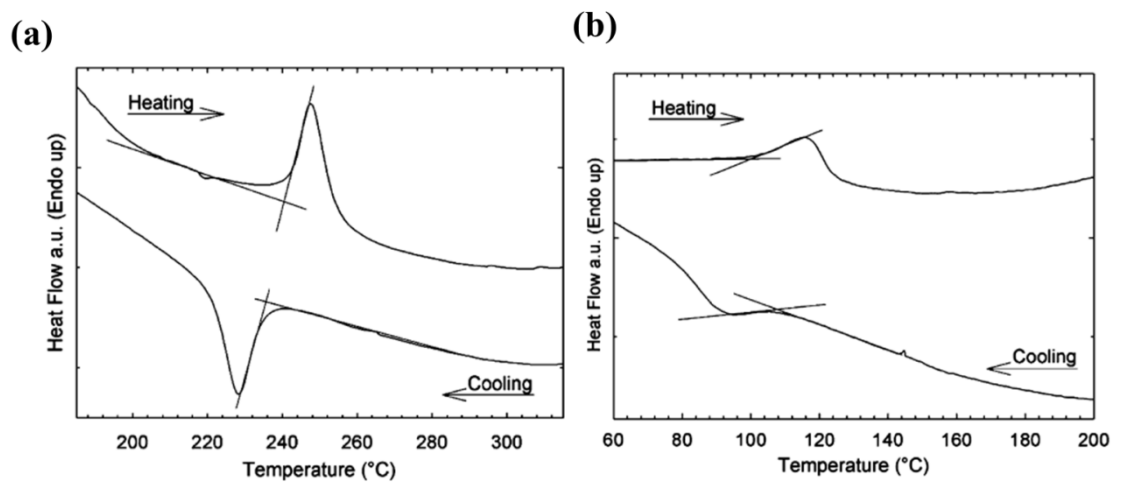
Fig. 2.3.14 DSC measurements: (a) LaTaO$_4$; (b) LaNb$_{0.2}$Ta$_{0.8}$O$_4$.[58]
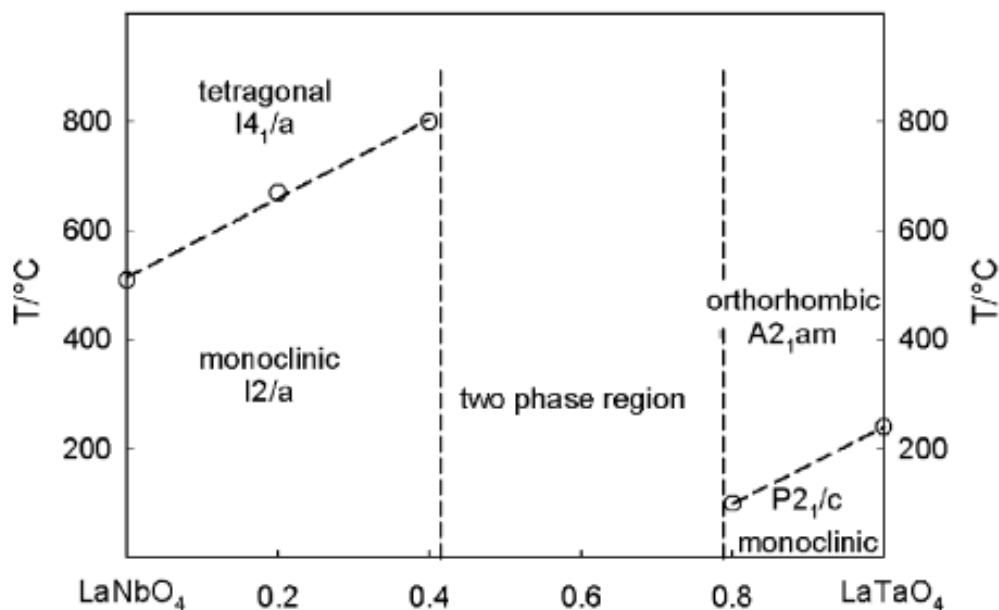
Fig. 2.3.15 Phase diagram for the binary system $LaNbO_4$-$LaTaO_4$.[58]

It is difficult to synthesize phase-pure $LaTaO_4$, because it is very sensitive to annealing temperature and pressure. Consequently, the monoclinic $LaTaO_4$ and the orthorhombic $LaTaO_4$ coexist at room temperature. As the molar volume of monoclinic $LaTaO_4$ is lower than that of orthorhombic $LaTaO_4$, moderate pressure can help the transformation from orthorhombic modification to monoclinic modification at ambient temperature.[58] Single-phase orthorhombic $LaTaO_4$ was also successfully synthesized by some chemical methods like sol-gel method.[25, 59] The photoluminescent and photocatalysis properties of orthorhombic $LaTaO_4$ have been reported, but no ferroelectricity has been demonstrated so far.

2.4 Dion-Jacobson Compounds

There are three structure types of Dion-Jacobson compounds $A'A_{k-1}B_kO_{3k+1}$, depending on the coordination preferences and size of the A' cations.[60] The three structure types mainly differ in the kind of displacement of adjacent layers.[9] If A' is a large cation like Cs^+ (0.188 nm) and Rb^+ (0.172 nm), they have the type I structure shown in Fig. 2.4.1. If A' is a smaller cation like K^+ (0.164 nm), they have the type II structure shown in Fig. 2.4.2, in which the perovskite blocks slip by half a unit cell along the a or b axis only. When A' is an even small cation like Li^+ (0.092) or Na^+ (0.139), they have the type III structure, in which the perovskite blocks in adjacent layers along c slip by half a unit cell along ab. Table 2.4.1 lists the structure of some Dion-Jacobson compounds. Most of them have a centrosymmetric structure. $RbBiNb_2O_7$ and $CsBiNb_2O_7$ have the non-centrosymmetric orthorhombic structure $P2_1am$, which was first reported by Subramanian et $al.$ in 1988.[61]

In 2003, Snedden et $al.$ used powder neutron diffraction to study the distortions in layered perovskite $CsBiNB_2O_7$ and proved that the room temperature phase has a polar orthorhombic structure $P2_1am$.[62] They found that the structure distortions in $CsBiNb_2O_7$ are produced by the off-centre displacements of Bi^{3+} cations and cooperative tilts of NbO_6 octahedrons, which is similar to the behaviour of Aurivillius ferroelectrics such as $SrBi_2Ta_2O_9$. But they concluded that $CsBiNB_2O_7$ does not display ferroelectricity according to its rather low and temperature-independent dielectric constant behaviour.

The ferroelectricity of $CsBiNb_2O_7$ was first studied from first principles by Fennie et $al.$ in 2006.[63] They proved that the ground state of $CsBiNb_2O_7$ is $P2_1am$ through phonon calculations. Spontaneous polarization of $CsBiNb_2O_7$ is 40 $\mu C/cm^2$ calculated by Berry-phase method, which is three times larger than that of the Aurivillius ferroelectrics $SrBi_2Ta_2O_9$.

$= BO_6$ octahedra (O located at the corners, B hidden in the center)

● A'

● A

b (or a) ←

c ‖ [100] $_{\text{perovskite}}$

$k = 2$	$k = 3$	$k = 4$	$k = \infty$
$A'AB_2O_7$	$A'A_2B_3O_{10}$	$A'A_3B_4O_{13}$	ABO_3 perovskite
$RbLaNb_2O_7$	$RbCa_2Nb_3O_{10}$	$RbCa_2NaNb_4O_{13}$	$CaNbO_3$

Fig. 2.4.1 Schematic representation of the idealized Dion-Jacobson type I crystal structures when $k = 2, 3, 4$, and ∞.[9] Perpendicular to the drawing plane, there is a height difference between the BO_6 octahedra and the A cations of about 2 Å, the half of the octahedron body diagonal.
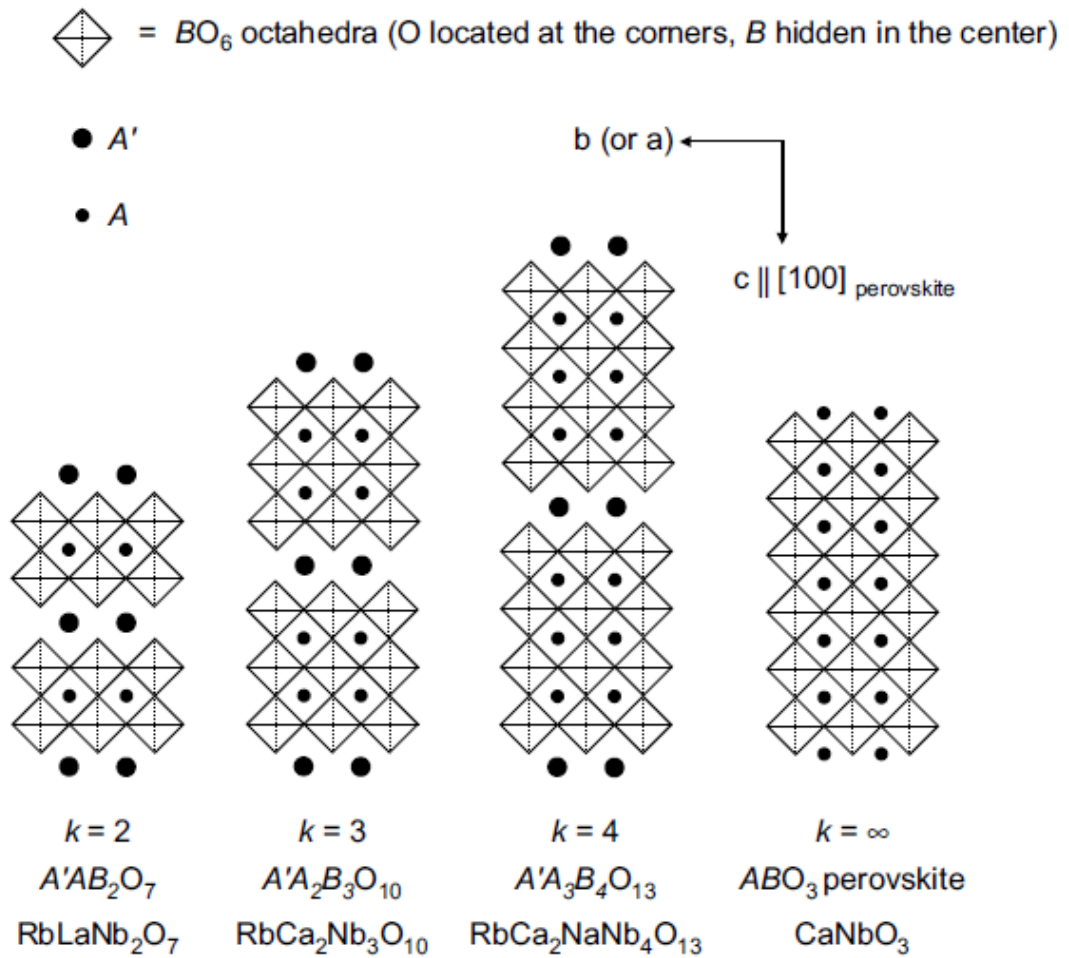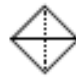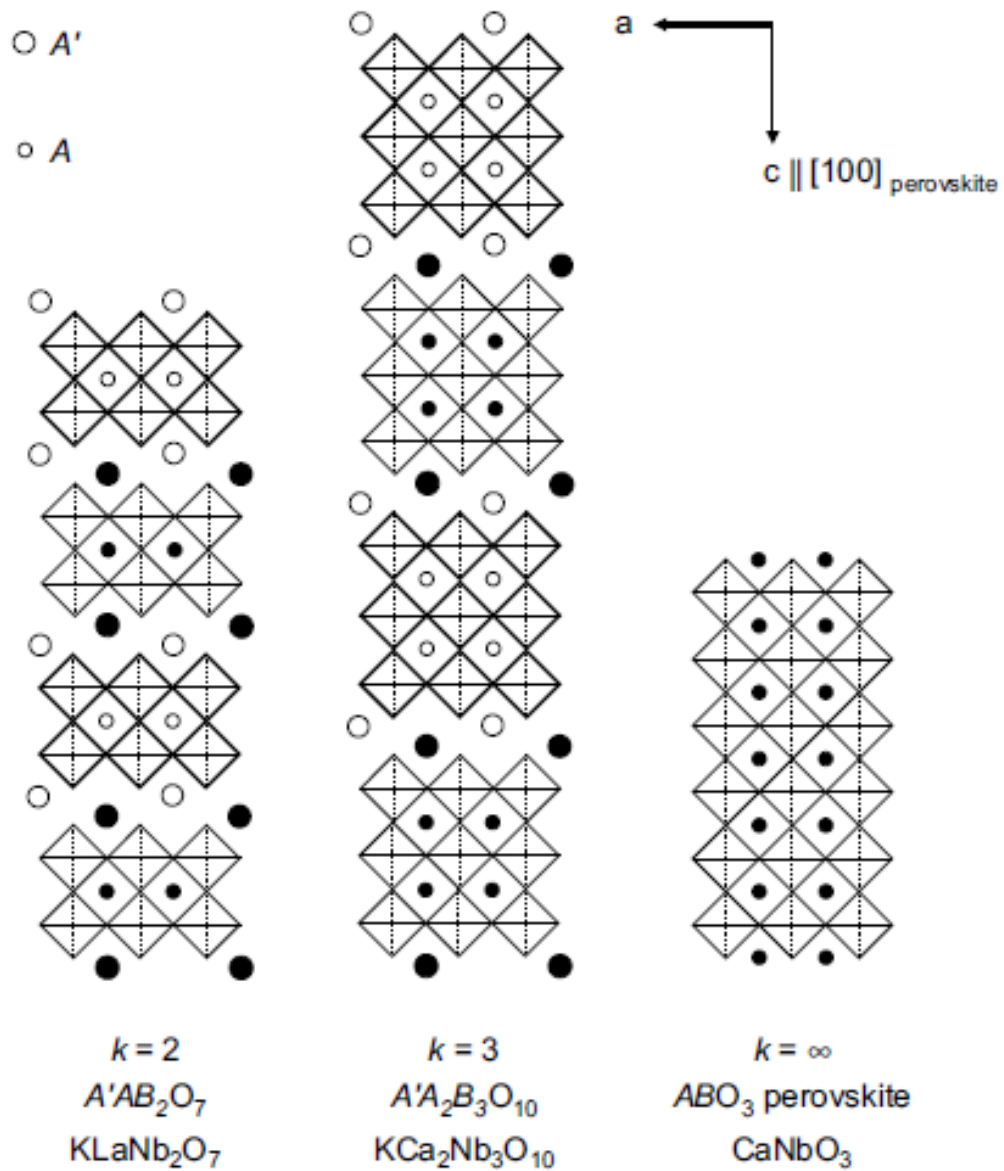
Fig. 2.4.2 Schematic representation of the idealized Dion-Jacobson type II crystal structures when k = 2, 3, and ∞.[9] Light and heavy drawing of the BO_6 octahedra and filled and open circles indicates a height difference perpendicular to the drawing planes of about 2 Å.

Table 2.4.1 Symmetry of some compounds with Dion-Jacobson structures.[9]

Compounds	k	Space group	Symmetry
$NaLaNb_2O_7$	2	*I4/mmm*	Centrosym.
$BaSrTa_2O_7$	2	*Immm*	Centrosym.
$RbBiNb_2O_7$[61, 64, 65]	2	*P2₁am*	Non-centrosym.
$CsBiNb_2O_7$[61, 62]	2	*P2₁am*	Non-centrosym.
$CsCa_2Nb_3O_{10}$	3	*Pnma*	Centrosym.
$KCa_2Nb_3O_{10}$	3	*Cmcm*	Centrosym.
$KSr_2Nb_3O_{10}$	3	*P2₁2₁2₁*	Non-centrosym.
$NaCa_2Ta_3O_{10}$	3	*I4/mmm*	Centrosym.
$BaLa_2Ti_3O_{10}$	3	*P2₁/m*	Centrosym.
$RbCa_2NaNb_4O_{13}$	4	*P4/mmm*	Centrosym.

Goff *et al*. attempted to experimentally demonstrate ferroelectricity in $CsBiNb_2O_7$.[66] They studied the structural change of $CsBiNb_2O_7$ with increasing temperature from room temperature up to 900 ℃ by powder neutron diffraction. Fig. 2.4.3 shows the thermal evolution of the lattice parameters from 25 to 900 ℃. The degree of orthorhombic distortion was represented by $2(a\text{-}b)/(a\text{+}b)$. The orthorhombic distortion decreases with increasing temperature, and the unit cell changes toward a tetragonal paraelectric phase. However, there was no direct evidence for a phase transition below 900 ℃ (Fig. 2.4.3), which means that the ferroelectric-paraelectric phase transition is above 900 ℃. They performed the *P-E* measurements to observe the ferroelectric polarization, but no *P-E* hysteresis was obtained due to the leakage currents.
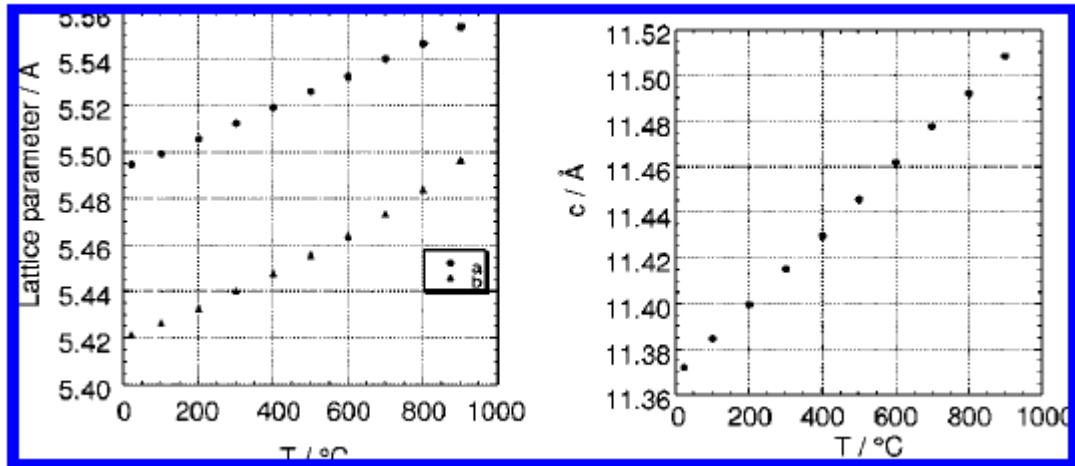
Fig. 2.4.3 Thermal variation of the lattice parameters: (a) *a* and *b*, and (b) *c*.[66]

Recently, Li *et al*. reported the first characterization of the ferroelectricity and piezoelectricity of Dion-Jacobson compound RbBiNb$_2$O$_7$.[64] Fig. 2.4.4(a) shows the temperature dependence of its dielectric constant. The frequency-independent peaks at about 945 ℃ indicate the ferroelectric-paraelectric phase transition point (T_c). They also performed the *P-E* measurements (Fig. 2.4.4(a)), but the unsaturated *P-E* hysteresis loop does not provide evidence of ferroelectric polarization switching. The ferroelectric-paraelectric phase transition was also proved by the Raman spectra shown in Fig. 2.4.4(b), indicated by the disappearance of the low frequency phonon modes above 945 ℃. The piezoelectric constant d_{33} of RbBiNb$_2$O$_7$ ceramic was measured to be 12 pC/N. The thermal depoling result is shown in Fig. 2.4.4(c). The d_{33} is stable below 800 ℃ and disappeared above T_c.
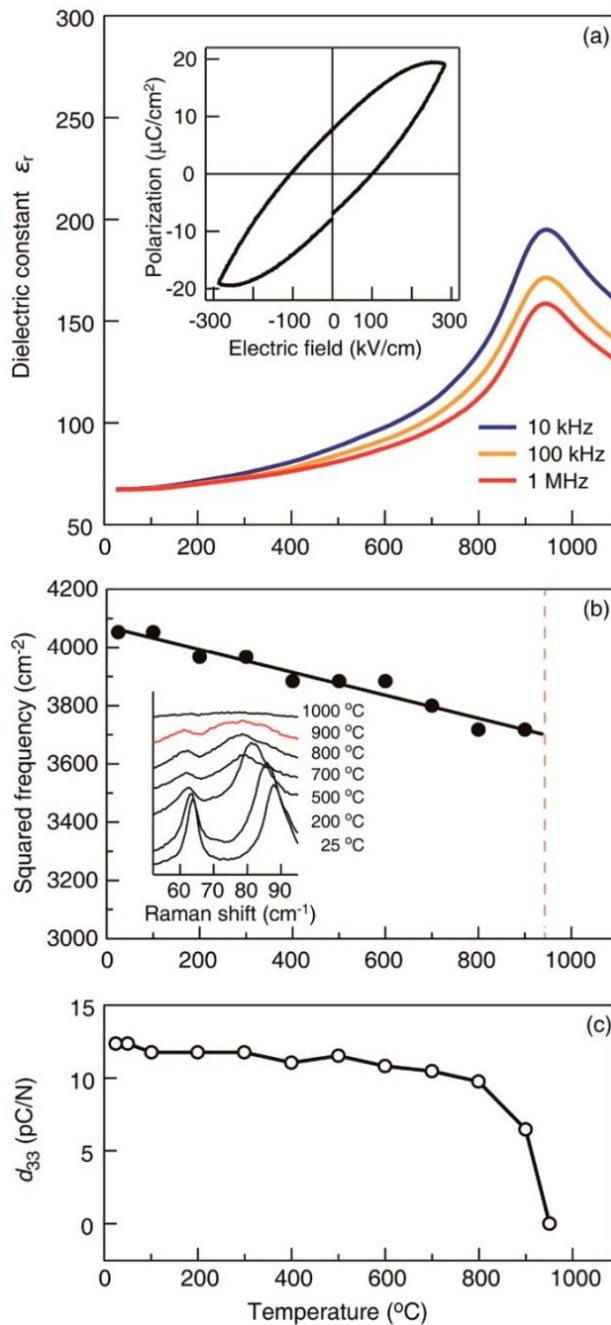
Fig. 2.4.4 (a) Temperature dependence of the dielectric constant. The inset shows room-temperature *P-E* hysteresis loop. (b) Variation of the lowest-frequency mode as a function of temperature. The inset shows low-frequency Raman spectra above and below T_c. (c) Temperature dependence of the piezoelectric constant d_{33}.[64]

2.5 Hexagonal Compounds

As discussed in chapter 2.2, the Hexagonal phases $A_mB_{m-1}O_{3m}$ can be regarded as a result of cutting the perovskite structure across the (1 1 1)$_{perovskite}$ planes, which means that they have more complicated structures than the Dion-Jacobson and $A_nB_nO_{3n+2}$ phases. Fig. 2.5.1 shows an illustration of the idealized Hexagonal phase when $m = 4$, 5, 6, 7, and ∞. Most of the compounds with Hexagonal phase have a centrosymmetric structure as shown in Table 2.5.1. So far, only two Hexagonal compounds, $Sr_6Nb_4TiO_{18}$ and $La_6Ti_{4.04}Mg_{0.913}O_{18}$, have been reported to be non-centrosymmetric and have the potential to present ferroelectricity.[9]

Table 2.5.1 Symmetry of some compounds with Hexagonal phase $A_mB_{m-1}O_{3m}$.[9]

Compounds	m	Space group	Symmetry
$Ba_3Re_2O_9$	3	$R\bar{3}m$	Centrosym.
$LaSr_3Ta_3O_{12}$	4	$R\bar{3}m$	Centrosym.
$Sr_5Nb_4O_{15}$	5	$P\bar{3}c1$	Centrosym.
$Sr_6Nb_4TiO_{18}$	6	$R3m$	Non-centrosym.
$La_6Ti_{4.04}Mg_{0.913}O_{18}$	6	$R3m$	Non-centrosym.
$Ba_2La_4Ti_5O_{18}$	6	$R\bar{3}$	Centrosym.
$Sr_7Nb_6O_{21}$	7	$R\bar{3}$	Centrosym.
$Ba_{11}Nb_8TiO_{33}$	5+6	$R\bar{3}m$	Centrosym.
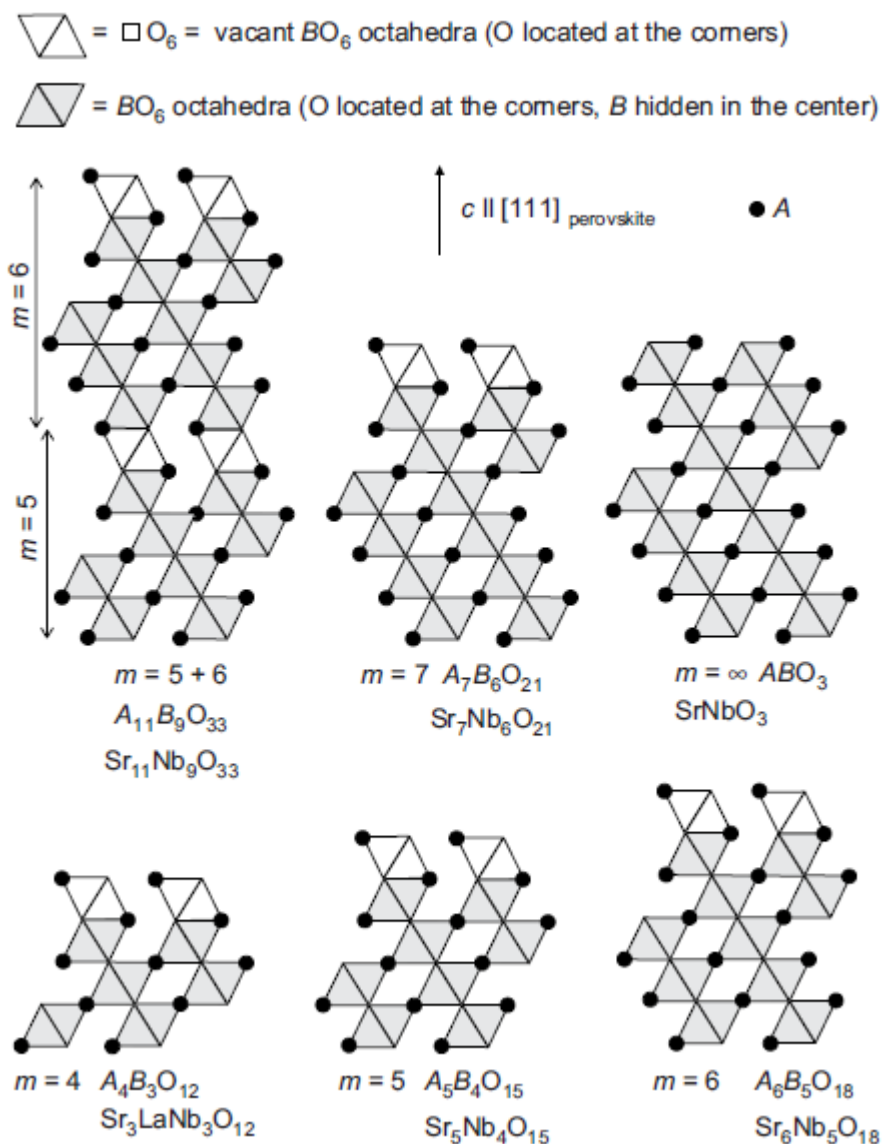
Fig. 2.5.1 Schematic representation of the idealized Hexagonal phase $A_mB_{m-1}O_{3m}$ when $m = 4, 5,$

6, 7, and ∞.

The structure of 6-layer Hexagonal compounds $Sr_6Nb_4TiO_{18}$ was first reported by Drew

et al. in 1997.[67] Polycrystalline $Sr_6Nb_4TiO_{18}$ was prepared by solid state reaction using

starting oxides as SrO_2, TiO_2, and Nb_2O_5. Its crystal structure was indicated to be non-

centrosymmetric space group *R3m* by X-ray powder diffraction analysis. Fig. 2.5.2

shows the crystal structure of $Sr_6Nb_4TiO_{18}$ projected along the [110] direction. This

structure contains perovskite-like layers with five octahedral in thickness. $La_6MgTi_4O_{18}$

was studied by Vanderah *et al*. Non-stoichiometric composition $La_6Mg_{0.913}Ti_{4.04}O_{18}$ was

formed and indexed to be isostructural with $Sr_6Nb_4TiO_{18}$.[68]
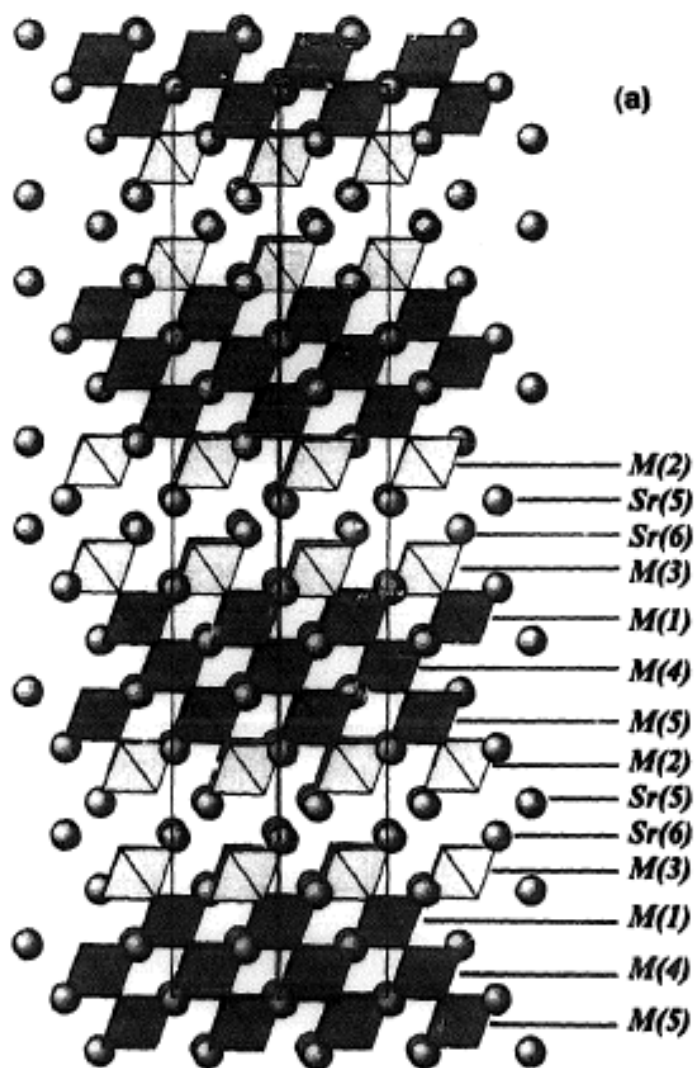
Fig. 2.5.2 The crystal structure of $Sr_6Nb_4TiO_{18}$ projected along the [110] direction.[67]

2.6 Synthesis Methods

2.6.1 Powders Synthesis

(a) Solid State Reaction

The solid state reaction method is the most conventional technique to prepare polycrystalline powders. A mixture of solid state materials, such as simple oxides, carbonates, nitrates, sulfates, oxalates, or acetates, are usually used as starting materials. Normally, as the starting solids are very stable and do not react together at room temperature, a heat treatment process, usually called calcination, is very necessary. Fig. 2.6.1 shows the process of a simple solid state reaction between two solids, A and B. At the beginning, a homogeneous mixture of starting materials A and B are obtained by ball-milling method. A and B will start to react and form a new compound C during the heating treatment. At this step, the reaction mechanisms involve complicated solid diffusions, like the transport of atoms, ions, or molecules. Pure-phase C will be obtained when A and B have fully reacted. Lots of parameters including the size and shape of the particles, the uniformity of the mixed powders, the reaction atmosphere, the time and temperature should be considered during the solid state reaction process.

The remarkable advantage of the solid state reaction method is its low cost, which makes it the most suitable method for industrial productions. There are also several drawbacks of solid state reaction method that should be noticed: a grinding step is always necessary to break the agglomerated powders, which normally leads to the contamination of the powder with impurities; it is difficult to control the particle size and shape of the productions; the mixed powders with poor uniformity may result in the incompletion of the reactions with undesirable phases.[69]
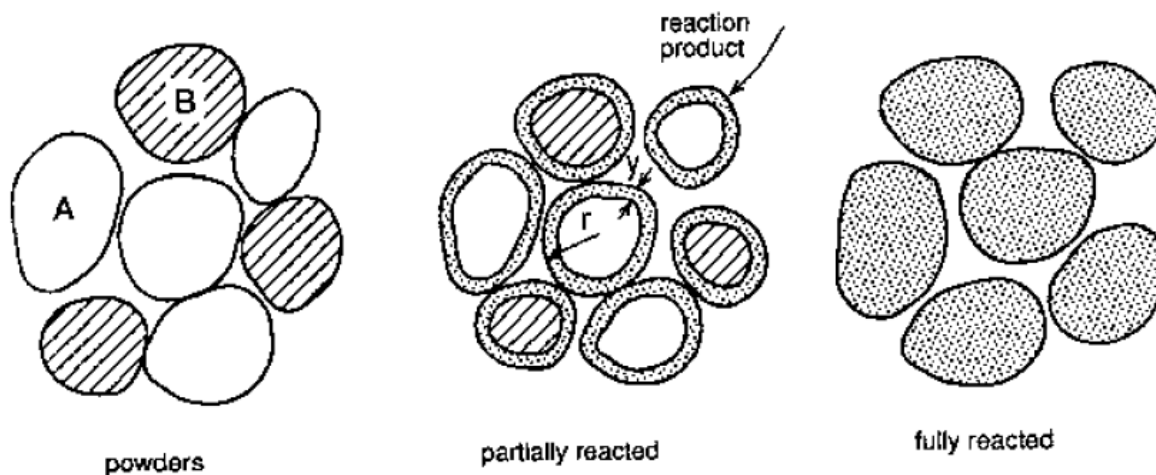
Fig. 2.6.1 Schematic of solid-state reaction in mixed powders.[69]

(b) Co-precipitation Method

For some complex oxides, which contain more than one metal element in its chemical formula, it is difficult to obtain single phase with solid-state reaction between mixed oxide powders. The co-precipitation method is an ideal way to prepare fine composite powders that contain at least two metal oxides. In the co-precipitation route, mixed metal salts or combination of salts and alkoxides are used to prepare the precursor solution, and a precipitator, like ammonia water and aqueous sodium hydroxide, is generally used to react with the precursor solution to generate an mixture of precipitates [7, 70, 71]. The desired composition can be synthesized by calcining the mixture at high temperature. Compared with solid-state reaction method, the raw materials for co-precipitation method are more expensive, and it is difficult to control the hydrolysis of the precursor solution, since the hydrolysis rates of different reactants are different, which results in segregation of the precipitated mixture. [69]

(c) Sol-Gel Method

During the past 40 years, the sol gel method was developed as an alternative for the synthesis of ceramic powders at considerably lower temperatures.[72] In general, the sol-gel process is to convert the sol (a solution of metal compounds or a suspension of very fine particles in a liquid) into a gel (highly viscous mass), which can be dried and ground to produce powders.[69] A typical sol-gel process usually consists of 5 steps: (1) formation of sol; (2) gelation; (3) aging; (4) drying; (5) firing. The initial precursors used for sol-gel process can be divided to three groups: (I) aqueous solutions of metal salts; (II) metal alkoxide solutions; (III) mixed organic and inorganic precursors.[72] The selection of the initial precursors and the conditions of the reactions are very important because they critically decide the composition of particles and the homogeneity of component distribution.[73] The disadvantages of sol-gel method are the high cost of the raw materials and the time-consuming process.[69, 74] Table 2.6.1 shows the advantages and disadvantages of some common powder synthesis methods for ceramics.

Table 2.6.1 Common Powder Preparation Methods for Ceramics [69]

Powder preparation method	Advantages	Disadvantages
Solid state reaction	Simple apparatus, inexpensive	Agglomerated powder, limited homogeneity for multicomponent powders
Liquid solutions: Co-precipitation; Sol-gel method; Hydrothermal method.	High purity, small particle size, composition control, chemical homogeneity	Expensive, poor for nonxides, powder agglomeration commonly a problem
Gas-solid reaction	Commonly inexpensive for large particle size	Commonly low purity, expensive for fine powders
Gas-liquid reaction	High purity, small particle size	Expensive, limited applicability
Reaction between gases	High purity, small particle size, inexpensive for oxides	Expensive for nonoxides, agglomeration commonly a problem

2.6.2 Spark Plasma Sintering

Compared with the conventional sintering technique, Spark plasma sintering (SPS) is characterized by low voltage, direct current pulsed current activated, pressure-assisted sintering.[75] In the recent years, SPS, which is also known as pulsed electric-current sintering (PECS), field-assisted sintering technique (FAST) or current-activated pressure-assisted densification (CAPAD), has been widely used for materials processing.[76, 77] Although SPS has been used for a long time, no direct evidence of spark

or plasma was observed.[78, 79] Therefore, lots of people prefer to use the name 'field-assisted sintering technique' instead of 'spark plasma sintering' nowadays.[75]

Fig. 2.6.2 shows the basic working schematic of the SPS apparatus. As a uniaxial pressure is applied to the powders during the sintering process, SPS is similar to hot pressing (HP), but the sintering mechanisms of SPS and HP are different. For SPS, with the assist of high electric current, materials can be sintered to full density much faster than by HP. For instance, a typical SPS process usually takes 30 to 60 minutes, but many hours even days are necessary for conventional sintering methods. In addition, the temperature for obtaining the materials with full density is always significantly lower by using SPS.[77, 78, 80]

As discussed in chapter 2.3.1, one efficient method to reduce the coercive field of ferroelectric ceramics with random orientated grains is to texture them. In this work, almost all the materials have plate-like grains due to their perovskite-like layered structures, therefore texture is very necessary to applied to demonstrate their ferroelectricity. Using SPS, a two-steps sintering method is used in our work. The schematic of two-steps SPS texture process is shown in Fig. 2.6.3. In the first step, powders are sintered into a dense ceramic with minimal grain growth. In the second step, the ceramic is put into a larger die and sintered at higher temperature with high pressure. During this step, the pressure constrains the grain growth direction. At last, dense ceramics with highly orientated grains are obtained.
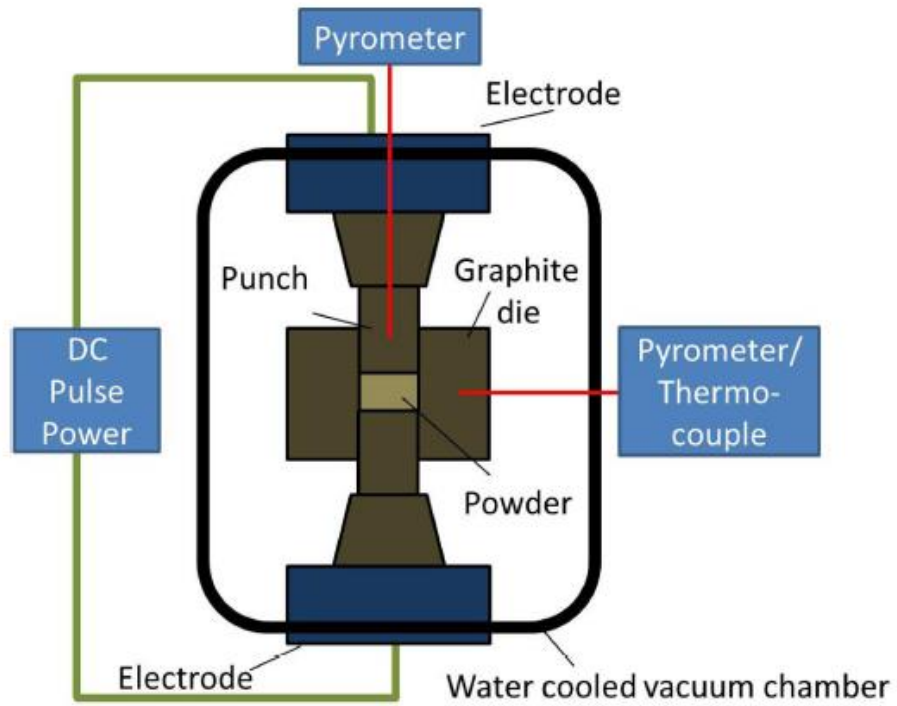
Fig. 2.6.2 Working schematic of the SPS apparatus.[75]
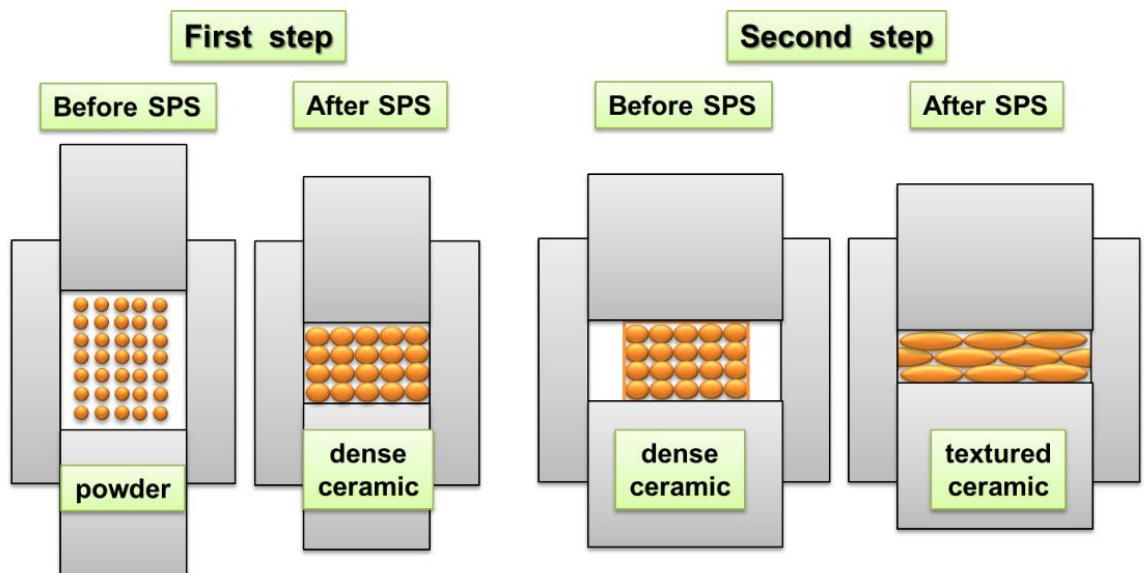
Fig. 2.6.3 The schematic of two-steps SPS texture process.

Chapter III. Experimental Procedure

Fig. 3.1 shows the flowchart of the basic experimental procedure for the preparation and characterizations of the ceramics in this work. The whole procedure can be divided into three parts: powder preparation, ceramic sintering, and characterization. In the first step powder preparation, we used the traditional ball-milling method, and chemical methods like co-precipitation and sol-gel to obtain powders with different grain size. For ceramic sintering, we mainly used the SPS, and conventional sintering was also applied to some compounds. A number of characterization methods were applied to analyse the crystal structures, microstructures, and dielectric, ferroelectric and piezoelectric properties of the materials. The details of those characterization methods will be given in later sections.
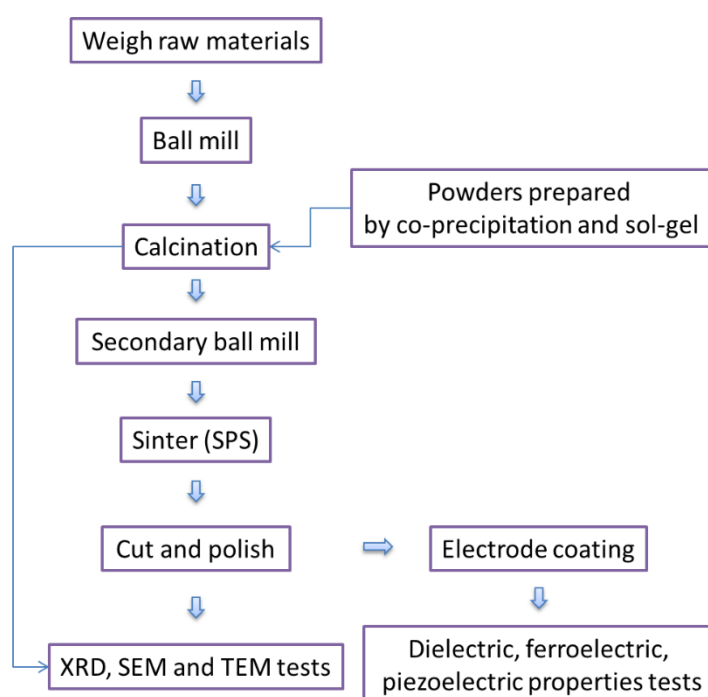
Fig. 3.1 The flowchart of the basic experimental procedure.

3.1 Powder Preparation

3.1.1 Ball-Milling Method

For solid state reaction, the oxides and carbonates given in Table 3.1.1 were used as the starting materials. The starting powders were weighed according to the stoichiometric formula of the desired composition. Wet ball-milling method was employed to mix the starting powders and reduce the particle size. The starting powders were put into a nylon ball-milling pot with ZrO_2 milling balls with 5 mm and 10 mm diameter. Ethanol was used as the liquid milling media. The ratio of the volume of powders, ethanol, and milling balls was about 1:2:3. A planetary ball milling machine was employed (Fig. 3.1.1). The starting powders were mixed with ball-milling speed of 450 rpm for 3 hours. After ball milling, the mixture was dried at 80 ℃. Then the dried mixture was sieved using a stainless steel sieve (aperture diameter 250 μm) to control the particle size.

Fig. 3.1.1 Planetary ball milling machine (QM-3SP4, Nanjing University Instrument Plant, China). Inset shows the nylon ball-milling pot with ZrO_2 milling balls.

Table 3.1.1 Purity of raw materials

Materials	Purity	Manufacturer
La_2O_3	99.99%	Alfa Aesar
Pr_6O_{11}	99.9%	Sigma-Aldrich
Sm_2O_3	99.9%	Alfa Aesar
Eu_2O_3	99.9%	Alfa Aesar
TiO_4	99.8%	Alfa Aesar
Ta_2O_5	99.85%	Alfa Aesar
Nb_2O_5	99.9%	Alfa Aesar
$La(NO_3)_3\ 6H_2O$	99.9%	Alfa Aesar
$Pr(NO_3)_3\ 6H_2O$	99.9%	Sigma-Aldrich
$Ti(OCH_9)_4$	97%	Sigma-Aldrich
$TaCl_5$	99.8%	Sigma-Aldrich
Rb_2CO_3	99.8%	Alfa Aesar
Cs_2CO_3	99.9%	Alfa Aesar
Bi_2O_3	99.9%	Alfa Aesar
$SrCO_3$	99.9%	Sigma-Aldrich

Solid state reaction was used for powder calcination. The mixed raw powders were put in alumina crucibles and calcined in a conventional chamber furnace (Fig. 3.1.2(a)). The ideal calcination temperature was chosen to be high enough to obtain single-phase materials, low enough to permit easy subsequent re-milling. Then the calcined powders were re-milled at 350 rpm for 4 hours to reduce their particle size.
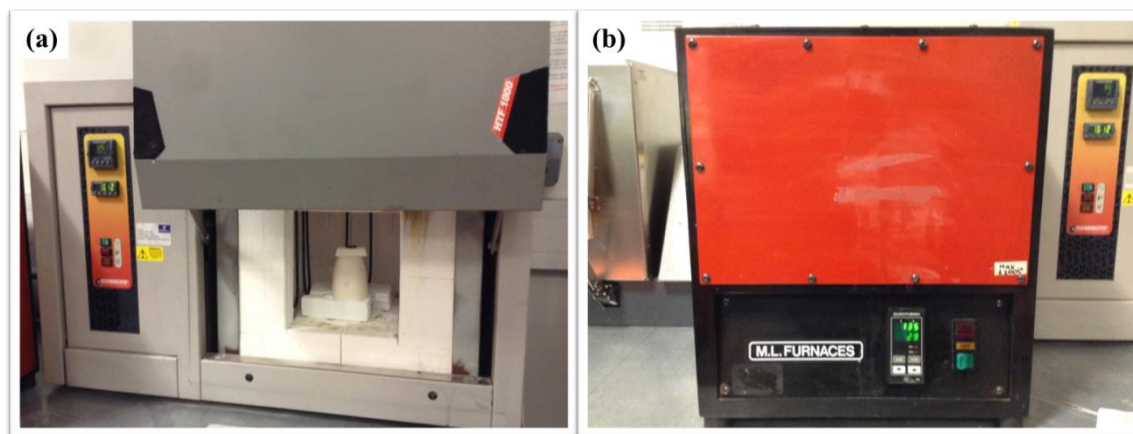
Fig. 3.1.2 (a) Conventional chamber furnace (Carbolite HTF 1800, UK), (b) Tube furnace (M.L.Furnaces, UK).

3.1.2 Co-precipitation Method

For some complex oxides, it was difficult to obtain single phase by solid state reaction between oxides, and so for these co-precipitation method was applied. Metal salts and alkoxides like $TaCl_5$, $Pr(NO_3)_3\ 6H_2O$, and $Ti(OCH_9)_4$ were chosen as the starting precursors. Stoichiometric amounts of the precursors of the desired composition were dissolved in ethanol at room temperature for 12 hours to obtain a precursor solution. Ammonia solution (10 cm^3 concentrated ammonia in 100 cm^3 ethanol) was added into the precursor solution dropwise, resulting in precipitation. During this process the pH was maintained above nine by the addition of a few drops of aqueous concentrated ammonia. The precipitate was centrifuged to separate from the liquid, then rinsed three times with deionized water and finally once with ethanol, before drying at 80 °C.[7, 15, 70, 81] After that the dried precipitate was calcined at high temperature.

3.2 Sintering by SPS

The calcined powders were sintered in graphite dies using a SPS furnace (Fig. 3.2.1). Graphite dies and punches were used for SPS sintering due to its good electrical conductivity and mechanical strength at high temperature. Graphite foils were used to enclose the powders to stop contact between the dies and powders and maintain good thermal and electrical contact between dies and punches.

Fig. 3.2.1 Spark Plasma Sintering furnace (HPD 25/1 FCT, Germany).

One-step SPS sintering was used to prepare dense untextured ceramics and a two-step SPS sintering method was used to produce textured ceramics. For the one-step method and the first step of the two-step method, graphite dies with 20 mm diameter were usually used. After this step, dense ceramics with average density above 95% were

obtained. For textured ceramics, in the second step the densified ceramics obtained in the first step were placed in larger dies (30 mm diameter) and sintered at higher temperature to produce hot forging. To remove any carbon contamination and oxygen defects caused during the SPS process in a reducing atmosphere, all of the sintered ceramics were annealed at 100 ℃ below their sintering temperature for 10 to 15 hours in air in a chamber furnace or tube furnace (Fig. 3.1.2).

3.3 Characterizations

3.3.1 Density Measurement

The densities of all of the samples were measured using the Archimedes principle. The density ρ was calculated with the following equation:[82]

$$\rho = \frac{m_1 \rho_0}{m_2 - m_3}$$

Where m_1 is the mass of the dry sample in air; m_2 is the mass of the sample after soaking in water; m_3 is the mass weighed while the sample is immersed in water; ρ_0 is the density of water. Normally $m_1 = m_2$ for samples with nearly fully dense or only closed pores.

3.3.2 Crystallographic Structure and Microstructure Characterizations

First the crystallographic structure of the powders and ceramics were analysed by X-ray diffraction (XRD). XRD as a non-destructive technique is widely used to analyse the phase identification, quantitative analysis, and crystal structure of materials. XRD analysis is based on Bragg's law: $n\lambda = 2d\sin\theta$, where n is an integer; λ is the wavelength of the X-ray beam; d is the spacing between the parallel planes in the crystal structure; θ is the angle between the X-ray beam and the scattering planes.[83]

In this work, for phase identification, data were collected on a Siemens D5000 X-ray diffractometer using LiF monochromated Cu-Kα radiation ($\lambda = 1.5418$ Å) over the 2θ range 8° to 70° in steps of 0.03° with a count rate of 10 s per step. For Rietveld analysis, data were collected on a PANalytical X'Pert Pro diffractometer, fitted with an X'Celerator detector, in θ/θ geometry using Ni filtered Cu-Kα radiation ($\lambda = 1.5418$ Å) over the 2θ range 5° to 120° in steps of 0.0167° with an effective count rate of 200 s per step. Both were calibrated with an external LaB$_6$ standard. A preliminary structural

analysis was carried out by the Rietveld method using the GSAS suite of programmes.[84, 85]

The degree of preferred grain orientation of the textured ceramics was estimated using the Lotgering orientation factor *f*, calculated using following equations:

$$f = \frac{P - P_0}{1 - P_0}, P = \frac{\sum I(0\,k\,0)}{\sum I\,(h\,k\,l)}, \text{ and } P_0 = \frac{\sum I_0(0\,k\,0)}{\sum I_0(h\,k\,l)}.$$

where *P* and P_0 are the integrated intensities of all (0 *k* 0) planes to the integrated intensities of all (*h* *k* *l*) planes for preferentially and randomly oriented samples, respectively.[7, 86]

The microstructures of the samples were observed using scanning electron microscopy (SEM, FEI, Inspect F, Hillsboro, OR) and transmission electron microscopy (TEM, JEOL 2010). Bulk samples for SEM observation were polished using silicon carbide paper (up to grade 4000) and then thermally etched at 70 to 100 ℃ below their sintering temperatures for 15 to 30 min to reveal the surface grain structure. All of the powders and ceramics samples were coated with gold or carbon to make them conductive. Bulk samples for TEM observation were ground and polished down to a thickness of 30-50 μm. Then the samples were ion-beam thinned using a Precision Ion Polishing System (PIPS). DigitalMicrograph software was used to analyse the TEM images and diffraction patterns.

Piezoresponse force microscopy (PFM) was used to observe the ferroelectric domain structure. PFM experiments were performed by Dr. Serban Lapadatu using a Veeco Dimension 3000 atomic force microscope (AFM) at National Physical Laboratory (NPL).

3.3.3 Spectroscopy

Raman spectroscopy (Nicolet Almega XR dispersive Raman Spectrometer) was used to observe vibrational, rotational, and other low-frequency modes in compounds with PLS structure. X-ray photoelectron spectroscopy (XPS) was used to determine the chemical state of different elements in the samples. The XPS data was collected using an ESCALAB 250 XPS meter at Aston University Birmingham.

3.3.4 Electrical Measurements

Samples for electrical measurements were coated with platinum paste (Gwent Electronic Materials Ltd, C2011004D5) as electrodes and fired at 1100 ℃ for 30 min.

The frequency dependence of dielectric constants and losses of ceramics were obtained using an Agilent 4294A Precision Impedance Analyser at room temperature. The measured capacitances C were converted into the relative dielectric constants ε_r using the equation: $\varepsilon = \frac{Cd}{\varepsilon_0 A}$, where d and A are the thickness and the electrode area of the samples, respectively; ε_0 is the vacuum dielectric constant ($\varepsilon_0 \approx 8.854 \times 10^{-12}$ F/m).

The temperature dependence of dielectric constants and losses of ceramics were obtained using an Agilent 4284A Precision Impedance Analyser. The meter was connected to a high temperature tube furnace (Leton, LTF 16/--/180, T_{max}= 1600 C). Curie points of materials were determined by the change of dielectric constants with the change of temperature. The accuracy of the temperature was evaluated by using reference sample with known Curie point like LiNbO$_3$ (T_c = 1140 ℃). The impedance spectroscopy of ceramics was measured using the same set-up.

The temperature dependence of DC resistivity ρ was measured using a high resistance meter (KEITHLEY, 6517A). The resistance data was manually collected at 10 V after holding at different temperature for 15 min. The resistivity R was calculated from

resistance according to the relationship: $\rho = \frac{RA}{d}$, where d and A are the thickness and the electrode area of the samples, respectively.

The polarization-electric field (*P-E*) and current-electric field (*I-E*) hysteresis loops were measured using a ferroelectric hystersis measurement tester (NPL, UK). Samples were immersed in silicone oil (SIL 300) which was heated up to 200 ℃. Triangular wave voltage up to 10 kV in the frequency range from 1 Hz to 200 Hz was applied to the sample for measurement. The *P-E* and *I-E* data were collected using a software programmed by NPL.

For piezoelectric measurements, samples were poled in silicon oil under various DC electric fields up to 20 kV. The silicon oil can be heated up to 200 ℃. The piezoelectric constant d_{33} of poled samples were measured using a quasi-static d_{33} meter ZJ-3B PIEZO d_{33} meter, Institute of Acoustics Academia Sinica, China). The accuracy of the d_{33} meter was calibrated using X-cut quartz ($d_{33} = 2.3 \pm 0.1$).

Chapter IV. Results - $A_nB_nO_{3n+2}$ Compounds

4.1 4-layer La$_{2-x}$Eu$_x$Ti$_2$O$_7$ and La$_{2-x}$Sm$_x$Ti$_2$O$_7$ Solid Solutions

4.1.1 Introduction

Some of the 4-layer Ln_2Ti$_2$O$_7$ (Ln = La, Ce, Pr, Nd) ceramics have been shown to be ferroelectric and piezoelectric active with super-high T_c.[7, 36] All of them have a perovskite-like layered structure with polar symmetry at room temperature. The structural stability of the Ln_2Ti$_2$O$_7$ compounds is determined by the ratio of the average ionic radii of the Ln^{3+} and Ti^{4+} cations. When r_{Ln3+} /r_{Ti4+} is greater than 1.80 (Ln = La to Nd), a perovskite-like layered structure with polar symmetry is stable at room temperature. When r_{Ln3+} /r_{Ti4+} is between 1.48 and 1.80 (Ln = Sm to Lu) a pyrochlore structure is preferred, which belongs to the centrosymmetric space group $Fd3m$.[9, 14, 87]

In this work, (A_xLa$_{1-x}$)$_2$Ti$_2$O$_7$ (A = Sm and Eu) solid solutions were prepared by solid state reaction and spark plasma sintering. A two-step SPS method was used to prepare textured ceramics. X-ray diffraction and Raman spectra technique were used to study the phase stability and phase boundary of the (A_xLa$_{1-x}$)Ti$_2$O$_7$ solid solution. The photoluminescent properties of (Sm$_x$La$_{1-x}$)$_2$Ti$_2$O$_7$ powders prepared by sol-gel method were reported by Shao, et al, before,[48] but in this paper, the effects of the Sm and Eu substitution on the on the dielectric, ferroelectric and piezoelectric properties of La$_2$Ti$_2$O$_7$ were studied.

4.1.2 Experimental Procedure

The $(Sm_xLa_{1-x})_2Ti_2O_7$ (x = 0, 0.1, 0.2, 0.5, 0.8, 0.9, 1) and $(Eu_xLa_{1-x})_2Ti_2O_7$ (x = 0, 0.2, 0.5, 0.6, 0.7, 0.8, 1) solid solutions were prepared by SSR. The starting materials were La_2O_3 (99.99%), Sm_2O_3 (99.9%), Eu_2O_3 (99.9%) and TiO_2 (99.8%). The stoichiometric mixtures of the oxides were ball milled with ethanol at 350 rpm for 3 h. The mixed powders were calcined using a conventional furnace. After that the calcined powders were ball milled at 350 rpm for 4 h to break any agglomerates and reduce the particle size. The calcined powders were sintered using a SPS furnace. A heating rate of 100 ℃/min was used in all cases. The $(A_xLa_{1-x})_2Ti_2O_7$ powders were sintered in a graphite die with a diameter of 20 mm for 3 min at different temperatures (1200 ℃ ~ 1300 ℃) under a pressure of 80 MPa in the SPS furnace. The textured ceramics were prepared using a two-step SPS process. [7, 12, 13] In the first step, the powders were sintered in a graphite die with a diameter of 20 mm for 3 min under a pressure of 80 MPa. In the second step, these sintered ceramics were placed in a graphite die with a diameter of 30 mm and sintered for 5 min under a pressure of 80 MPa. Finally, all of the sintered ceramics were annealed at 1200 ℃ for 15 h to remove any carbon contamination and reduction produced by SPS. For the textured ceramics, the direction of a plane with a normal line parallel to the SPS pressing direction is defined as the parallel direction (//) and the normal line perpendicular to the pressing direction is the perpendicular direction (⊥).

4.1.3 Results and Discussion

Fig. 4.1.1 shows the XRD patterns of $(Eu_xLa_{1-x})_2Ti_2O_7$ ($x = 0$, 0.2, 0.5, 0.6, 0.7, 0.8, 1) powders. $La_2Ti_2O_7$ ($x = 0$) has the typical PLS monoclinic structure (shown in Fig. 4.1.3(a) and (b)), while $Eu_2Ti_2O_7$ ($x = 1$) has the cubic pyrochlore structure. For $x = 0.2$ and 0.5, they are single phase with the same structure as $La_2Ti_2O_7$. For $x = 0.6 \sim 0.8$, they are biphase. A small peak around $50°$ corresponding to the (4 4 0) planes of the cubic phase can be found in the diffraction pattern of the $x = 0.6$ sample. The peak becomes stronger with increasing of Eu/La ratio (increasing x). Fig. 4.1.2 shows the XRD patterns of $(Sm_xLa_{1-x})_2Ti_2O_7$ ($x = 0$, 0.1, 0.2, 0.5, 0.8, 0.9, 1) powders. Like $Eu_2Ti_2O_7$, $Sm_2Ti_2O_7$ ($x = 1$) has the same cubic pyrochlore structure (shown in Fig. 4.1.3(c)). For $x = 0 \sim 0.8$, they are single phase with the PLS structure. For $x = 0.9$, it is biphase. The solubility limit of $(Sm_xLa_{1-x})_2Ti_2O_7$ powders prepared by SSR is similar to that of $(Sm_xLa_{1-x})_2Ti_2O_7$ powders prepared by sol-gel.[48] Comparing the solid solutions of $(Eu_xLa_{1-x})_2Ti_2O_7$ and $(Sm_xLa_{1-x})_2Ti_2O_7$, the solid solubility of Sm^{3+} in $La_2Ti_2O_7$ is higher than that of Eu^{3+}. One possible reason for this is that the ionic radius of Sm^{3+} (1.24 Å) is a little larger than that of Eu^{3+} (1.206 Å), and closer to the ionic radius of La^{3+} (1.360 Å).[88] Table 4.1.1 shows the Full Width of Half Maximum (FWHM) of the (2 1 1) peak of the monoclinic structure and the (2 2 2) peak of the cubic structure. For $(Eu_xLa_{1-x})_2Ti_2O_7$ ($x = 0.6$, 0.7 and 0.8) with biphase, the (2 1 1) peak is actually a sum-peak of the (2 1 1) peaks of the monoclinic structure and the (2 2 2) peaks of cubic structure due to their similar d spacing in the solid solutions. For $(Sm_{0.9}La_{0.1})_2Ti_2O_7$ with biphase, the (2 1 1) peak and the (2 2 2) peak are clearly separated. Broad peaks were observed from $(Eu_{0.6}La_{0.4})_2Ti_2O_7$ and $(Sm_{0.8}La_{0.2})_2Ti_2O_7$ at the phase boundary. The peak broadening is caused by the disordered structure in the solid solutions. Fig. 4.1.4 shows the diffraction peak position versus x of the (0 4 0) and (2 1 1) planes of the monoclinic structure and (2 2 2) planes of the cubic structure from the XRD results of

$(A_x La_{1-x})_2 Ti_2 O_7$ solid solutions. For $(Sm_x La_{1-x})_2 Ti_2 O_7$, With increasing x, the position of the (0 4 0) peak remains in the same while the position of the (2 1 1) peak increases linearly. For $x = 0.9$, the position of the (2 1 1) peak is linear with that of the compositions with $x < 0.9$ and the position of the (2 2 2) peak is in the same position as that of the pure $Sm_2 Ti_2 O_7$, which means the biphase found at composition $x=0.9$ consists of $(Sm_x La_{1-x})_2 Ti_2 O_7$ with monoclinic PLS structure and pure $Sm_2 Ti_2 O_7$ with pyrochlore structure. For $(Eu_x La_{1-x})_2 Ti_2 O_7$, when x is less than 0.6 the position of the (0 4 0) and (2 1 1) peaks show a similar trend with that of $(Sm_x La_{1-x})_2 Ti_2 O_7$. When x is greater than 0.6, the position of the (2 1 1) peak does not follow a linear trend, because the (2 1 1) peak is a sum-peak of the (2 1 1) peak of the monoclinic structure and the (2 2 2) peak of the cubic structure for the biphase structure. To clearly understand the biphase structure in $(Eu_x La_{1-x})_2 Ti_2 O_7$, the change of the position of the (4 4 0) peak of the cubic phase is shown in Table 4.1.2. The positions of the (4 4 0) peak for $x = 0.7$ and 0.8 are lower than that of pure $Eu_2 Ti_2 O_7$ ($x = 1$), which means that the cubic phase in the biphase structure is a La^{3+} doped $Eu_2 Ti_2 O_7$ solid solution. Because the radius of La^{3+} is larger than that of Eu^{3+}, the diffraction peaks of cubic $Eu_2 Ti_2 O_7$ shift to lower angles when La^{3+} replaced Eu^{3+} in the crystal structure. For $(Sm_x La_{1-x})_2 Ti_2 O_7$, the (4 4 0) peaks of $x = 0.9$ and $x = 1$ are in the same position (50.42 °), which means the cubic phase at $x = 0.9$ is pure $Sm_2 Ti_2 O_7$. This is consistent with the previous discussion on Fig. 4.1.4.

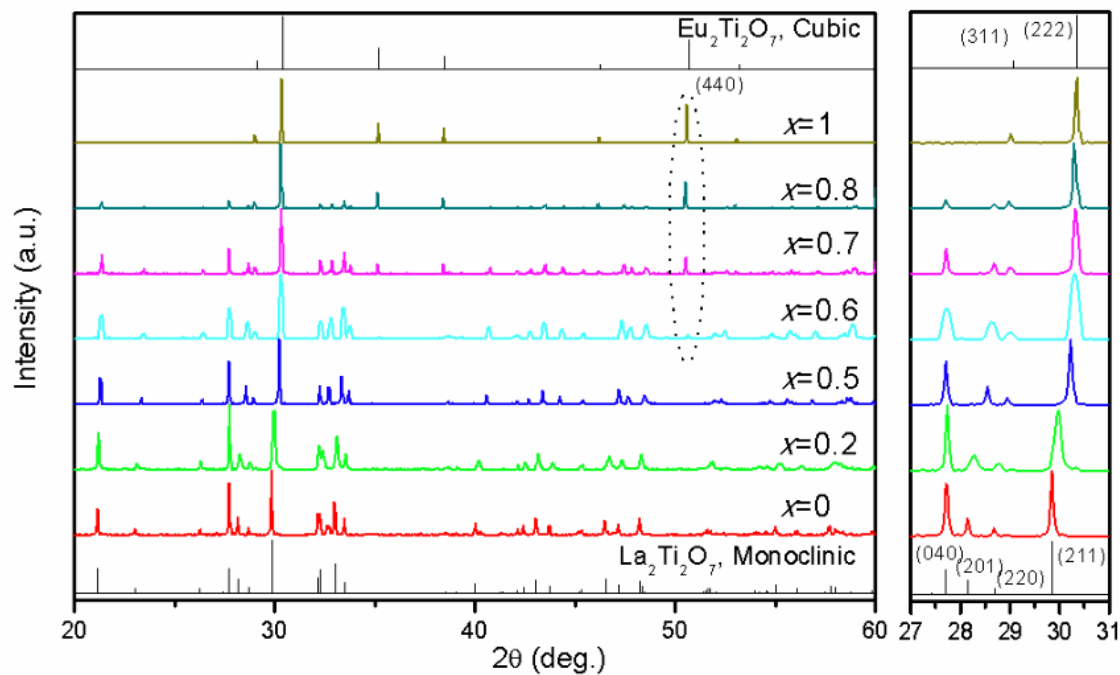Fig. 4.1.1 XRD patterns of $(Eu_xLa_{1-x})_2Ti_2O_7$ (x = 0, 0.2, 0.5, 0.6, 0.7, 0.8, 1) powders.
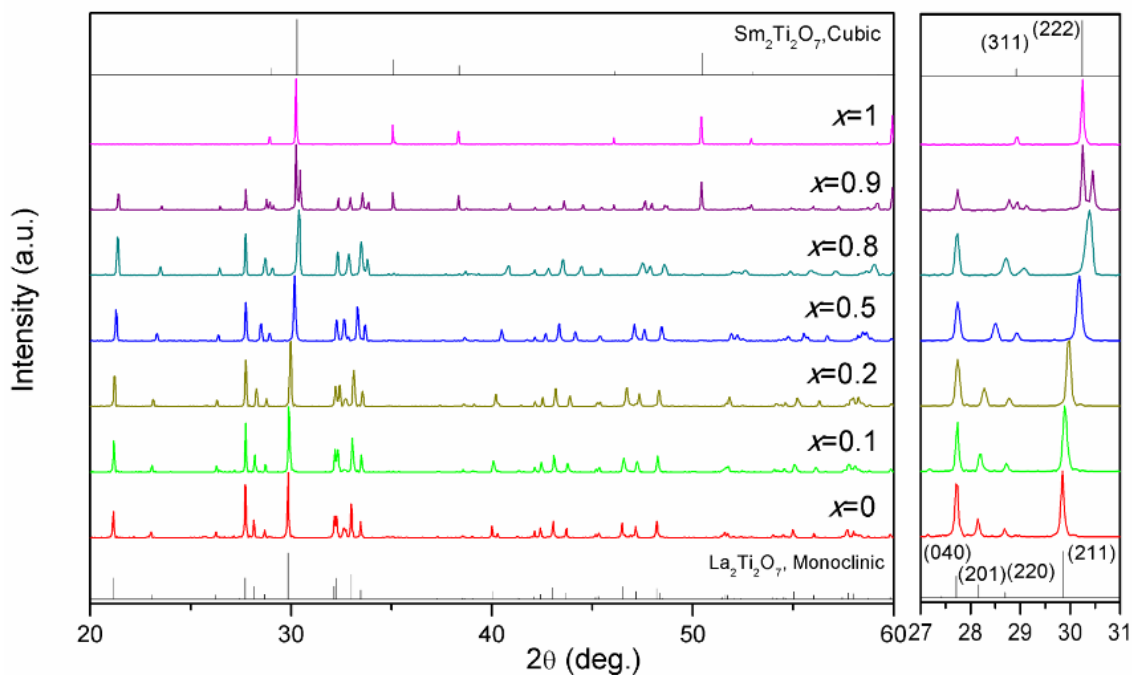

Fig. 4.1.2 XRD patterns of $(Sm_xLa_{1-x})_2Ti_2O_7$ (x = 0, 0.1, 0.2, 0.5, 0.8, 0.9, 1) powders.

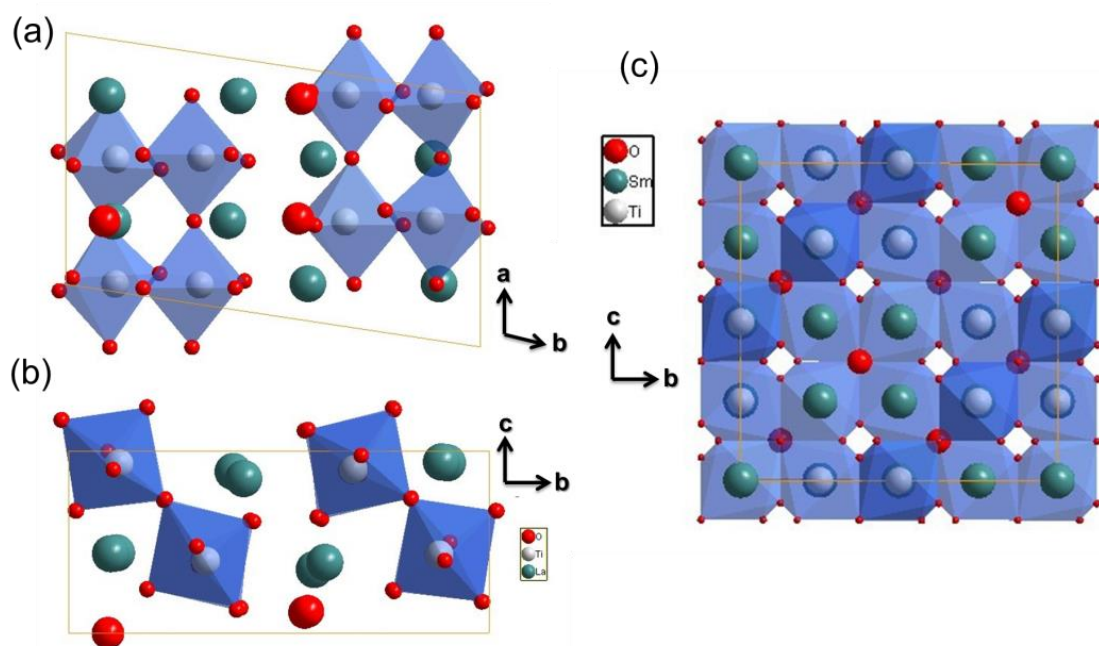Fig. 4.1.3 Crystal structures of PLS La$_2$Ti$_2$O$_7$ along the (a) *a-c* and (b) *b-c* projection and pyrochlore Sm$_2$Ti$_2$O$_7$ along the (c) *a-c* projection.

Table 4.1.1 Full with of half maximum (FWHM) of the (1 1 2) peak of the monoclinic structure and the (2 2 2) peak of the cubic structure for (Eu$_x$La$_{1-x}$)$_2$Ti$_2$O$_7$ and (Sm$_x$La$_{1-x}$)$_2$Ti$_2$O$_7$ solid solutions

(Eu$_x$La$_{1-x}$)$_2$Ti$_2$O$_7$	$x = 0$	$x = 0.2$	$x = 0.5$	$x = 0.6$	$x = 0.7$	$x = 0.8$	$x = 1$
(2 1 1) (°)	0.134	0.152	0.089	0.161	0.102	0.080	/
(2 2 2) (°)	/	/	/	/	/	/	0.068
(Sm$_x$La$_{1-x}$)$_2$Ti$_2$O$_7$	$x = 0$	$x = 0.1$	$x = 0.2$	$x = 0.5$	$x = 0.8$	$x = 0.1$	$x = 1$
(2 1 1) (°)	0.134	0.1	0.105	0.115	0.145	0.073	/
(2 2 2) (°)	/	/	/	/	/	0.063	0.061

Table 4.1.2 Diffraction Peak position for (4 4 0) of cubic structure for $(Eu_xLa_{1-x})_2Ti_2O_7$ and

$(Sm_xLa_{1-x})_2Ti_2O_7$

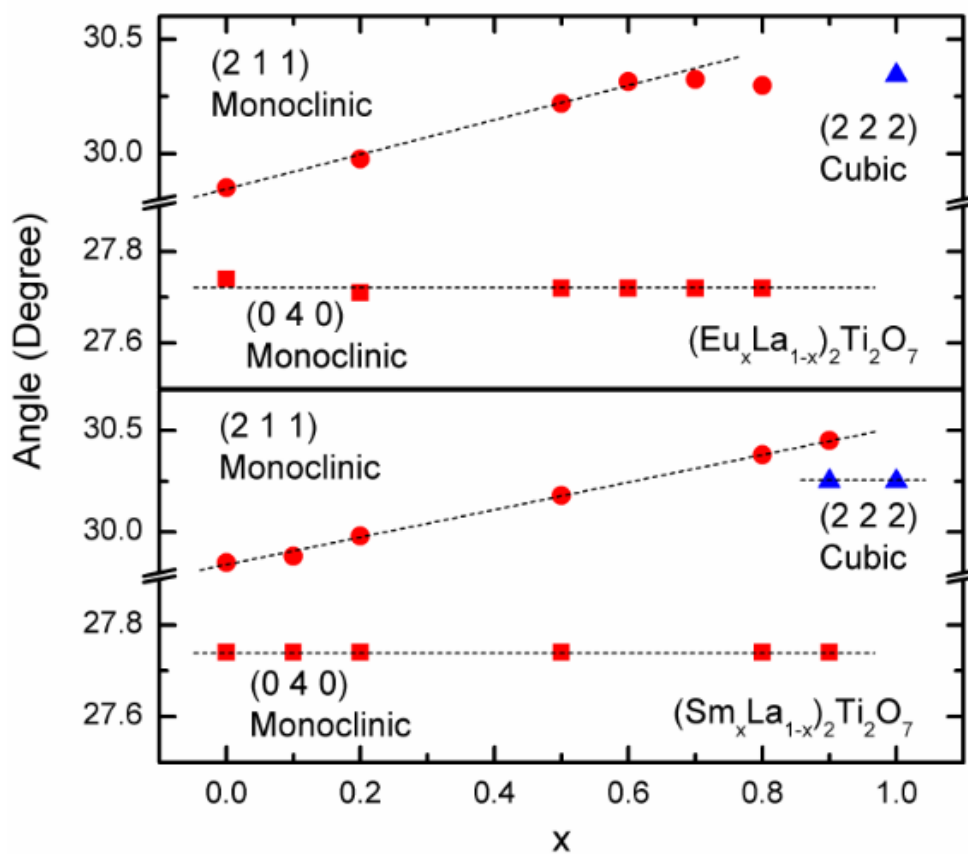| Solid solutions	$(Eu_xLa_{1-x})_2Ti_2O_7$			$(Sm_xLa_{1-x})_2Ti_2O_7$	
	$x = 0.7$	$x = 0.8$	$x = 1$	$x = 0.9$	$x = 1$
(4 4 0) (°)	50.525	50.509	50.573	50.42	50.42

Fig. 4.1.4 The diffraction peak position versus *x* of the (0 4 0) and (2 1 1) planes of monoclinic

structure and (2 2 2) plane of cubic structure from the XRD results of $(A_xLa_{1-x})_2Ti_2O_7$ solid

solutions.

Fig. 4.1.5 shows the Raman spectra of $(A_x La_{1-x})_2 Ti_2 O_7$ powders. The Raman spectra of $Eu_2 Ti_2 O_7$ and $Sm_2 Ti_2 O_7$ are very different to other spectra due to their pyrochlore structure. There are six active Raman modes, A_{1g}, E_g and $4F_{2g}$, for the pyrochlore structure from group theoretical analysis.[89] The peaks at 343 cm^{-1} ($Eu_2 Ti_2 O_7$) and 319 cm^{-1} ($Sm_2 Ti_2 O_7$), containing two modes (E_g + F_{2g}), correspond to the bending of the O-Eu-O bond and O-Sm-O, respectively. The modes (A_{1g}) at 531 cm^{-1} ($Eu_2 Ti_2 O_7$) and 518 cm^{-1} ($Sm_2 Ti_2 O_7$) correspond to the stretching of the Eu-O and Sm-O bonds.[37] Compared with $Eu_2 Ti_2 O_7$ and $Sm_2 Ti_2 O_7$, the spectrum of $La_2 Ti_2 O_7$ ($x = 0$) shows more phonon modes due to various La-O and Ti-O vibrations.[90] It exhibits intense phonon modes at 343, 371, 405, 430, 448, 520, 541, 559, 609 and 795 cm^{-1}, which are related to the monoclinic structure. The mode at 343 cm^{-1} is related to the La-O vibration, the modes at 448, 609 and 795 cm^{-1} correspond to the stretching of oxygen in the octahedral O-Ti-O chain. For most of the layered perovskite-related materials, the modes above ~200 cm^{-1} are associated with the $B O_6$ octahedra. [91-93] For the sample $(Sm_{0.9} La_{0.1})_2 Ti_2 O_7$ ($x = 0.9$), the modes from both the monoclinic structure and pyrochlore structure can be observed. The positions of the modes from the monoclinic phase follow the change of the solid solutions, while the modes from the pyrochlore phase are similar to pure $Sm_2 Ti_2 O_7$. This is consistent with the previous discussion, that the biphase at $x=0.9$ consists of $(Sm_x La_{1-x})_2 Ti_2 O_7$ with monoclinic PLS structure and pure $Sm_2 Ti_2 O_7$ with cubic pyrochlore structure. For the sample $(Eu_{0.8} La_{0.2})_2 Ti_2 O_7$ ($x = 0.8$), the modes from the pyrochlore phase are shifted to lower wavenumber compared with pure $Eu_2 Ti_2 O_7$, which agrees with the previous discussion (Table 4.1.2) that the pyrochlore phase in the biphase structure is not pure $Eu_2 Ti_2 O_7$, but La^{3+} doped $Eu_2 Ti_2 O_7$. With increasing x, for both $(Eu_x La_{1-x})_2 Ti_2 O_7$ and $(Sm_x La_{1-x})_2 Ti_2 O_7$, the intensities of the modes at 448, 609 and 795cm^{-1} decrease and the peaks become broad, which means a reduction of the TiO_6 distortion. A change in the peak positions and intensity of the other modes can also be

observed. When La^{3+} in $La_2Ti_2O_7$ with monoclinic structure is substituted by Eu^{3+} or Sm^{3+}, there is a change of the mass and ionic radii of the A-site elements, so that the force constant changes due to the change in the bond length and lattice parameters and the Raman modes in the perovskite unit cell shift.[93]
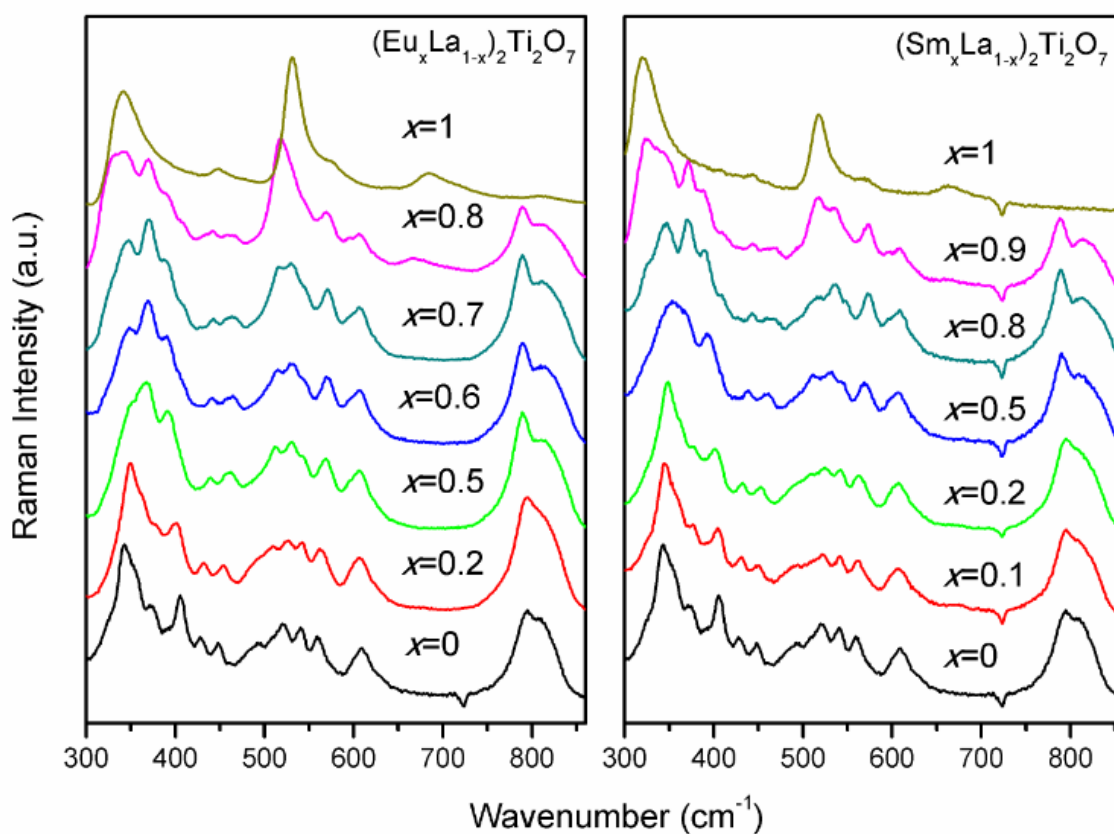

Fig. 4.1.5 Raman spectra of $(A_xLa_{1-x})_2Ti_2O_7$ powders at room temperature.

Fig. 4.1.6 shows the XRD pattern of textured $(Sm_{0.2}La_{0.8})_2Ti_2O_7$ ceramic. The diffraction pattern of the plane parallel to the SPS pressing direction shows a strong (0 k 0) diffraction peaks, while the pattern for the plane perpendicular to the SPS pressing direction shows weak (0 k 0) peaks and strong (h 0 l) peaks, which indicates that the ceramic is highly textured. The grain orientation factor (f) of the (0k0) planes is

calculated by the Lotgering method using the following equations: $f = \frac{P-P_0}{1-P_0}$, $P_0 = \frac{I_0(0k0)}{\sum I_0(hkl)}$, $P = \frac{I(0k0)}{\sum I(hkl)}$ where P and P_0 are the integrated intensities of all $(0k0)$ planes and all (hkl) planes for preferentially and randomly oriented samples, respectively.[7] The orientation factor f for the plane parallel to the pressing direction of $(Sm_{0.2}La_{0.8})_2Ti_2O_7$ ceramic is approximately 0.71. Fig. 4.1.7 shows SEM images of textured $(Sm_{0.2}La_{0.8})_2Ti_2O_7$ ceramic from the surfaces perpendicular (Fig. 4.1.7(a)) and parallel (Fig. 4.1.7(b)) to the SPS pressing direction. The plate-like grains are oriented perpendicular to the SPS pressing direction. This is consistent with the XRD results in Fig. 4.1.6. The plate-like grains are about 2~3 μm in thickness and 5~10 μm in the other two dimensions.

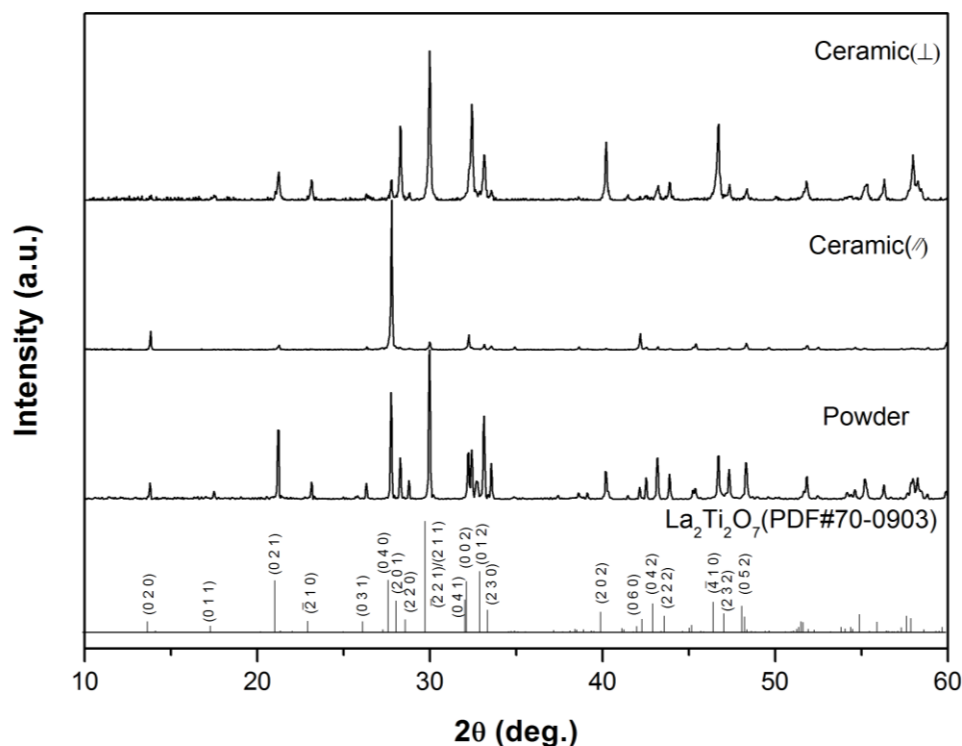Fig. 4.1.6 XRD patterns of $(Sm_{0.2}La_{0.8})_2Ti_2O_7$ powder and textured ceramic.
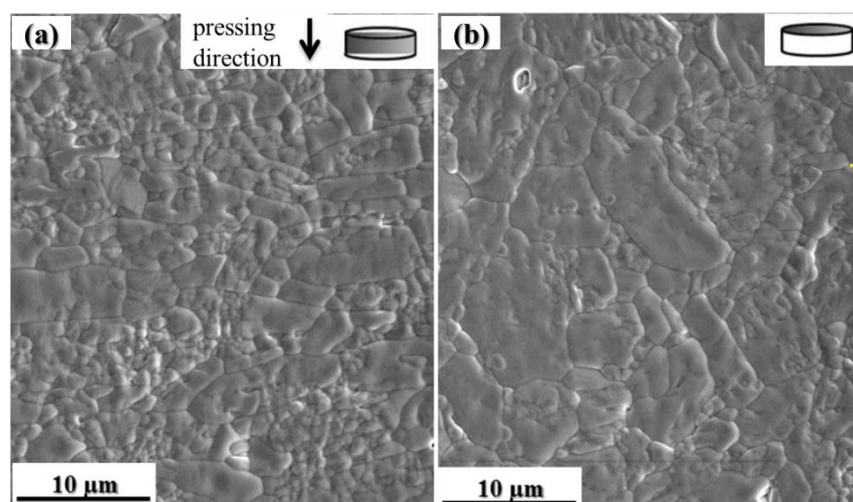
Fig. 4.1.7 SEM images of textured $(Sm_{0.2}La_{0.8})_2Ti_2O_7$ ceramic: (a) the surface with normal line perpendicular to the pressing direction; (b) the surface with normal line parallel to the pressing direction.

Fig. 4.1.8(a) shows the frequency dependence of the permittivity and loss at room temperature for untextured $(Sm_xLa_{1-x})_2Ti_2O_7$ (x = 0, 0.1, 0.2, 0.5, 0.8, 0.9 and 1) ceramics. Like other PLS materials, both the permittivity and loss are almost frequency independent and the losses are very low in the frequency range from 10^3 to 10^7 Hz for all of the compositions.[94, 95] For $(Sm_{0.2}La_{0.8})_2Ti_2O_7$, the permittivity and loss slightly increase with decreasing frequency, especially in the low frequency range from 10^4 to 10^3 Hz. Although the permittivity of $(Sm_{0.2}La_{0.8})_2Ti_2O_7$ is lower than that of $(Sm_{0.5}La_{0.5})_2Ti_2O_7$, in general, A-site Sm substitution of $La_2Ti_2O_7$ reduces its intrinsic permittivity. Fig. 4.1.8(b) shows the frequency dependence of permittivity and loss for the textured $(Sm_xLa_{1-x})_2Ti_2O_7$ (x = 0, 0.1 and 0.2) ceramics measured at room temperature along the surface perpendicular to the SPS pressing direction. After texturing, the losses for all of the ceramics are still very low from 10^4 to 10^3 Hz, Compared with untextured ceramics (Fig. 4.1.8(a)), textured ceramics show higher permittivity along the plane perpendicular to the SPS pressing direction due to the anisotropy of the layered perovskite structure. The anisotropy of the PLS materials were

firstly observed for single crystal. For the $La_2Ti_2O_7$ single crystal, the permittivity along the *a*-axis (52) and the *c*-axis (62) are higher than that along *b*-axis (42, perpendicular to the layers).[11]
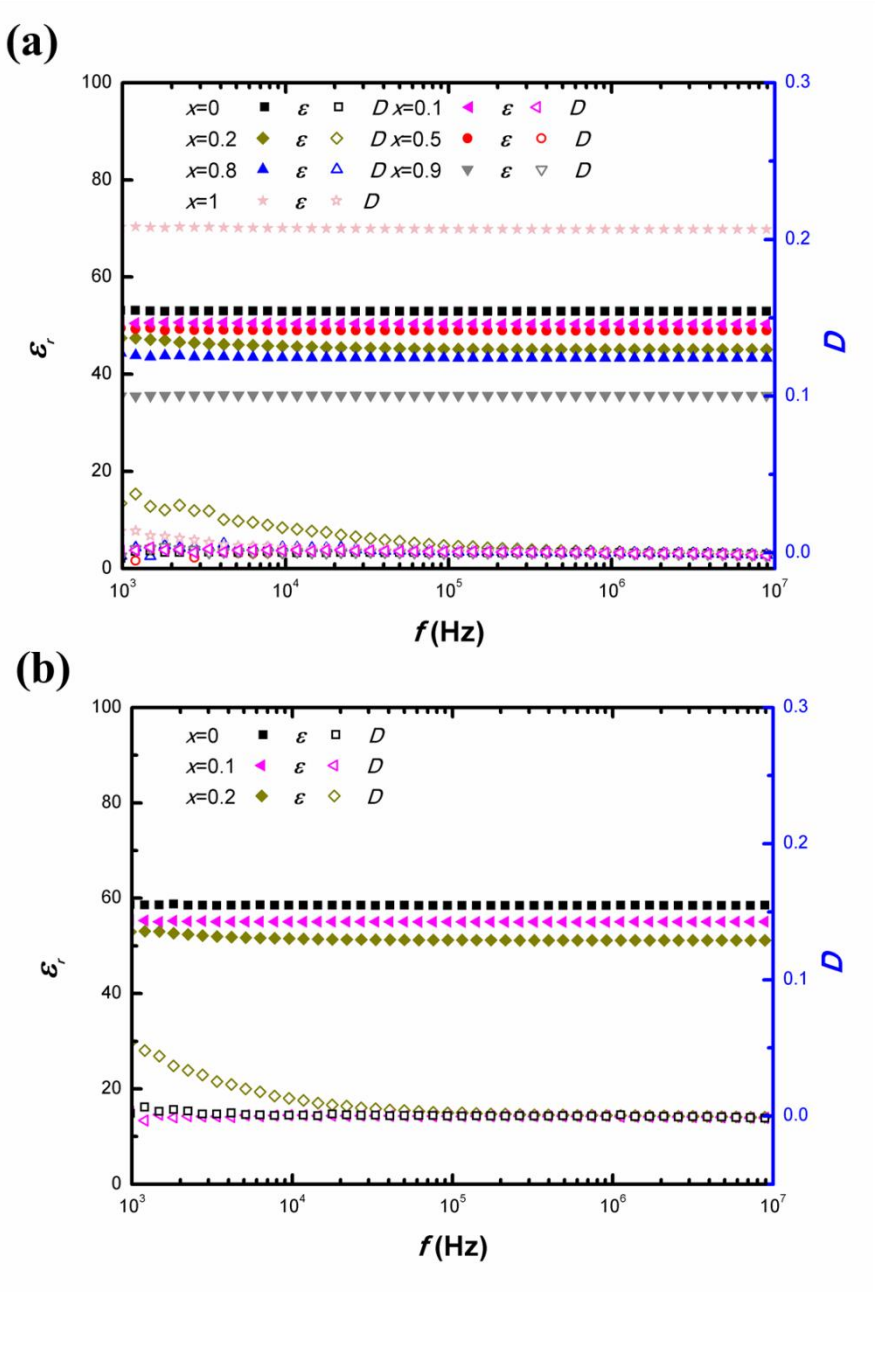

Fig. 4.1.8 Frequency dependence of permittivity and loss at room temperature: (a) untextured $(Sm_xLa_{1-x})_2Ti_2O_7$ ($x = 0, 0.2, 0.5, 0.8, 0.9, 1$) ceramics; (b) textured $(Sm_xLa_{1-x})_2Ti_2O_7$ ($x = 0, 0.1, 0.2$) ceramics measured from the surface perpendicular to the pressing direction

Fig. 4.1.9 shows the temperature dependence of the permittivity and loss of $(Sm_{0.2}La_{0.8})_2Ti_2O_7$ measured at different frequencies. The permittivity is very stable up to 1300 °C and then increases dramatically on approaching T_c (~ 1430 °C). The loss peaks just below T_c are attributed to ferroelectric domain wall movement.[96, 97] The permittivity peaks observed in the inset of Fig. 4.1.9 between 600 to 1000 °C might be due to possible point defects, as the permittivity peaks produced by a phase transition are normally frequency independent. According to N. Ishizawa's report,[42] there is a phase transition from $P2_1$ to $Cmc2_1$ at approximately 780 °C for pure $La_2Ti_2O_7$, which is not observed here. One possible reason is that the change of permittivity is not obvious due the small change of spontaneous polarization between $P2_1$ and $Cmc2_1$. The T_c of $La_2Ti_2O_7$ ($x = 0$) is about 1450 °C, which is similar with previous reports.[7, 11] The T_c data are plotted versus tolerance factor in Fig. 4.1.10 to clearly show the variation of T_c with the changing of A-site substitution in $La_2Ti_2O_7$. Tolerance factor (t), which is defined as $t = \frac{1}{\sqrt{2}} \cdot \frac{r_A + r_O}{r_B + r_O}$ where r_A, r_B and r_O are ionic radii of A, B and O ions, is used to analyse structural stability of ceramics with perovskite structure (ABO_3).[98] The tolerance factor can also be used to analyse their physical properties. The phase transitions between ferroelectric phase and paraelectric phase for PLS materials are related to the structural distortion of BO_6 octahedra, which can be quantified using the tolerance factor. The relation between perovskite tolerance factor and T_c of Aurivillius materials was studied before.[99] Here tolerance factor is introduced to analyse the T_c change of the $(A_xLa_{1-x})Ti_2O_7$ solid solutions. With increasing Sm and Eu substitution, the T_c decreases gradually with decreasing tolerance factor. For $La_2Ti_2O_7$, the ferroelectric phase at room temperature has a monoclinic structure $P2_1$ as shown in Fig. 4.1.3(a) and (b). Its corresponding paraelectric phase has an orthorhombic structure $Cmcm$. The structure change from paraelectric phase $Cmcm$ to ferroelectric phase $P2_1$ can be regarded as a combination of a rotation along the a axis and a tilt along the b

axis.[14, 42] As discussed previously, the ionic radius of Sm^{3+} and Eu^{3+} are smaller than that of La^{3+} when Sm^{3+} or Eu^{3+} occupy the position of La^{3+} in the unit cell, and the degree of rotation and tilt of the TiO_6 octahedra is reduced,[100] which is also observed form the analysis of the Raman spectra. This means that the structure is easier to transform to the paraelectric phase.[101] Consequently, the T_c becomes lower with increasing Sm and Eu substitution. The SPSed $Sm_2Ti_2O_7$ and $Eu_2Ti_2O_7$ have a centrosymmetric pyrochlore structure. The T_c of the high-pressure phases $Sm_2Ti_2O_7$ and $Eu_2Ti_2O_7$ ceramics were estimated to be about 1077 ℃ and 1247 ℃, respectively, by studying the second harmonic signal temperature dependence.[37, 39] The lower Curie points of the high pressure phases are consistent with that of their high Sm and Eu content solid solutions as shown in Fig. 4.1.10.
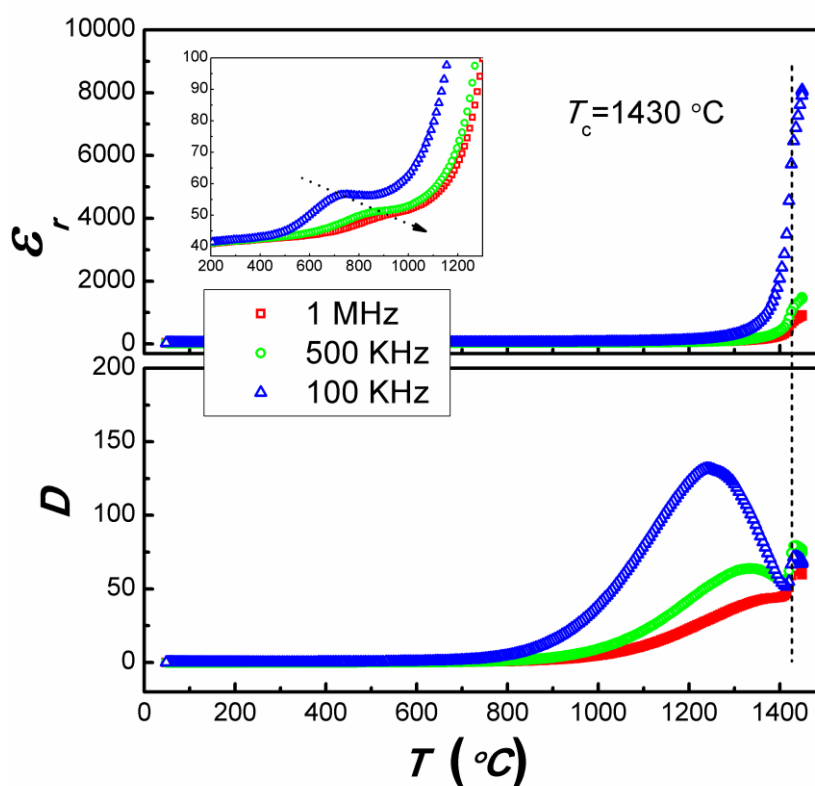

Fig. 4.1.9 Temperature dependence of permittivity and loss of $(Sm_{0.2}La_{0.8})_2Ti_2O_7$ ceramic. The inset shows the permittivity in the temperature range from 200 to 1400 ℃.
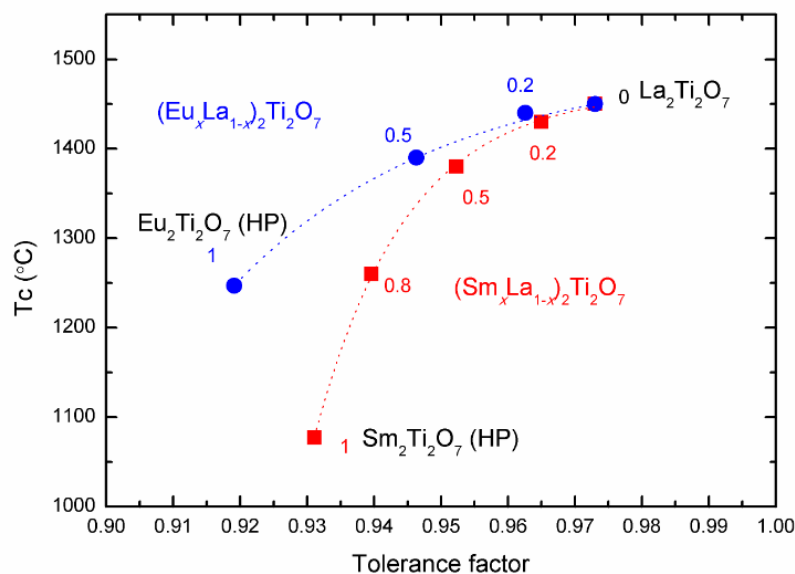
Fig. 4.1.10 Variation in Curie point with $(A_xLa_{1-x})_2Ti_2O_7$ solid solutions (HP: high-pressure

phase)

Fig. 4.1.11 shows the current-electric field (*I-E*) and polarization-electric field (*P-E*) hysteresis loops for textured $(Sm_xLa_{1-x})_2Ti_2O_7$ (*x* = 0, 0.1 and 0.2) ceramics measured along the direction perpendicular to the SPS pressing direction at 200 ℃ at 10 Hz. There are clear current peaks corresponding to ferroelectric switching between 50 and 100 kV/cm for $La_2Ti_2O_7$ (*x* = 0). It was not possible to obtain a saturated *P-E* loop due to the high coercive field. For $(Sm_{0.1}La_{0.9})_2Ti_2O_7$ (*x* = 0.1), double current peaks are observed in the *I-E* loops with increasing voltage. The peaks produced at lower field are probably produced by defects dipole, while the peaks produced at the higher field are attributed to ferroelectric domain switching. For $(Sm_{0.2}La_{0.8})_2Ti_2O_7$ (*x* = 0.2), only one unobvious current peak can be observed. For textured $(Eu_xLa_{1-x})_2Ti_2O_7$ (*x* = 0.2 and 0.5) ceramics, no peaks were be observed in *I-E* loops.
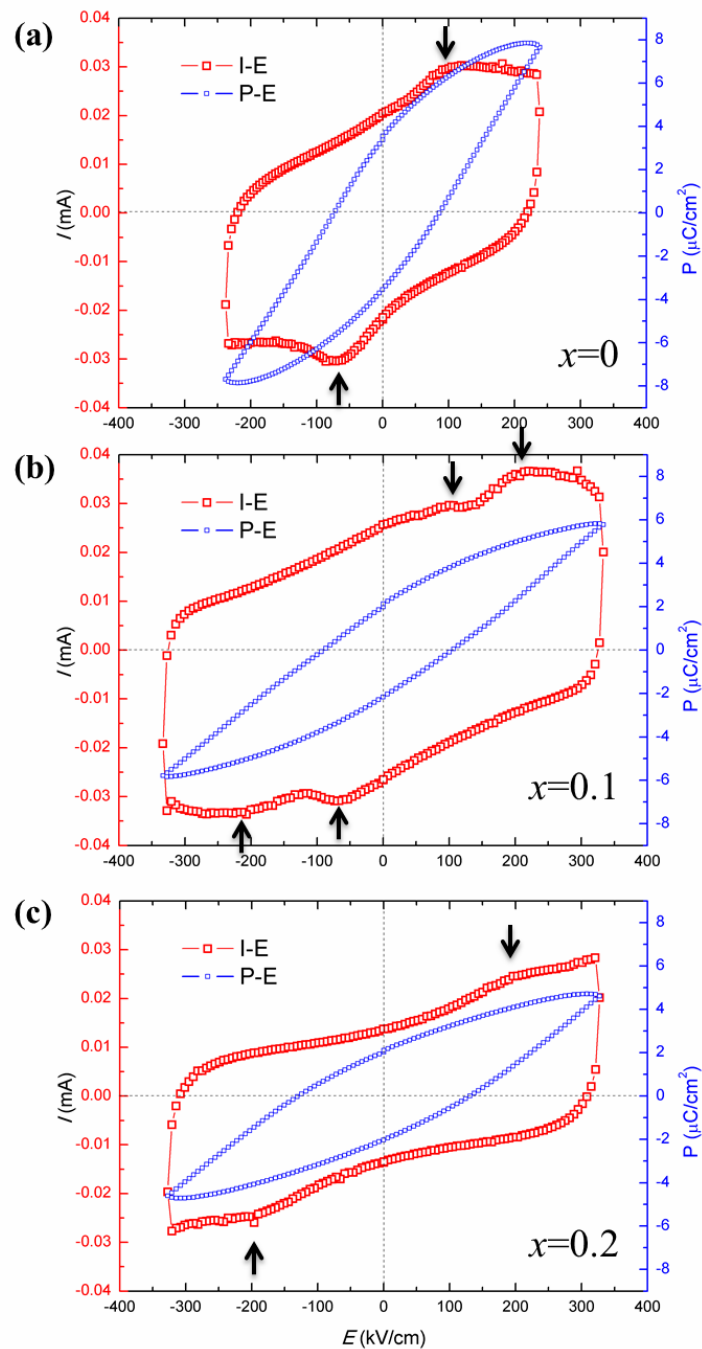
Fig. 4.1.11 Current-electric field (*I-E*) and polarization-electric field (*P-E*) hysteresis loops of textured $(Sm_xLa_{1-x})_2Ti_2O_7$ ceramics along the direction perpendicular to the pressing direction measured at 200 ℃: (a) $x = 0$, (b) $x = 0.1$ and (c) $x = 0.2$. The arrows show the current peaks caused by ferroelectric domain switching (The arrows at lower field in Fig (b) show the current peaks probably produced by defects dipole).

Table 4.1.3 shows the piezoelectric constant d_{33} of the textured $(Sm_xLa_{1-x})_2Ti_2O_7$ ($x = 0$, 0.1 and 0.2) ceramics. All of the ceramics were poled in silicon oil at 200 °C under various DC electric fields (200-350 kV/cm) in a direction perpendicular to the SPS pressing direction. The average d_{33} of pure $La_2Ti_2O_7$ is around 1.6 pC/N. $(Sm_{0.1}La_{0.9})_2Ti_2O_7$ has a higher d_{33} of 2.8 pC/N. With further increasing the content of Sm, the d_{33} dropped to 2.2 pC/N for $(Sm_{0.2}La_{0.8})_2Ti_2O_7$. For textured $(Eu_xLa_{1-x})_2Ti_2O_7$ ($x = 0.2$ and 0.5) ceramics, no piezoelectric constant d_{33} could be measured and after poling.

Table 4.1.3 Piezoelectric constant d_{33} of textured $(Sm_xLa_{1-x})_2Ti_2O_7$ ceramics measured along the direction perpendicular to the SPS pressing direction. All of the ceramics were poled in silicon oil at 200 °C under various DC electric fields (200-350 kV/cm).

x	0	0.1	0.2
orientation factor f	0.8	0.73	0.71
d_{33} (pC/N)	1.6	2.8	2.2

4.1.4 Conclusions

$(A_x La_{1-x})Ti_2O_7$ (A = Sm and Eu) solid solutions were successfully prepared by SSR and SPS. $(A_x La_{1-x})Ti_2O_7$ solid solutions were isomorphous with $La_2Ti_2O_7$ when x was less than 0.5 for $(Eu_x La_{1-x})Ti_2O_7$ and 0.8 for $(Sm_x La_{1-x})Ti_2O_7$. When x was above their solubility limit, a biphase was observed. The XRD and Raman data indicate that the biphase of $(Sm_x La_{1-x})Ti_2O_7$ (x = 0.9) consisted of $(Sm_x La_{1-x})_2Ti_2O_7$ with PLS structure and pure $Sm_2Ti_2O_7$ with pyrochlore structure, and the biphase of $(Eu_x La_{1-x})Ti_2O_7$ (x =0.6, 0.7 and 0.8) consisted of $(Eu_x La_{1-x})_2Ti_2O_7$ with PLS structure and La^{3+} doped $Eu_2Ti_2O_7$ with pyrochlore structure. With increasing Sm and Eu substitution at $(A_x La_{1-x})_2Ti_2O_7$, the tolerance factor decreased and the rotation and tilt of the TiO_6 octahedra were supposed to be reduced, so that the T_c decreased gradually. For highly textured ceramics obtained using a 2-step SPS method, ferroelectric domain switching was observed in the *I-E* and *P-E* hysteresis loops for $(Sm_x La_{1-x})Ti_2O_7$ (x < 0.2). The highest d_{33} was 2.8 pC/N for $(Sm_{0.1}La_{0.9})Ti_2O_7$. No ferroelectric domain switching and d_{33} were observed for the textured $(Eu_x La_{1-x})Ti_2O_7$ (x = 0.2 and 0.5) ceramics.

4.2 3-layer Pr$_3$Ti$_2$TaO$_{11}$ Compound

4.2.1 Introduction

Some of the 4-layer PLS $A_2B_2O_7$ compounds and their solid solutions have been widely studied and demonstrated to be ferroelectrics, but the 3-layer PLS $A_3B_3O_{11}$ compounds are largely unexplored and it was not previously reported if they are ferroelectrics. For n = 3 compounds there are two different types of structure. So far only Titov *et al*. reported that Sr$_2$LaTa$_3$O$_{11}$ has the centrosymmetric type I structure and La$_3$Ti$_2$TaO$_{11}$ and Pr$_3$Ti$_2$TaO$_{11}$ have the non-centrosymmetric type II structure.[15-17] They mentioned that A$_3$B$_3$O$_{11}$ compounds with type II structure like La$_3$Ti$_2$TaO$_{11}$ and Pr$_3$Ti$_2$TaO$_{11}$ can present ferroelectricity, however, their works are based only on powder diffraction, and no information on the microstructure and ferroelectric properties of ceramics of n = 3(II) type compounds was reported. The aim of this work is to prepare the Pr$_3$Ti$_2$TaO$_{11}$ ceramic with type II structure and try to study its microstructure and potential ferroelectric properties.

In this chapter, Pr$_3$Ti$_2$TaO$_{11}$ powders were prepared by solid state reaction (SSR) and co-precipitation (CP) methods. SPS was used to fabricate dense and textured ceramics. The crystal structure and microstructure of the 3-layer PLS compound Pr$_3$Ti$_2$TaO$_{11}$ were studied and its dielectric properties and T_c are reported for the first time.

4.2.2 Experimental Procedure

SSR and CP methods were used to obtain the crystalline $Pr_3Ti_2TaO_{11}$ powders. For SSR, the starting materials were Pr_6O_{11} (99.9%), TiO_2 (99.9%) and Ta_2O_5 (99.85%). Stoichiometric mixtures of the oxides were ball milled with ethanol at 350 rpm for 3 h. A two-step calcination process was used. The powder mixtures were first calcined at 1200 °C for 4 h. The calcined powders were then re-ball-milled at 350 rpm for 4h and then calcined again at 1400 °C for 4 h. Finally, the calcined powders were ball milled at 350 rpm for 4 h to break agglomerates and reduce the particle size. For co-precipitation, $Pr(NO_3)_3 \cdot 6H_2O$ (99.9%), $Ti(OCH_9)_4$ (97%) and $TaCl_5$ (99.8%) were used as the starting precursors, and an ammonia water solution was used as the precipitator. Stoichiometric amounts of the precursor compounds to prepare 5 g of $Pr_3Ti_2TaO_{11}$ were dissolved in ethanol (100 cm^3) at room temperature, with stirring for 12 h. Ammonia solution (10 cm^3 concentrated ammonia in 100 cm^3 ethanol) was added dropwise, resulting in precipitation. During this process the pH was maintained above 9 by addition of a few drops of aqueous concentrated ammonia. The precipitate was centrifuged to separate it from the liquid which was decanted off. The precipitate was then rinsed three times with deionized water and finally once with ethanol, before drying at 80 °C.[7, 15, 81] The dried precipitate was calcined at 1300 °C for 4 h.

The calcined powders were sintered using SPS. A heating rate of 100 °C /min was used in all cases. The sintering temperatures were determined from the shrinkage curve of a sample heated up to 1500 °C under a pressure of 16 MPa. The $Pr_3Ti_2TaO_{11}$ powders prepared by SSR and CP were sintered in a 20 mm diameter graphite die for 3 min at 1500 and 1350 °C, respectively, under a pressure of 80 MPa in the SPS furnace. The textured ceramics were prepared using a two-step SPS process.[7, 12, 13] In the first step, the powders prepared by SSR and CP were sintered in a 20 mm diameter graphite die

for 3 min under a pressure of 80 MPa at 1350 and 1250 °C, respectively. In the second step, the sintered ceramics were placed in a 30 mm diameter graphite die and sintered for 5 min under a pressure of 80 MPa at 1450 and 1400 °C for the SSR and CP prepared samples, respectively. Finally, the sintered ceramics were annealed in air at 1200 °C for 15 h to remove any carbon contamination and reduction produced by SPS.

4.2.3 Results and Discussion

Fig. 4.2.1(a) shows the X-ray diffraction (XRD) pattern of the $Pr_3Ti_2TaO_{11}$ powder prepared by CP. The detail of the crystal data and Rietveld refinement parameters are given in Table 4.2.1. Preliminary structural analysis by Rietveld refinement using the n = 3 (II) type structure of $La_3Ti_2TaO_{11}$ [16] as a starting model confirmed an orthorhombic structure with space group $Pmc2_1$. The inset of Fig. 4.2.1(a) shows the second harmonic generation (SHG) result for powders prepared by CP. A strong SHG signal was detected, which confirms that $Pr_3Ti_2TaO_{11}$ has a non-centrosymmetric structure [102-104] consistent with the proposed space group. The n = 4 compound, $Pr_2Ti_2O_7$ was refined as a second phase (18.7(9)% by weight). No evidence was seen of a secondary Ta containing phase and refinement of the Ti/Ta site occupancy ratios in the main phase revealed it to be Ta rich (Ti:Ta per formula unit = 1.65(3):1.35(3)). Based on the refined weight percentages it can be assumed that $Pr_2Ti_2O_7$ does not show significant solid solution with Ta, and that the excess Ta is mainly contained in the 3-layer phase, whose general composition can be expressed as $Pr_3Ti_{2-x}Ta_{1+x}O_{11+x/2}$ ($x \approx 0.35$). The mechanism for accommodating the non-stoichiometry is not known at this stage.

Fig. 4.2.1(b) shows a model for the crystal structure of $Pr_3Ti_2TaO_{11}$ along the *b-a* and *b-c* projections, which was produced based on the refined cation sublattice and the structure of $La_3Ti_2TaO_{11}$. $Pr_3Ti_2TaO_{11}$ is proposed to have an n = 3(II) heteroblock structure. The refinement of the cation sublattice site occupancies suggests that the 2-layer and 4-layer sections are not simply formed of $PrTaO_4$ and $Pr_2Ti_2O_7$, respectively. Ta^{5+} and Ti^{4+} are randomly distributed in the BO_6 octahedra. Due to the inability to refine details of the anion sublattice, the structure must be considered to be tentative.

Table 4.2.1 Crystal data and refinement parameters for $Pr_3Ti_2TaO_{11}$ powder.

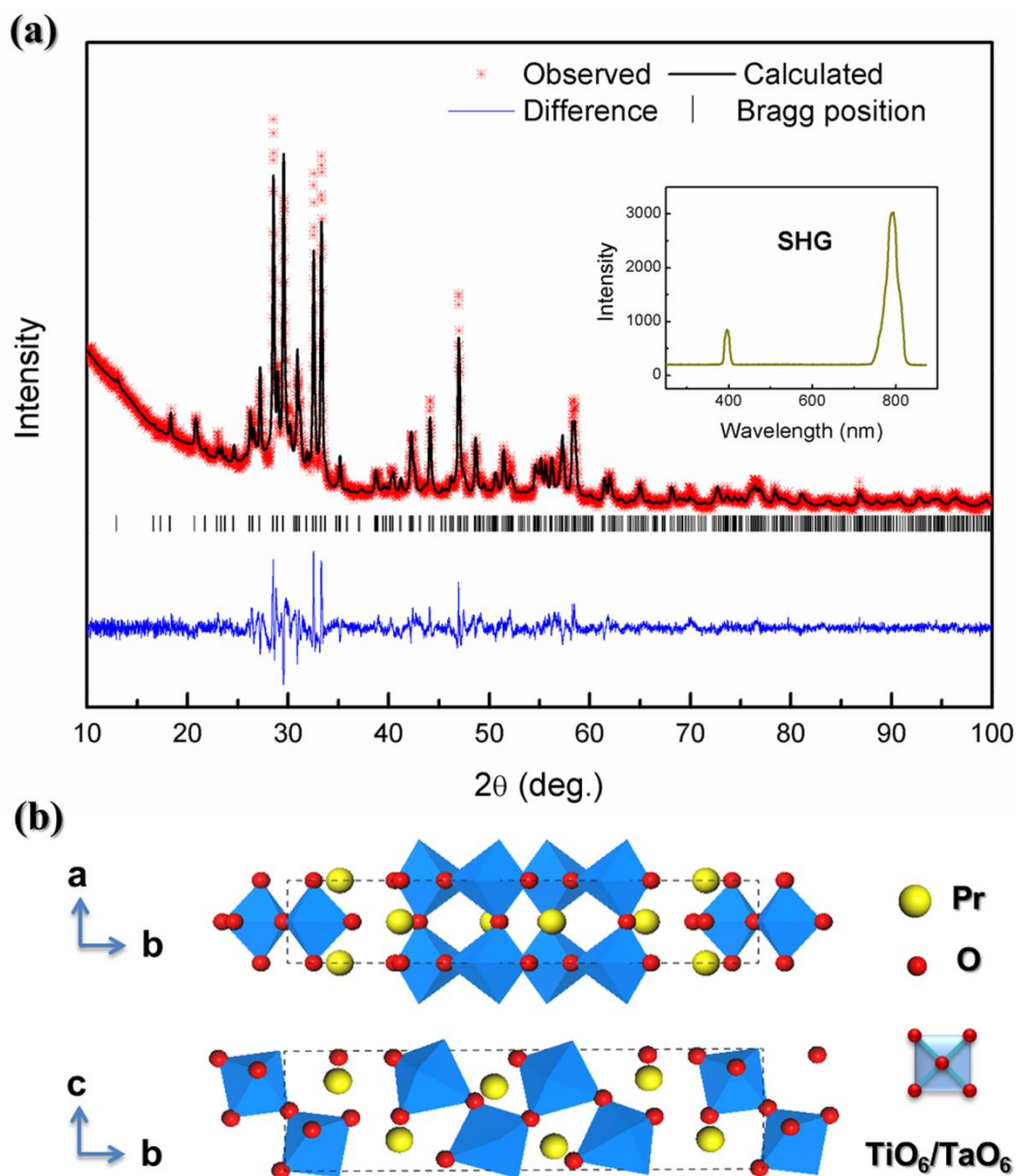| Compound	$Pr_3Ti_2TaO_{11}$
Crystal system	Orthorhombic
Space group	$Pmc2_1$ (26)
a (Å)	3.8689(3)
b (Å)	20.389(2)
c (Å)	5.5046(5)
V (Å^3)	434.2(1)
Z	2
Density (g/cm^3)	6.698
Reduced χ^2	2.585
No. of variables	72
No. of profile points	6879
R_{wp} (%)	8.09
R_p (%)	6.03
R_{ex} (%)	5.06
R_F2	15.32
No. of reflections	2830

Fig. 4.2.1 (a) Rietveld refinement for $Pr_3Ti_2TaO_{11}$ powder prepared by co-precipitation. The inset shows the SHG result. (b) Crystal structure of $Pr_3Ti_2TaO_{11}$ with *b-a* and *b-c* projections.

Fig. 4.2.2 shows the XRD patterns of $Pr_3Ti_2TaO_{11}$ powders and ceramics prepared by CP and SSR. A small trace of $Pr_2Ti_2O_7$ and an unknown phase were detected in the powders and ceramics prepared by SSR, which can be attributed to inhomogeneity of the starting materials. Compared with the powders, the diffraction peaks for the spark

plasma sintered ceramics prepared using the CP and SSR powders were broader. This peak broadening was produced by a disordering of the structure produced by the relatively rapid heating/cooling during SPS processing. Fig. 4.2.3 shows XRD patterns of textured $Pr_3Ti_2TaO_{11}$ ceramics from both the surfaces perpendicular and parallel to the SPS pressing direction. The diffraction patterns from the surface parallel to the SPS pressing direction exhibit strong $(0\ k\ 0)$ reflections. On the other hand, the patterns from the surface perpendicular to the SPS pressing direction show very weak $(0\ k\ 0)$ reflections. This indicates that the two-step SPS processed ceramics were highly textured. The Lotgering orientation factor, f, is estimated to be 0.52 for the ceramic prepared by SSR and 0.63 for the ceramic prepared by CP.
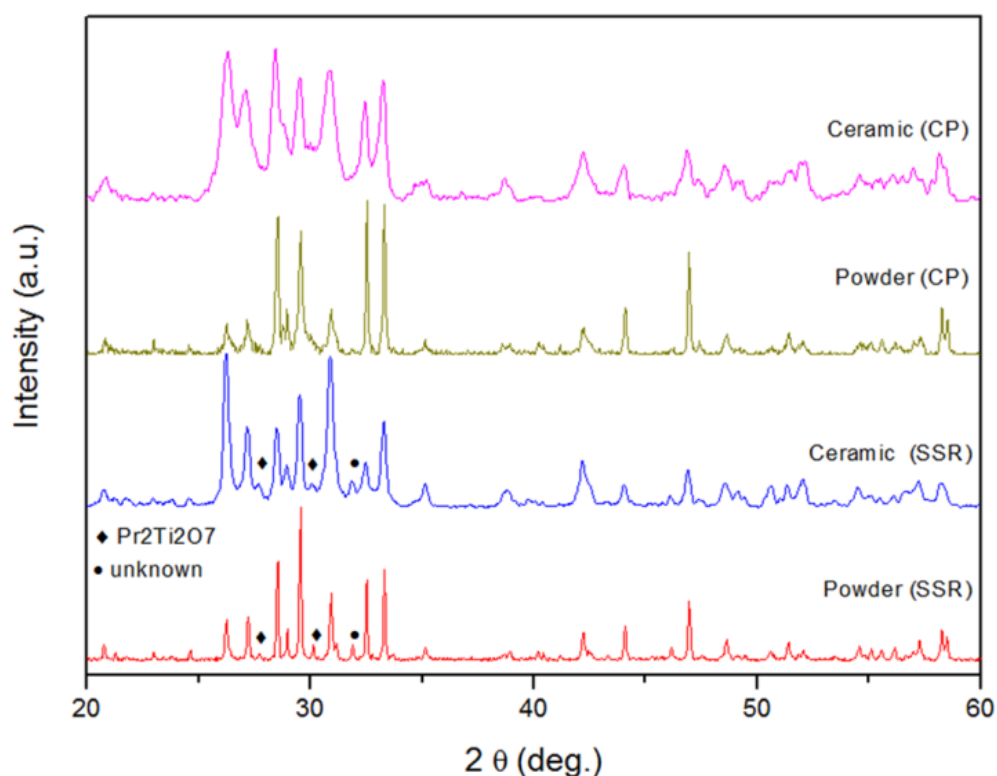

Fig. 4.2.2 X-ray diffraction patterns of $Pr_3Ti_2TaO_{11}$ powders and ceramics prepared by CP and SSR.
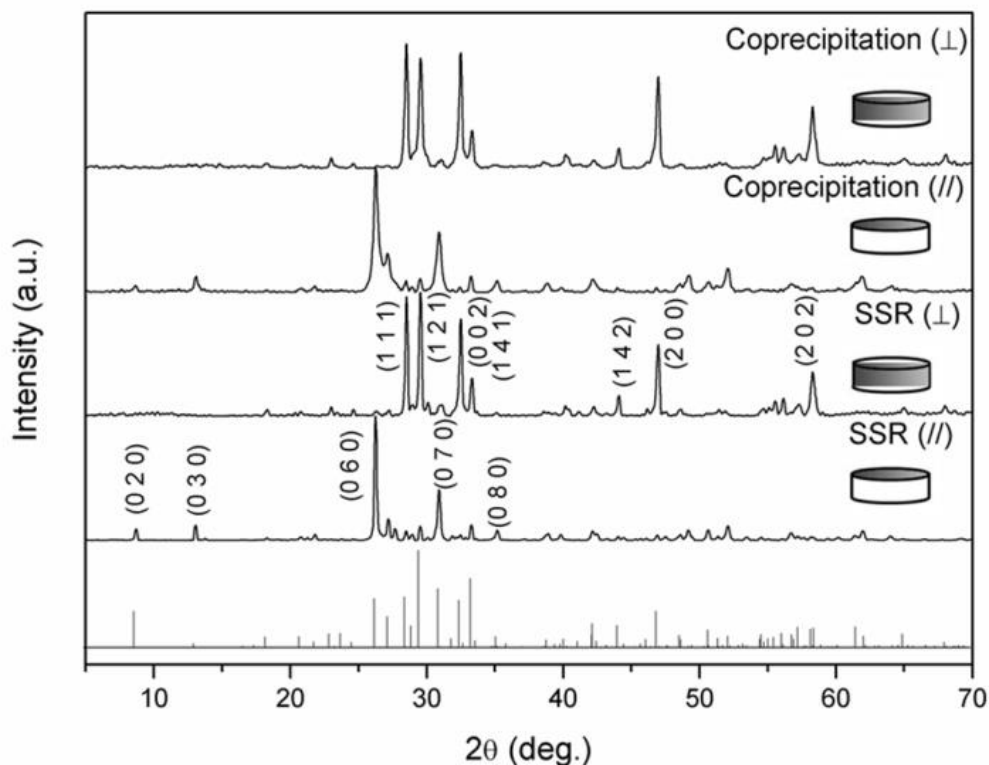
Fig. 4.2.3 X-ray diffraction patterns of textured $Pr_3Ti_2TaO_{11}$ ceramics.

Fig. 4.2.4 shows X-ray photoelectron spectra of the main elements in $Pr_3Ti_2TaO_{11}$ powders prepared by SSR and CP methods. The Pr $3d$ doublets are produced by spin-orbit coupling (Fig. 4.2.4(a)).[105, 106] This multiplet splitting is similar to those found for the 4-layer PLS compound $Pr_2Ti_2O_7$.[107] Both of the Pr $3d_{5/2}$ and Pr $3d_{3/2}$ peaks can be regarded as a combination of two peaks with different intensities, which suggests Pr^{3+} has two distinctly different chemical environments in the samples. This result agrees well with the features of materials with PLS structure. For instance, in the 4- layer compounds $A_2B_2O_7$, the A-site elements can occupy positions at the layer boundary or inside the layers. Fig. 4.2.4(b) shows the Ti $2p$ doublets, which can be attributed to the Ti-O bond in a TiO_6 octahedral-like environment. Unlike the narrow symmetrical Ti $2p$ peaks observed for the 4-layer compounds $La_2Ti_2O_7$ and $Pr_2Ti_2O_7$,[106, 107] a distinct high binding energy (BE) shoulder is observed for Ti $2p_{3/2}$. This could be attributed to the

nature of the 3-layer type II structure of $Pr_3Ti_2TaO_{11}$, which can be considered as an alternating layer structure consisting of perovskite layers with $n = 2$ and perovskite layers with $n = 4$ stacked in an ordered manner. As discussed before, the B site ions Ti^{4+} and Ta^{5+} in the crystal structure are randomly distributed, it is reasonable to think that the Ti^{4+} ions in the 2-layer and 4-layer sections possess different chemical environments. The binding energy of Ta $4f_{5/2}$ (27.2 eV) and Ta $4f_{7/2}$ (25.3 eV) are related to the higher oxidation state of Ta^{5+}.[108, 109] The spectrum of O 1s core level is shown in Fig. 4.2.4(d). The O 1s peaks can be divided into three elementary peaks with the middle peak dominant at around 531 eV. The low intensity peak with higher binding energy is probably produced by adsorbed OH groups. The other two peaks with lower binding energy are related to different oxygen states in the layer crystal structure.[32, 33] There were no significant differences in XPS spectra of samples prepared by SSR and by co-precipitation (Fig. 4.2.4). The similarity in local structure between the $n = 4$ secondary phase $Pr_2Ti_2O_7$ and the $n = 4$ blocks of $Pr_3Ti_2TaO_{11}$ mean that the contribution of the second phase to the XPS spectra cannot be determined.

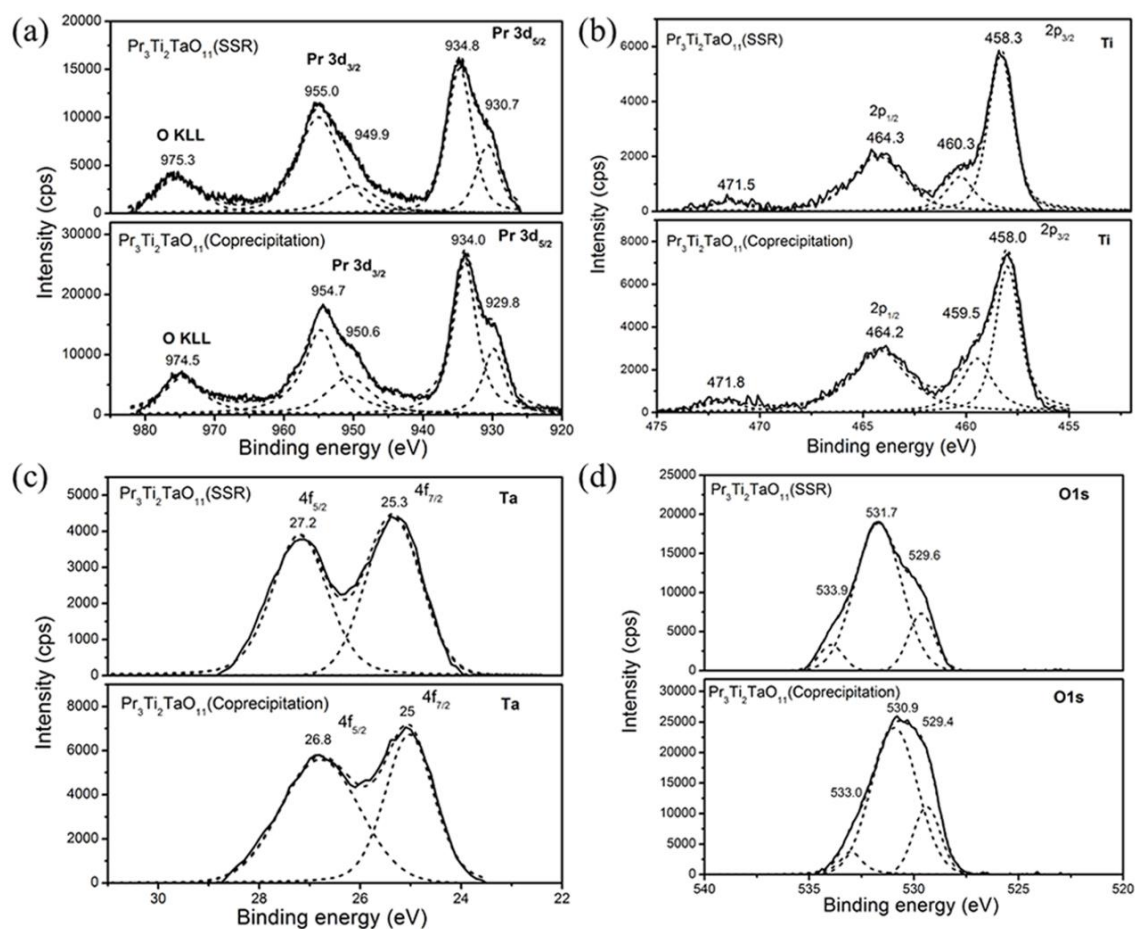Fig. 4.2.4 X-ray photoelectron spectra showing (a) Pr $3d_{5/2}$ and $3d_{3/2}$, (b) Ti $2p_{3/2}$ and $2p_{1/2}$, (c) Ta $4f_{7/2}$ and $4f_{5/2}$ and (d) O $1s$ emissions.

Fig. 4.2.5 shows SEM images of $Pr_3Ti_2TaO_{11}$ powders and ceramics prepared by co-precipitation. As shown in Fig. 4.2.5(a), nano-sized amorphous powders can be obtained using the co-precipitation technique. After calcination the powders are still smaller than 1 μm (Fig. 4.2.5(b)). Fig. 4.2.5(c) shows the fractured surface of the untextured ceramics after SPS. It shows that dense ceramics with small grains were obtained after SPS. Fig. 4.2.5(d) shows the fractured surface perpendicular to the SPS pressing direction of the textured ceramics after two-step SPS processing. The grains are plate-like, as seen in 4-layer PLS ceramics,[7, 12] which is caused by their layered crystal structure. It also can be observed that the plate-like grains are highly orientated along

the direction perpendicular to the SPS pressing direction, which is consistent with the XRD results shown in Fig. 4.2.3. The relative density of all of the ceramics is greater than 98%.

Fig. 4.2.6(a) shows a typical bright field TEM image of untextured $Pr_3Ti_2TaO_{11}$ ceramics with a high density of planar defects. Fig. 4.2.6(b) shows a phase contrast image of a typical grain with the (0 1 0) lattice planes imaged. The corresponding electron diffraction pattern shows streaking of the (0 k 0) reflections. Fig. 4.2.6(c) shows a similar area at higher resolution with a region of 4-layer (1.3 nm) PLS phase that is about 20 unit cells wide. The microstructure consists of 3-layer (2 nm) PLS phase with intergrowths of 4-layer perovskite phase.[110, 111] There is also associated faulting in the lattice structure where the 4-layer perovskite intergrowths terminate or move to a different plane. Some regions of indeterminate stacking are also evident (eg, marked X). Fig. 4.2.6(d) shows a line scan across a region of mixed phases, which reveals the intimate and disordered mixing of the $n = 3$ and 4 layer structures. The highly disordered microstructure explains the broadening of the XRD peaks of the ceramics (Fig. 4.2.2) and is consistent with the appearance of the $n = 4$ structure as a secondary phase in the XRD data. Fig. 4.2.6(e) shows a region of $n = 3$ phase at high resolution and Fig. 4.2.6(f) shows a line scan across this region, which reveals an asymmetry in the unit cell structure that is consistent with the periodicity of the 4-2 alternating layer structure of an $n = 3$ type II compound.
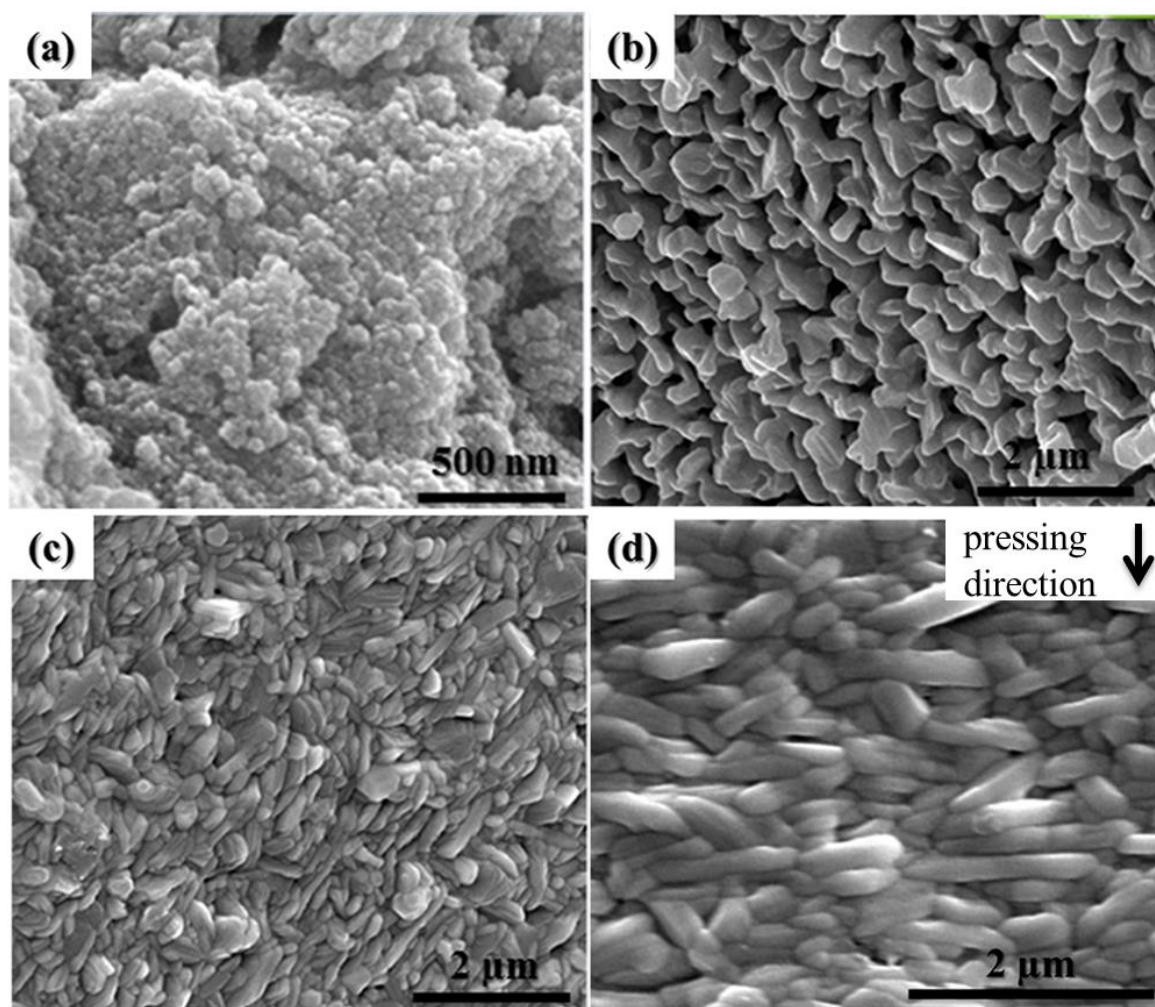
Fig. 4.2.5 SEM micrographs of $Pr_3Ti_2TaO_{11}$ powders and ceramics prepared by co-precipitation: (a) precipitate powders; (b) calcined powders; (c) the fractured surface of the untextured ceramic; and (d) the fractured surface with the normal line perpendicular to the SPS pressing direction of the textured ceramics.
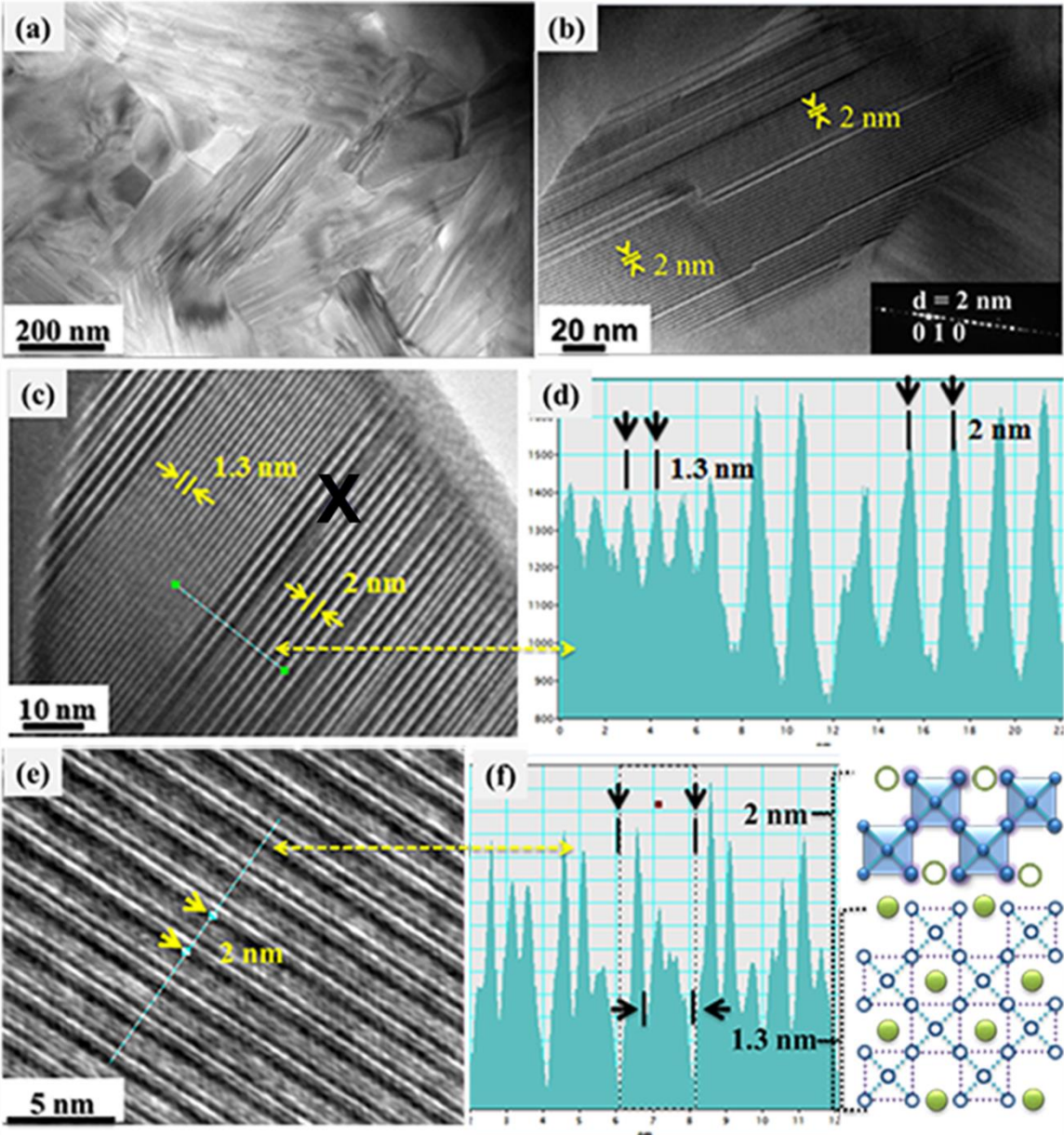
Fig. 4.2.6 TEM micrographs of untextured $Pr_3Ti_2TaO_{11}$ ceramics: (a) a typical bright field TEM image; (b) a phase contrast image of a typical grain with the (0 1 0) lattice planes imaged; (c) a similar area with (b) at higher resolution; (e) a region of $n = 3$ phase at high resolution; (d, f) the profile of the line scanned areas.

Fig. 4.2.7 shows the frequency dependence of permittivity and loss of textured and untextured $Pr_3Ti_2TaO_{11}$ ceramics prepared by SSR and co-precipitation measured at room temperature. The permittivity and loss of all the samples is stable in the frequency range from 10^3 to 10^7 Hz. Both the textured ceramics prepared by SSR and co-

precipitation show a higher permittivity than the untextured ceramics, which is attributed to the anisotropy of the layer structure.[112] Additionally, the samples prepared by co-precipitation have higher permittivity than the samples prepared by SSR. The untextured ceramics prepared by co-precipitation and the textured ceramics prepared by SSR show an increasing loss in the low frequency range below 10^4 Hz. As their permittivity in the same range of frequency is relatively stable, the increase of loss is probably caused by leakage conductance.
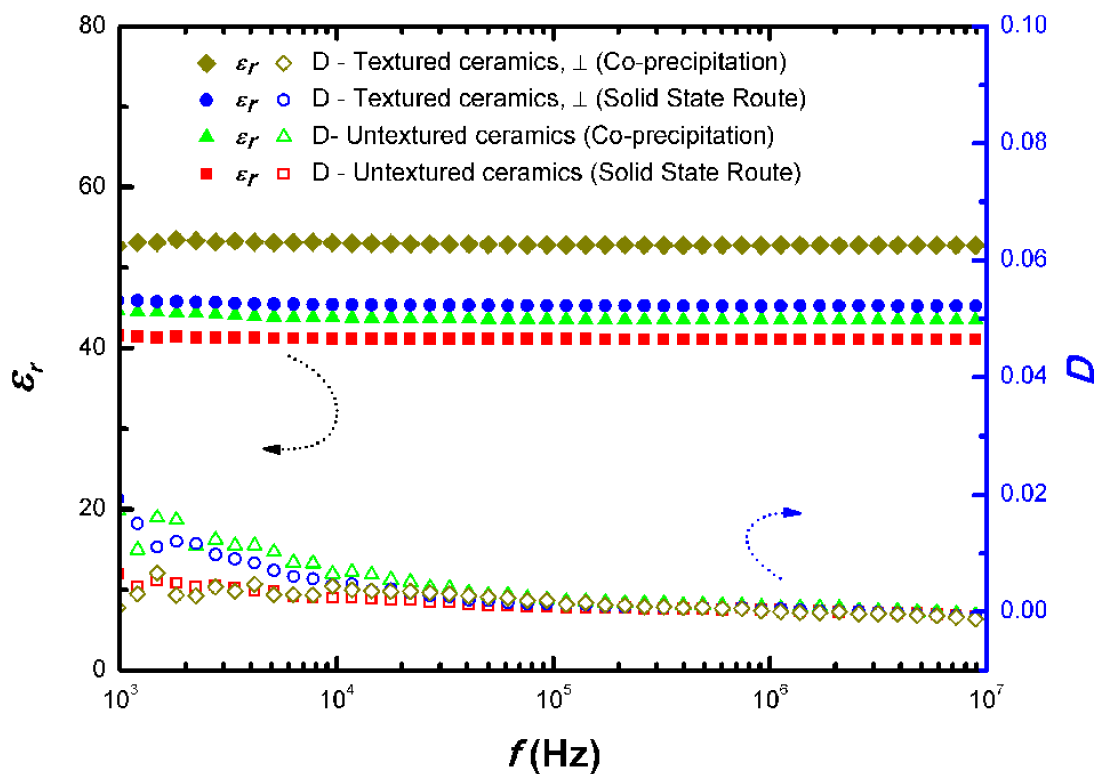

Fig. 4.2.7. Frequency dependence of permittivity and loss at room temperature.

Fig. 4.2.8 shows the temperature dependence of permittivity and loss of the untextured $Pr_3Ti_2TaO_{11}$ ceramics. The Curie point of the $Pr_3Ti_2TaO_{11}$ ceramic is 1415 ± 5 °C. The loss peaks just below T_c are attributed to ferroelectric domain wall movement.[95, 96]

There is no dispersion in the temperature of the dielectric anomaly at different frequencies. The inset in Fig. 4.2.8 shows the *I-E* and *P-E* hysteresis loops of a textured ceramic at room temperature. No obvious ferroelectric domain switching peak is found in the *I-E* hysteresis loops despite the application of a high field (> 300 kV/cm). Textured ceramics prepared by SSR and CP were poled in silicone oil at 200 °C under various DC electric fields up to 300 kV/cm. A zero piezoelectric constant d_{33} was measured, which means the samples could not be ferroelectrically switched. The high resolution images (Fig. 4.2.6) reveal that $Pr_3Ti_2TaO_{11}$ has a highly disordered layer structure on an atomic level. Although it is polar, these microstructures would be extremely difficult to ferroelectrically switch because of this disorder. High temperature poling was used to demonstrate ferroelectricity. Textured ceramics were heated above 900 °C in a tube furnace. An electric field between about 200 V/cm was applied to pole the samples. For all the samples, a small but stable d_{33} value between 0.1 and 0.2 pC/N was detected at room temperature.
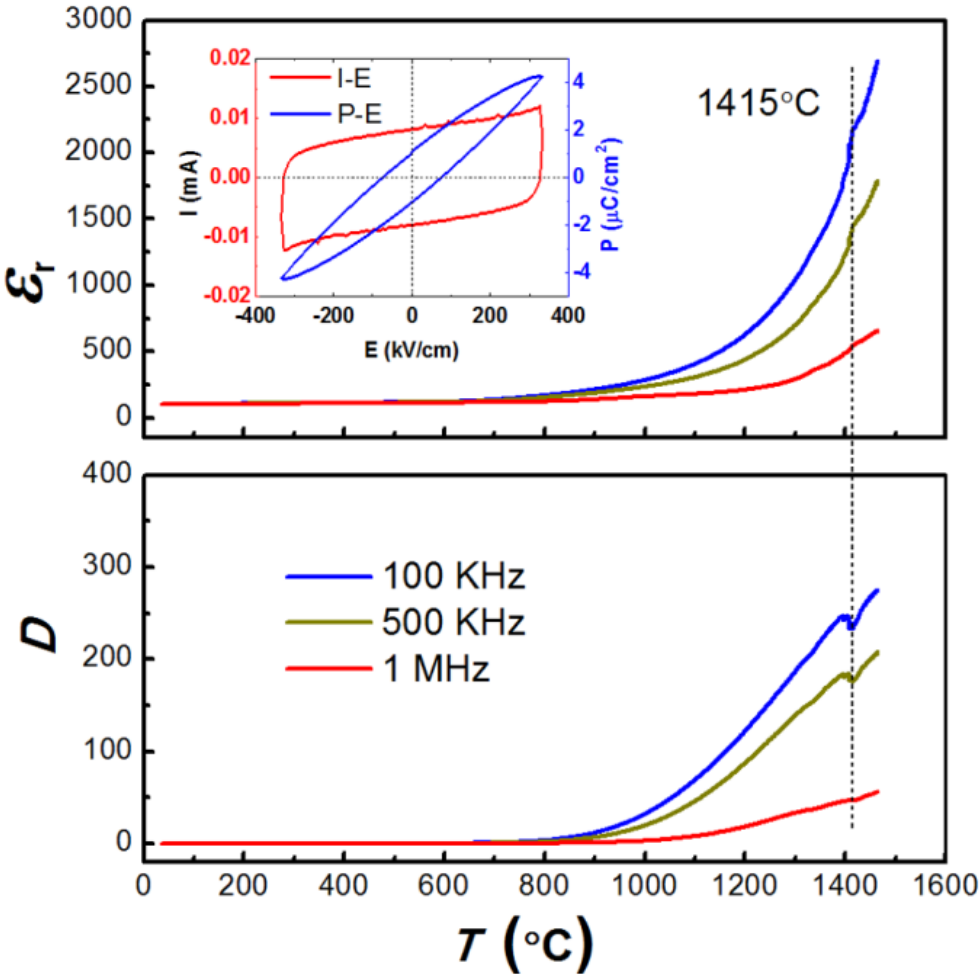
Fig. 4.2.8. Temperature dependence of permittivity and loss. The inset shows *P-E* and *I-E*

hysteresis loops of textured ceramics at room temperature.

4.2.4 Conclusions

In conclusion, $Pr_3Ti_2TaO_{11}$ powders were prepared by CP synthesis and SSR. Textured $Pr_3Ti_2TaO_{11}$ ceramics were prepared using a two-step SPS method. In the first step, the powders prepared by SSR and CP were sintered in a 20 mm diameter graphite die for 3 min under a pressure of 80 MPa at 1350 and 1250 °C, respectively. In the second step, the sintered ceramics were placed in a 30 mm diameter graphite die and sintered for 5 min under a pressure of 80 MPa at 1450 and 1400 °C for the SSR and CP prepared samples, respectively. Finally, the sintered ceramics were annealed in air at 1200 °C for 15 h to remove any carbon contamination and reduction produced by SPS. The $Pr_3Ti_2TaO_{11}$ compound has a 3-layer type II perovskite-like layered structure with space group *Pmc2*$_1$. High resolution TEM images show that the ceramics were highly disordered with faulting in the layer structure of the $n = 3$ type II phase and coexistence of a $n = 4$ phase intergrowths on a fine scale (nm). A super-high Curie point (1415 ± 5 °C) was indicated by the temperature dependence of the permittivity and loss peaks. The disordered structure made it difficult to ferroelectrically switch and pole the samples. However, by using an electric field of 100 to 200 V/cm at 900 °C it was possible to demonstrate a small piezoelectric activity with d_{33} between 0.1 to 0.2 pC/N.

4.3 2-layer LaTaO$_4$ Compound

4.3.1 Introduction

There is no report in the literature on the ferroelectricity of the 2-layer LaTaO$_4$ compound. However the structure of LaTaO$_4$ has been studied. It is a *A2$_1$am* orthorhombic modification of LaTaO$_4$, which is non-centrosymmetric and has the potential to present ferroelectricity. Cava *et al*. reported that the orthorhombic modification of LaTaO$_4$ is stable above 175 °C.[31] Titov *et al*. reported that the orthorhombic modification is stable in the temperature range from 20 to 1197 °C, and coexists with a monoclinic modification below 150 °C.[32] It is difficult to synthesize phase-pure LaTaO$_4$ because it is very sensitive to annealing temperature and pressure. Consequently, the monoclinic LaTaO$_4$ and the orthorhombic LaTaO$_4$ phases coexist at room temperature.

The aim of this work was to obtain phase-pure orthorhombic LaTaO$_4$ at room temperature, and then to study its dielectric, ferroelectric, and piezoelectric properties.

4.3.2 Experimental Procedure

SSR and CP methods were used to prepare phase-pure $LaTaO_4$ powders. La_2O_3 (99.99%) and TiO_2 (99.9%) were used as starting materials for SSR. Stoichiometric mixtures of the oxides were ball milled with ethanol at 350 rpm for 3 h. Powder calcination temperature were chosen from 1100 to 1500 °C. A two-step calcination process was also used to improve the phase purity. For co-precipitation, $La(NO_3)_3 \cdot 6H_2O$ (99.9%) and $Ti(OCH_9)_4$ (97%) were used as the starting precursors, and an ammonia water solution was used as the precipitator. The particular procedure is similar to that of $Pr_3Ti_2TaO_{11}$ as described in section 4.2.2. The dried precipitate was calcined at 1300 °C for 4 h. The calcined powders were sintered using SPS. A heating rate and cooling rate of 100 °C /min was used in all cases. The sintering temperatures were chosen from 1100 to 1500 °C. The $LaTaO_4$ powders prepared by SSR and CP were sintered in a 20 mm diameter graphite die for 3 min at high temperature under a pressure of 80 MPa in the SPS furnace.

4.3.3 Results and Discussion

To obtain the phase-pure orthorhombic $LaTaO_4$ powder using the SSR method, the stoichiometric-mixed raw materials were calcined at different temperatures. The XRD patterns of the calcined powders are shown in Fig. 4.3.1. According to Titov's report,[32] the orthorhombic modification of $LaTaO_4$ is stable in the temperature range from 20 to 1197 ℃, therefore at first the calcination temperatures were chosen below 1200 ℃. Fig. 4.3.1 (a) shows the XRD patterns of $LaTaO_4$ powders calcined at 1200 ℃ for 4 hours, 1150 ℃ for 12 hours and 24 hours. All of the powders have an orthorhombic main phase ($A2_1am$) with several impurities. Some impurity diffraction peaks were indexed to be La_3TaO_7 and raw material Ta_2O_5. The main reason for the impurities is supposed to be the low calcination temperatures, and the fact that the raw materials were not completely reacted. Fig. 4.3.1(b) shows the XRD patterns of $LaTaO_4$ powders calcined at 1400 and 1500 ℃ for 4 hours. No obvious La_3TaO_7 and Ta_2O_5 peaks can be observed, but the monoclinic ($P2_1/c$) $LaTaO_4$ is now observed. The M/O ratio of the 1500 ℃ calcined powders is higher than that of the 1400 ℃ calcined powders. For SSR prepared powders, lower calcination temperatures (<1300 ℃) lead to more incomplete reactions of raw materials; higher calcination temperatures (>1300 ℃) lead to more biphase structure formed with orthorhombic structure and monoclinic structure.

For the CP method, the nano-sized amorphous precursors produced by CP were calcined below 1200 ℃. Fig. 4.3.2 shows the XRD patterns of the $LaTaO_4$ powders calcined at 1000 and 1100 ℃. Unknown diffraction peaks (marked in arrows) were detected for the powder calcined 1000 ℃. Phase-pure $LaTaO_4$ with orthorhombic structure was obtained with the powders calcined at 1100 ℃.
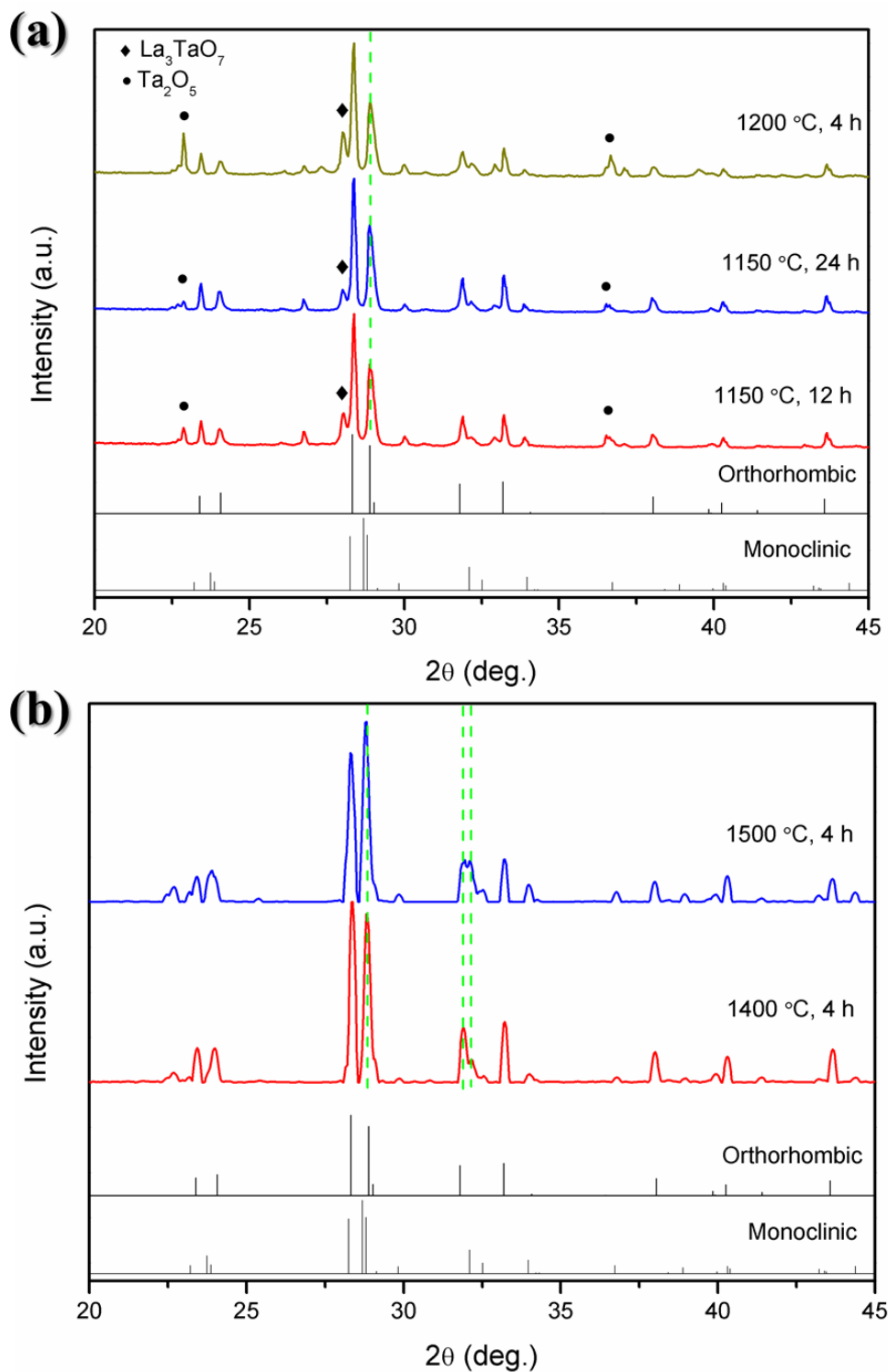
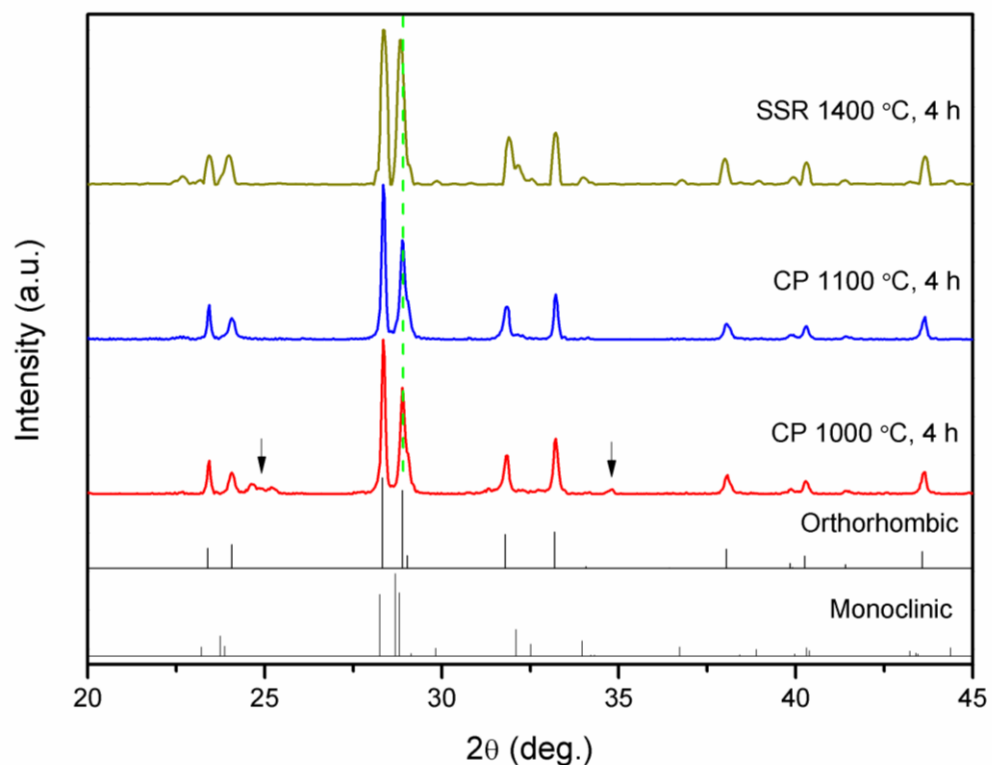Fig. 4.3.1 XRD patterns of LaTaO$_4$ powders (prepared by SSR) calcined at different

temperatures.

Fig. 4.3.2 XRD patterns of LaTaO$_4$ powders (prepared by CP) calcined at 1000 and 1100 ℃ for

4 hours.

To determine the phase purity of the LaTaO$_4$ powder calcined at 1100 ℃, its XRD

pattern was refined using the Rietveld method. Fig. 4.3.3 shows the refinement results,

and Table 4.3.1 gives the crystal data and refinement parameters. The structure

parameters of orthorhombic LaTaO$_4$ at 300 ℃ reported by Cava *et al*. was used as the

starting model for the preliminary structural analysis.[31] The observed peaks match well

with the calculated peaks, and no evidence of the monoclinic modification was detected.

The refinement of the LaTaO$_4$ powder prepared by CP and calcined at 1100 ℃ showed
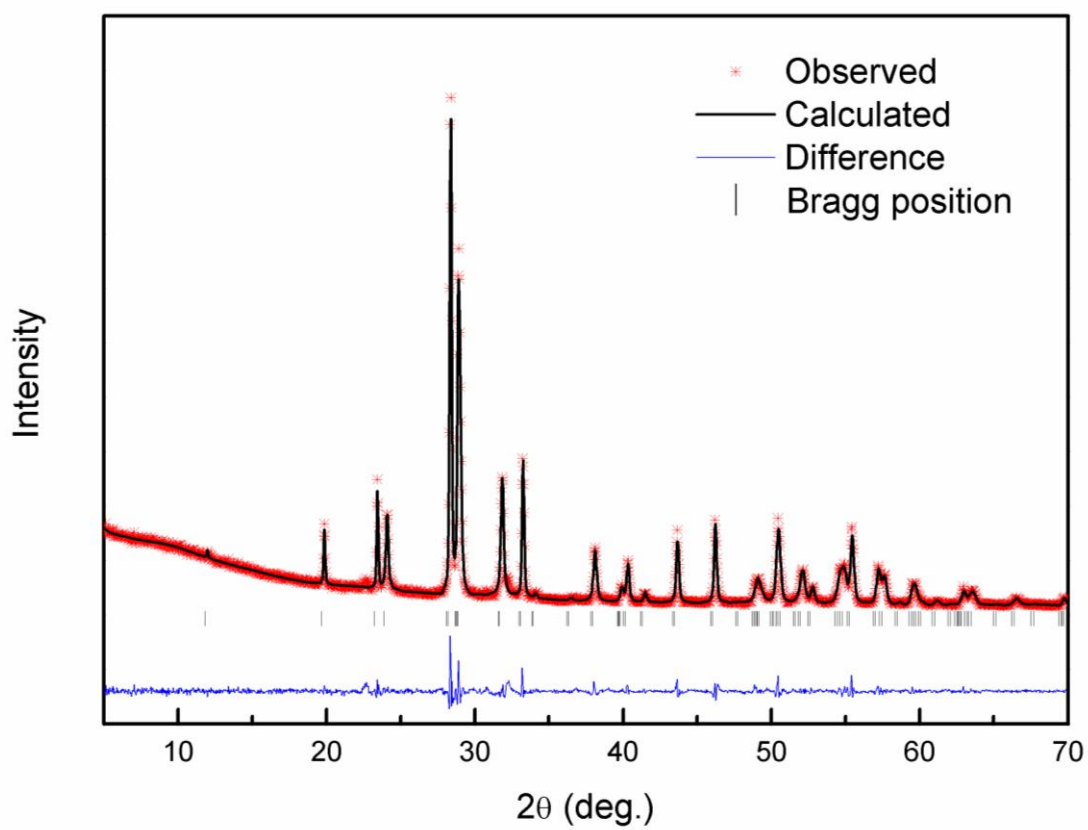
it to have an orthorhombic structure at room temperature.

Fig. 4.3.3 Rietveld refinement of LaTaO$_4$ powder prepared by CP calcined at 1100 ℃.

Table 4.3.1 Crystal data and refinement parameters of $LaTaO_4$.

Compound	$LaTaO_4$
Crystal system	Orthorhombic
Space group	*A2₁am* (36)
a (Å)	5.63034(34)
b (Å)	14.7973(9)
c (Å)	3.93605(20)
V (Å^3)	327.927(32)
Z	4
Reduced χ^2	2.564
No. of variables	50
R_{wp} (%)	6.44
R_p (%)	4.74
R_F2	9.46

Fig. 4.3.4 shows the SHG result for $LaTaO_4$ powders prepared by CP (1100 ℃ calcined) and SSR (1400 ℃ calcined). A strong SHG signal was detected in the CP powder calcined at 1100 ℃, which confirms that it has a polar structure consistent with the refinement results. The SSR powder calcined at 1400 ℃ is a biphase of polar orthorhombic phase and non-polar monoclinic phase, therefore, it has a very week SHG signal.
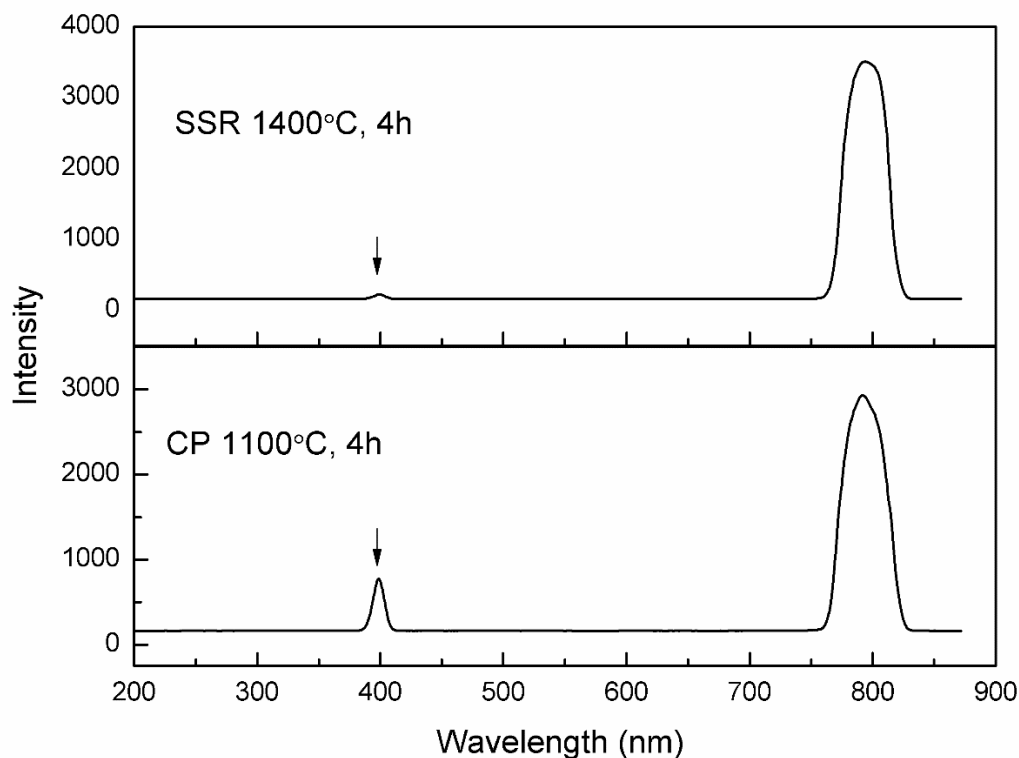
Fig. 4.3.4 SHG result of LaTaO$_4$ powders prepared by CP (1100 ℃ calcined) and SSR (1400 ℃ calcined).

Fig. 4.3.5 shows the ceramics sintered by SPS using the CP powders calcined at 1100 ℃. The ceramics were sintered at different temperatures from 1150 to 1500 ℃. The ceramics lost the phase-purity of the powders after sintering. All of the sintered ceramics are biphase, consisting of the orthorhombic and monoclinic phases. The content of monoclinic phase increases with increasing the sintering temperature, which can be clearly observed in the detailed XRD patterns shown in Fig. 4.3.5. With increasing the sintering temperature, the (1 1 1) and (1 4 0) diffraction peaks of the orthorhombic phase become broader, which is caused by the increased monoclinic diffraction peaks. According to Titov's report,[32] annealing a two phase sample (40%-45% M-LaTaO$_4$) at 1200 ℃ for long time decreased the content of the monoclinic phase to

zero. The ceramics sintered at 1350 ℃ were annealed at 1200 ℃ for 50 hours, and no obvious decrease of the monoclinic phase was observed.
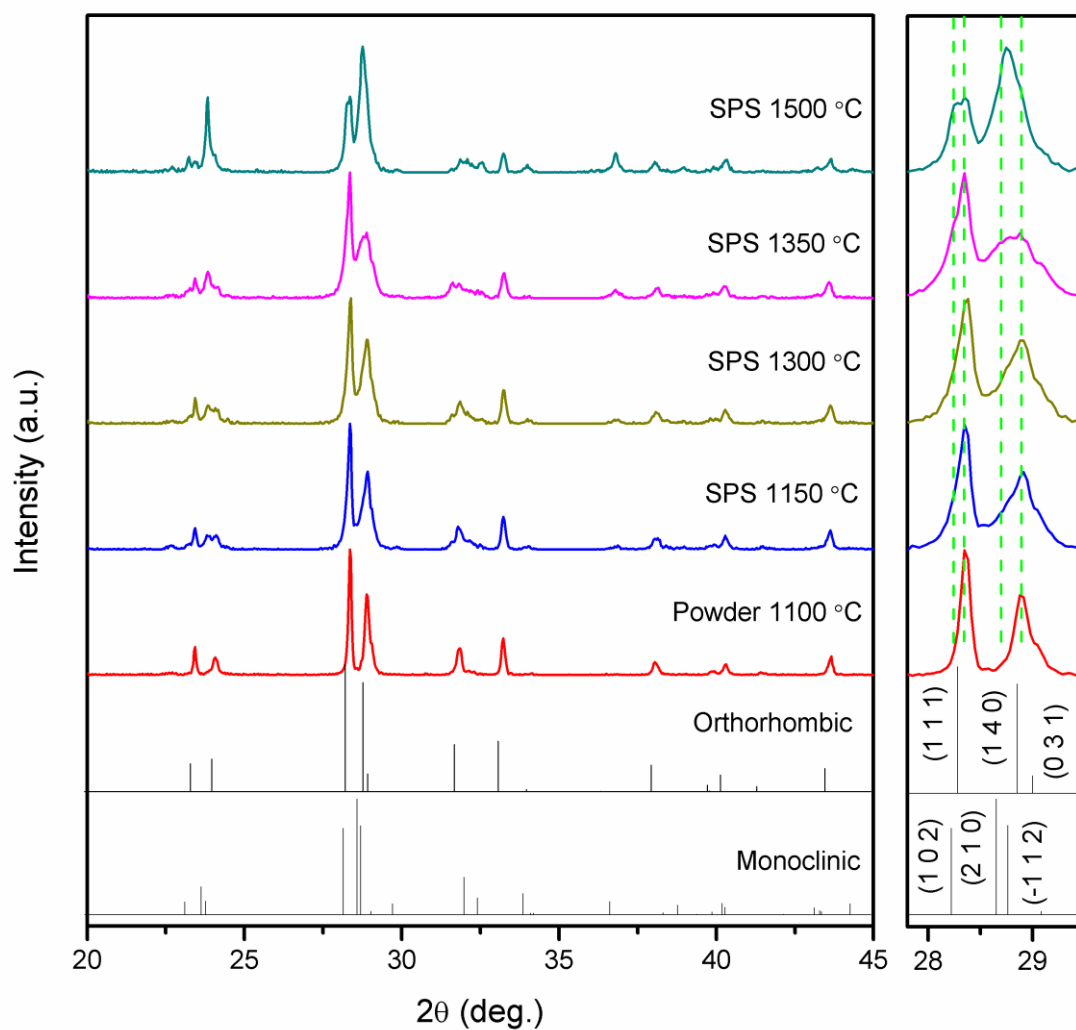

Fig. 4.3.5 XRD patterns of LaTaO$_4$ ceramics sintered by SPS at different temperature using CP powders calcined at 1100 ℃.

In an attempt to obtain ceramics with pure orthorhombic phase, CP powders were sintered at 1350 ℃ with different cooling rates (Fig. 4.3.6). The ceramic sintered at 1350 ℃ and cooled at a normal cooling rate (100 ℃/min) was biphase. The ceramic

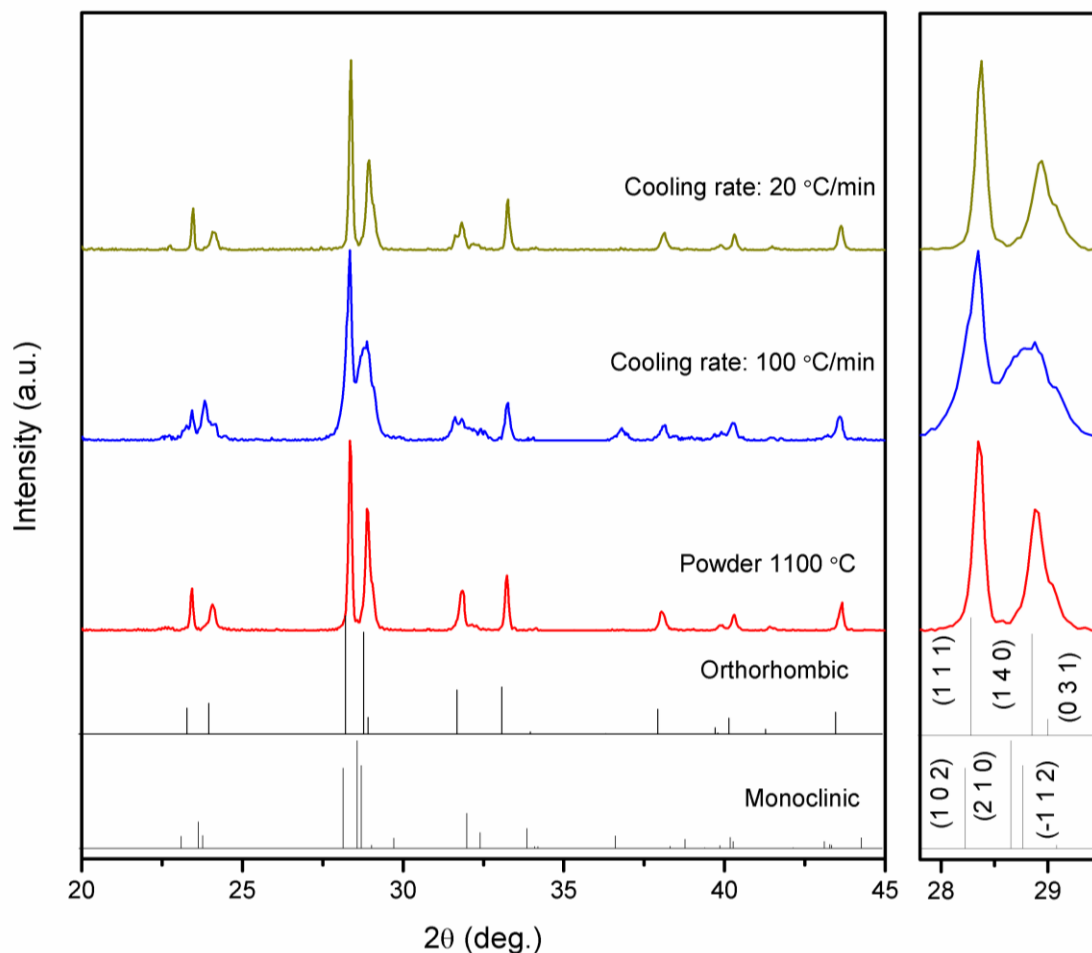sintered with lower cooling rate (20 ℃/min) maintained the pure orthorhombic phase of the powders.

Fig. 4.3.6 XRD patterns of LaTaO$_4$ ceramics sintered at 1350 ℃ with different cooling rates.

The temperature dependence of the permittivity and loss of the LaTaO$_4$ ceramic (CP, 1350 ℃, slow SPS cooling rate) with pure orthorhombic phase is shown in Fig. 4.3.7. The orthorhombic phase of LaTaO$_4$ is stable up to 1200 ℃ according to Titov's report.[32] As shown in Fig. 4.3.7, a small shoulder around 1400 ℃ is observed in the permittivity curves under different frequencies. A shoulder in the loss curves at different

frequencies is also observed just below 1400 ℃. Broad peaks (marked by arrows) are observed in both the permittivity and loss curves at about 700 ℃. To clearly study these peaks, the temperature dependence of permittivity and loss below 1000 ℃ are shown in Fig. 4.3.8.
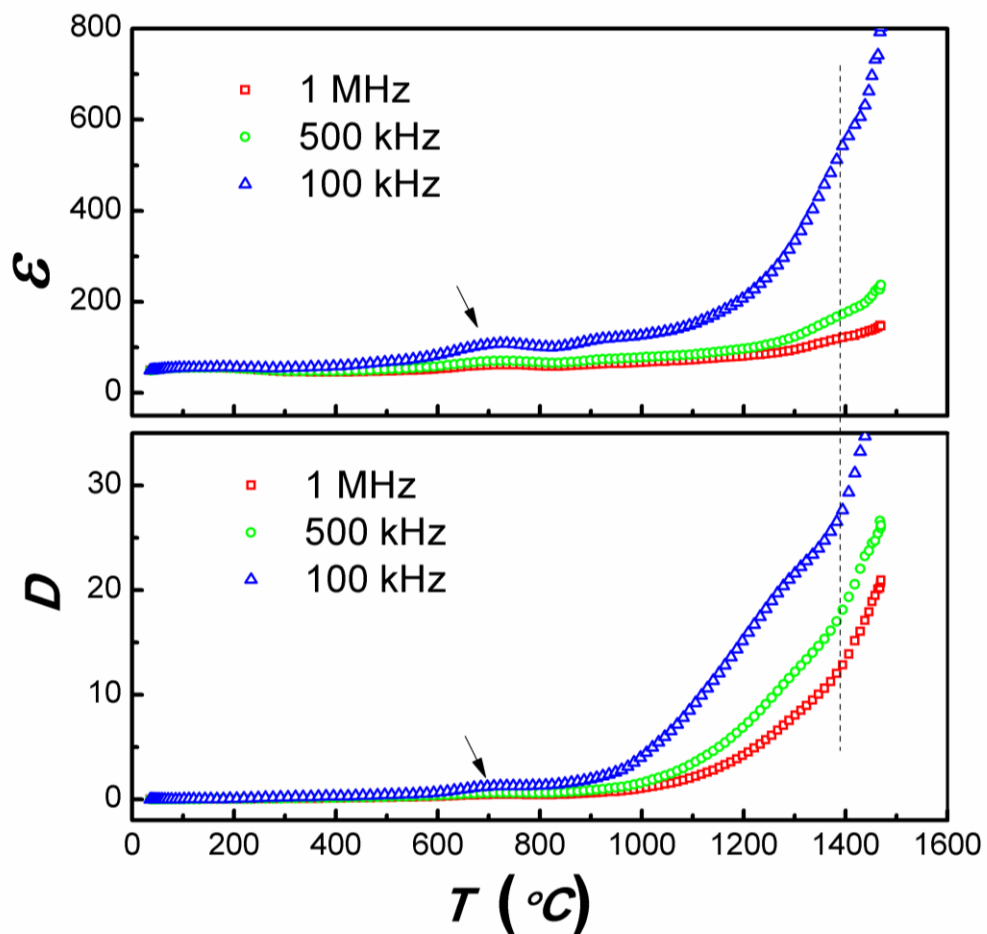

Fig. 4.3.7 Temperature dependence of permittivity and loss of the LaTaO$_4$ ceramic (CP, 1350 ℃, slow SPS cooling rate) with pure orthorhombic phase.

Fig. 4.3.8(a) shows the temperature dependence of the permittivity and loss during heating and cooling below 1000 ℃. Frequency independent permittivity and loss peaks

are observed at about 695 ℃ in the heating step, which are not observed in the cooling step. This suggests an irreversible phase transition. The same sample was remeasured under the same conditions, and the results are shown in Fig. 4.3.8(b). No permittivity and loss peaks are observed during the heating and cooling steps, which further suggest that the peaks at about 695 ℃ observed in Fig. 4.3.8(a) are produced by an irreversible phase transition. The phase structure of the LaTaO$_4$ ceramic before and after the T_c measurements was investigated using XRD (Fig. 4.3.9). Before the T_c measurement the ceramic had the pure orthorhombic phase, and became biphase after the T_c measurement.

Fig. 4.3.10 shows the current-electric field (*I-E*) and polarization-electric field (*P-E*) hysteresis loops of O-LaTaO$_4$ ceramic measured at different temperatures. No obvious ferroelectric domain switching peak is observed in the *I-E* hysteresis loops despite the application of a high field (approximately 300 kV/cm). The sample was poled in silicone oil from room temperature to 200 °C under various DC electric fields. No piezoelectric activity was detected.
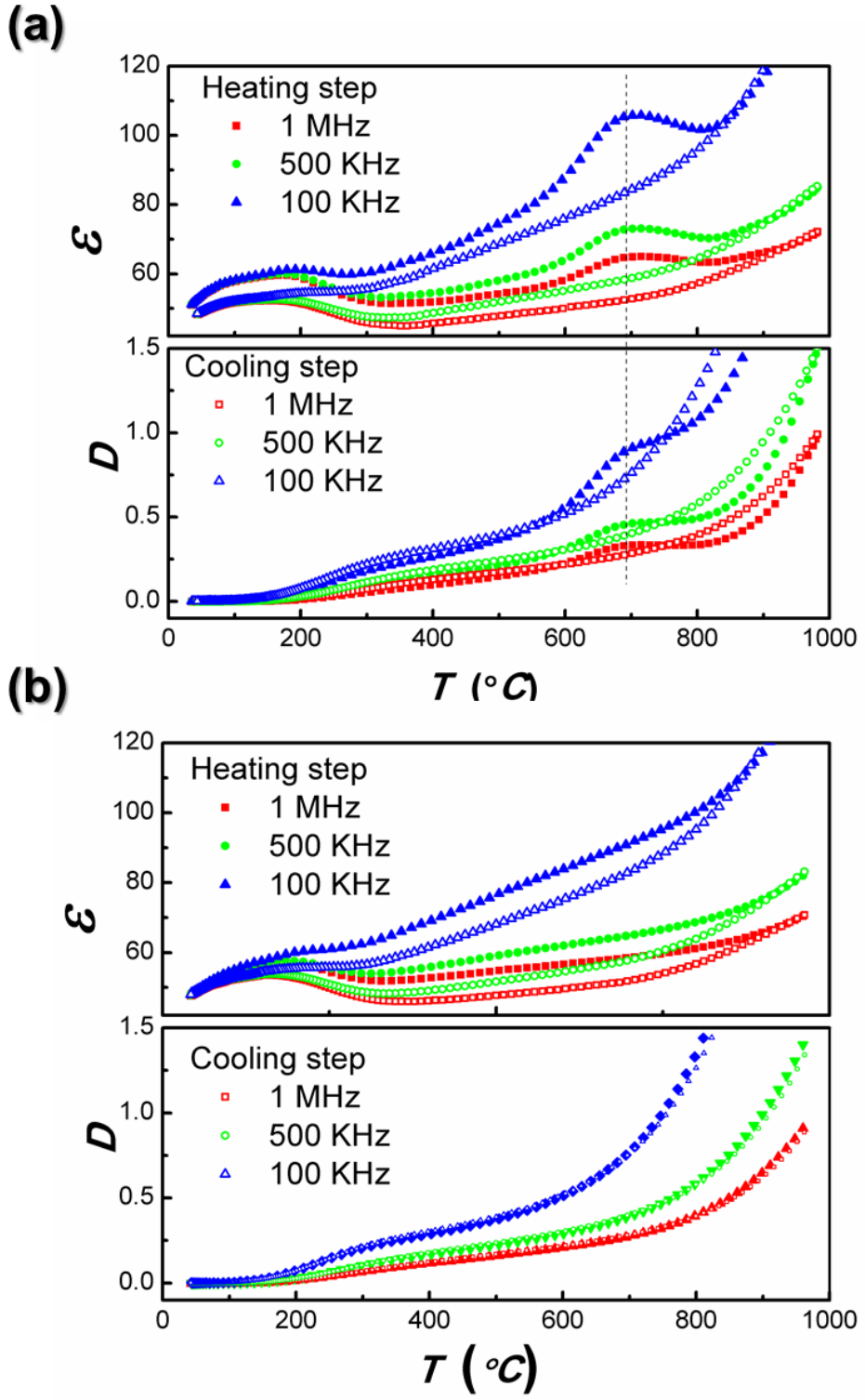
Fig. 4.3.8 Temperature dependence of permittivity and loss: (a) the LaTaO₄ ceramic below

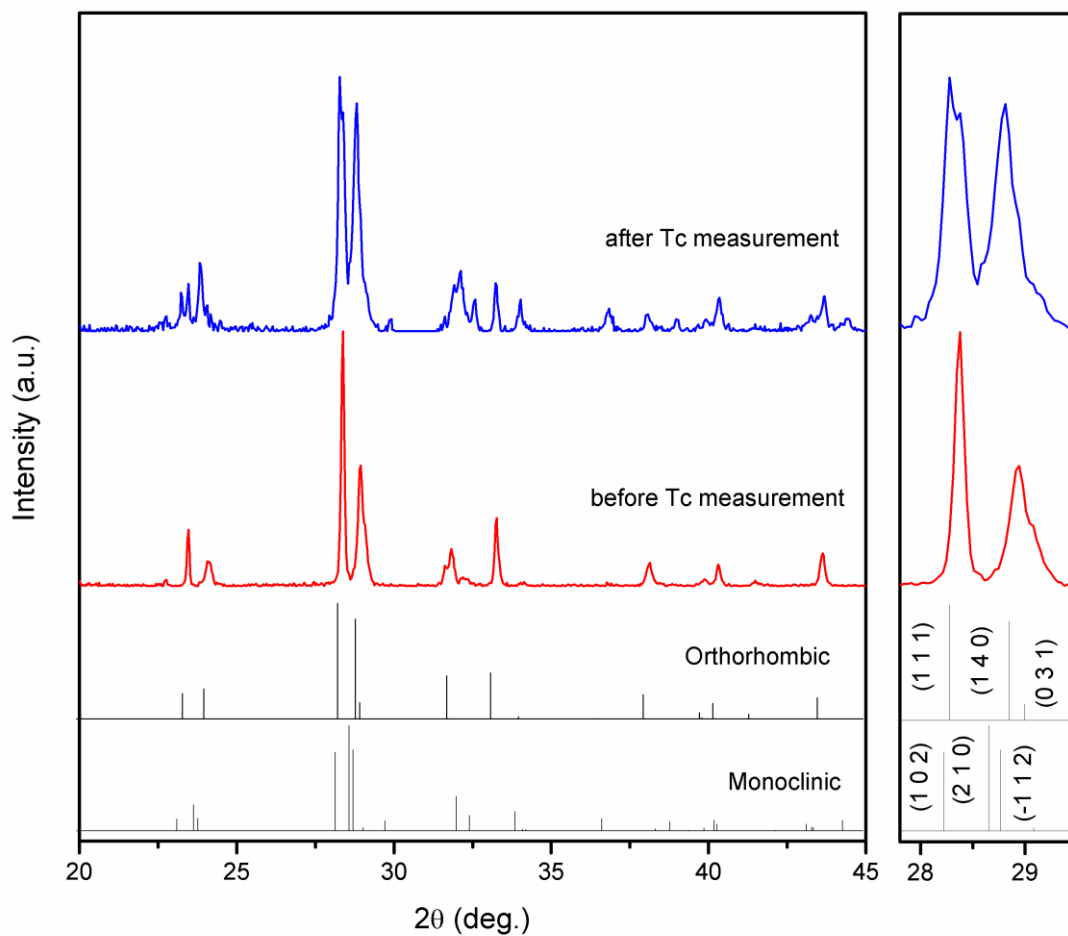1000 ℃; (b) the same sample re-measured under the same condition.

Fig. 4.3.9 XRD patterns of O-LaTaO$_4$ ceramic before and after high temperature T_c
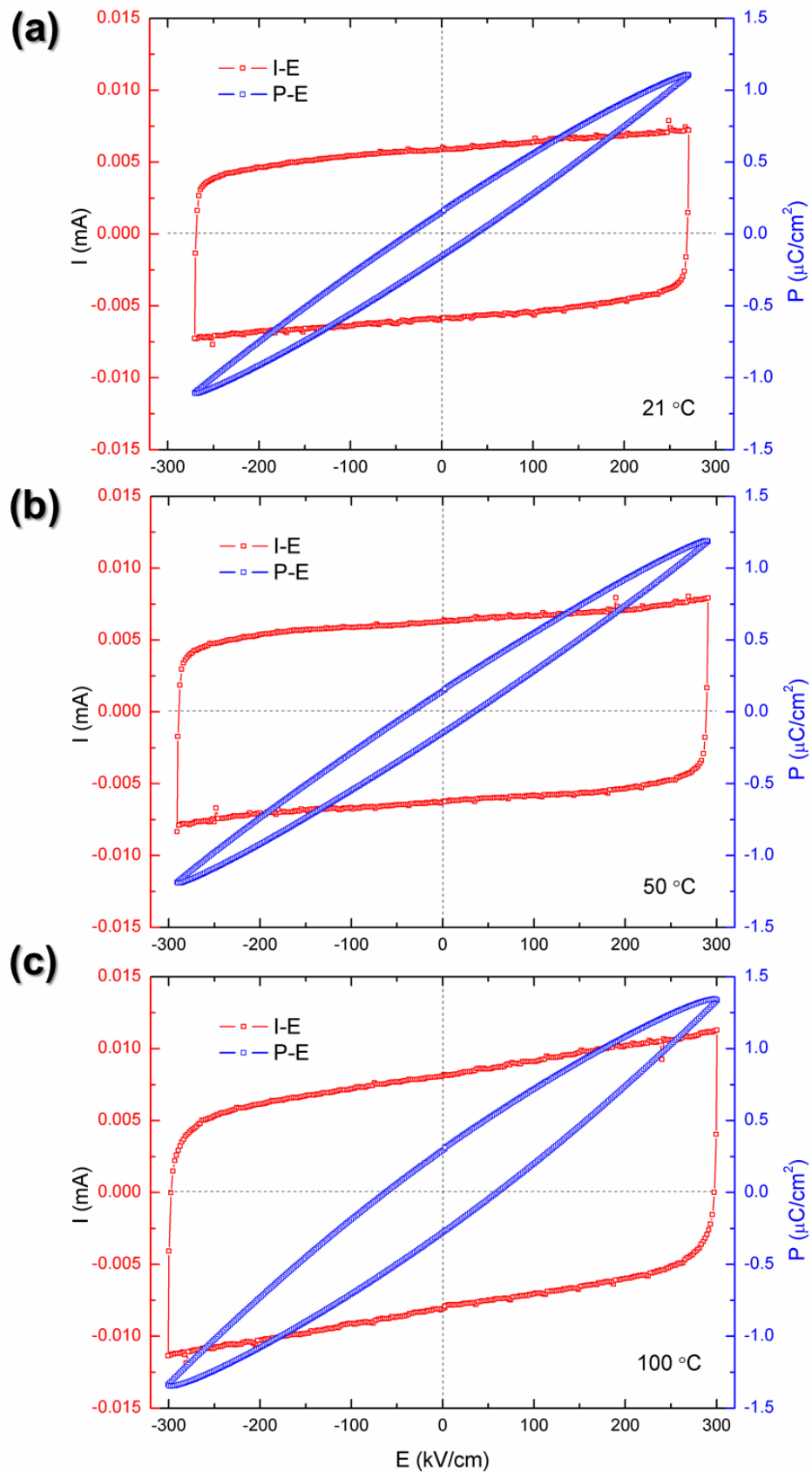
measurement.

Fig. 4.3.10 Current-electric field (*I-E*) and polarization-electric field (*P-E*) hysteresis loops of

O-LaTaO$_4$ ceramic measured at different temperature: (a) 21 ℃; (b) 50 ℃; (c) 100 ℃.

Because the monoclinic phase and orthorhombic phase of $LaTaO_4$ have similar crystal structure, and coexists at room temperature, it is supposed that the monoclinic phase might be converted into the orthorhombic phase under a high electric field. The $LaTaO_4$ ceramic sintered at 1500 ℃ with a biphase dominated by monoclinic phase (Fig. 4.3.5) was studied as M-$LaTaO_4$. The *I-E* and *P-E* hysteresis loops of M-$LaTaO_4$ ceramic were measured from room temperature to 200 ℃ under an AC field up to 230 kV/cm (Fig. 4.3.11.) No obvious peaks indicating any reversible phase transition are observed from the *I-E* loops. The M-$LaTaO_4$ ceramic was poled under a DC field (230 kV/cm) at 200 ℃, and a d_{33} of 0.3 pC/N was obtained. Fig. 4.3.12 shows the XRD patterns of the M-$LaTaO_4$ ceramic before and after poling. The monoclinic phase transferred into the orthorhombic phase after poling, which indicates that there was an irreversible electric field induced phase transition. No piezoelectric activity was detected from the O-$LaTaO_4$, but d_{33} was obtained from the orthorhombic phase induced from the M-$LaTaO_4$.
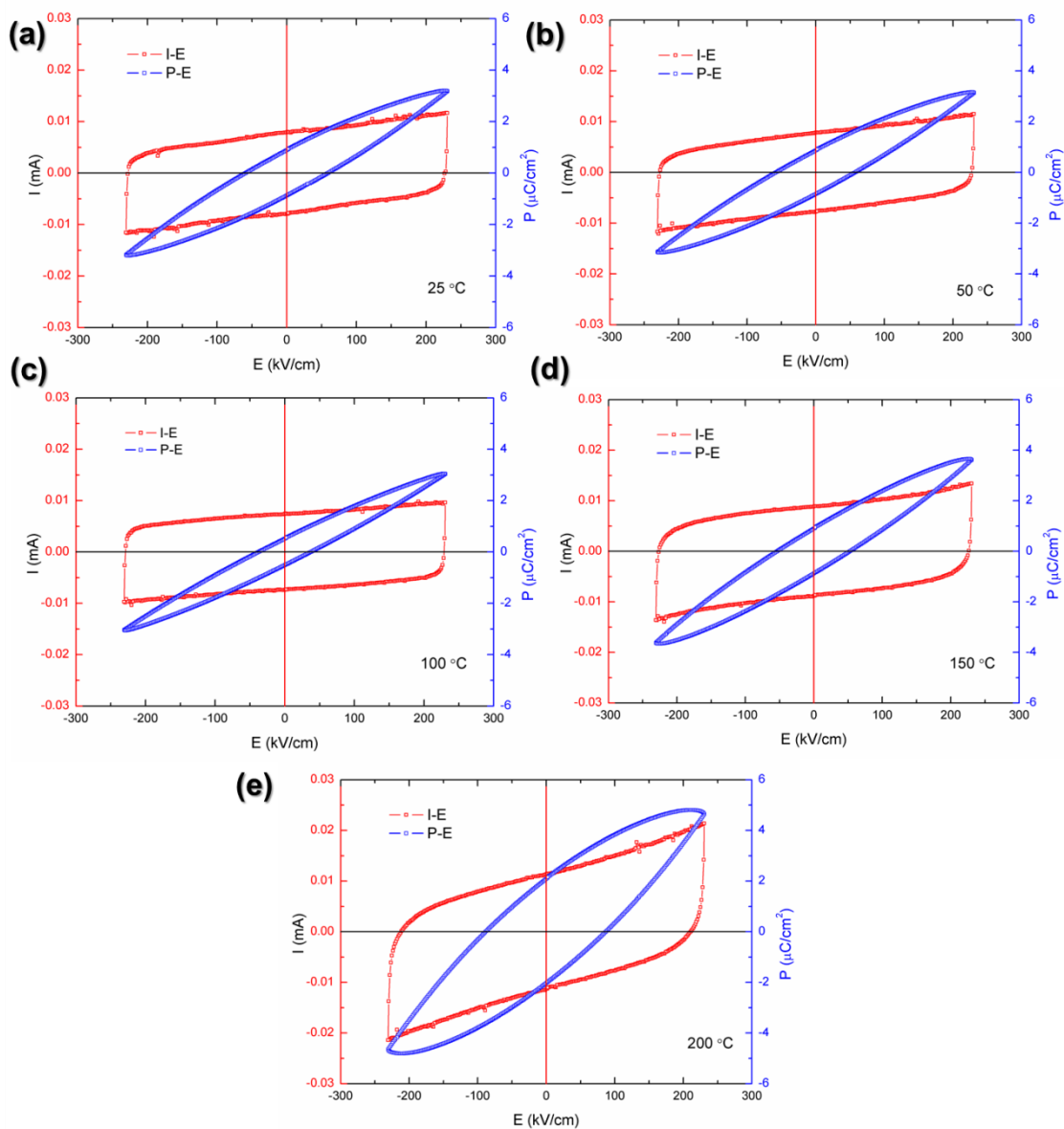
Fig. 4.3.11 Current-electric field (*I-E*) and polarization-electric field (*P-E*) hysteresis loops of M-LaTaO$_4$ ceramic measured from room temperature to 200 ℃ under an AC field up to 230 kV/cm: (a) 25 ℃; (b) 50 ℃; (c) 100 ℃; (d) 150 ℃; (e) 200 ℃.
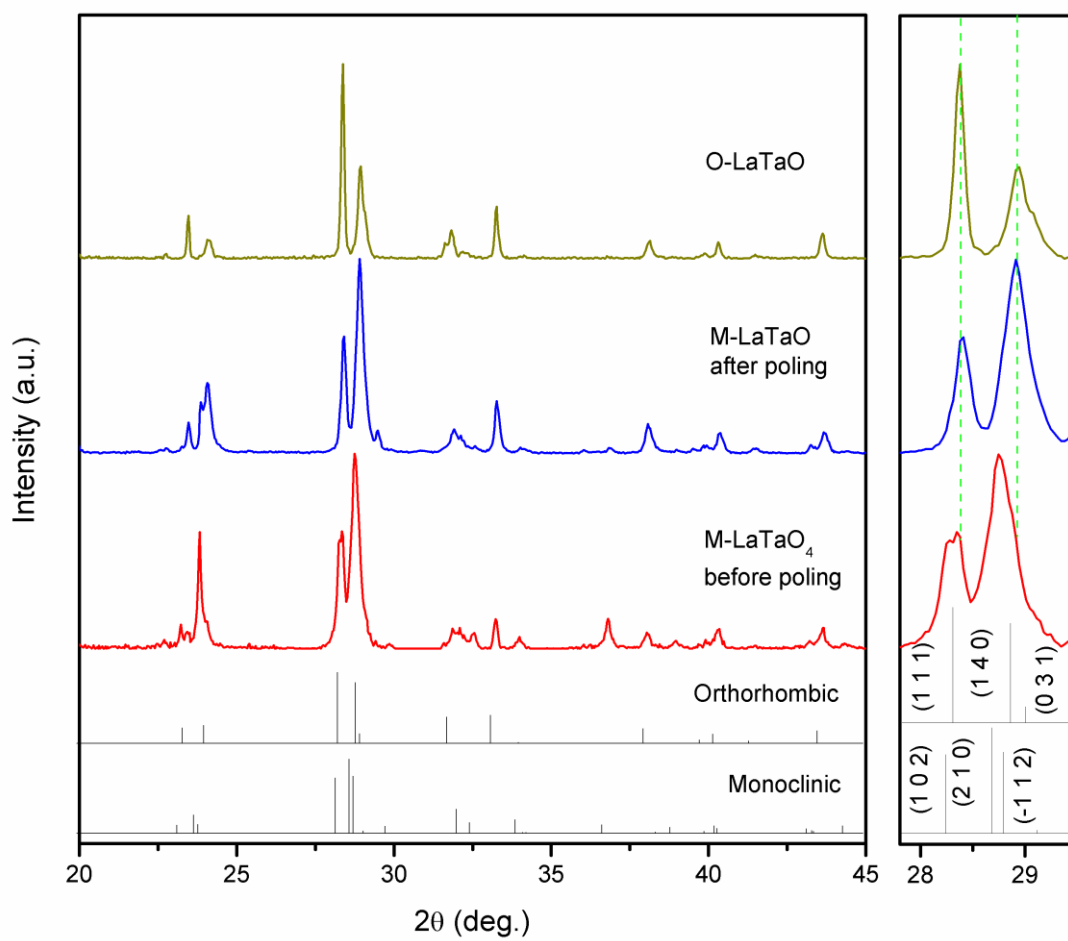
Fig. 4.3.12 XRD patterns of M-LaTaO$_4$ ceramic before and after poling.

4.3.4 Conclusions

LaTaO$_4$ powders were prepared using the SSR method. Lower calcination temperatures (<1300 °C) lead to incomplete reaction of the raw materials; Higher calcination temperatures (>1300 °C) lead to a biphase structure with orthorhombic and monoclinic phases. Pure LaTaO$_4$ powders with orthorhombic phase were be prepared by CP synthesis. The O-LaTaO$_4$ powders have a 2-layer perovskite-like layered structure with space group *A2$_1$am*, which was refined using Rietveld method. Single phase O-LaTaO$_4$ ceramic was prepared using SPS with a low cooling rate (20 °C/min). An irreversible phase transition at about 695 °C was detected by study the temperature dependence of dielectric permittivity and loss, and the O-LaTaO$_4$ ceramic transferred into a biphase after the *T$_c$* measurement. The M-LaTaO$_4$ ceramic can transfer into orthorhombic phase under high DC electric field. A *d$_{33}$* of 0.3 pC/N was obtained from the electric field induced orthorhombic phase.

Chapter V. Results - 2-layer Dion-Jacobson Compounds

5.1 CsBiNb$_2$O$_7$ Compound

5.1.1 Introduction

Compared with the $A_nB_nO_{3n+2}$ type PLS compounds, materials with Dion-Jacobson structure have rarely been reported to present ferroelectricity. Fennie *et al*. demonstrated the polar nature of CsBiNb$_2$O$_7$ using first principles and group theoretical analysis and estimated that CsBiNb$_2$O$_7$ has a spontaneous polarization of 40 µC/cm^2.[63] However, Goff *et al*. reported that the ferroelectricity of CsBiNb$_2$O$_7$ cannot be detected due to its large leakage current and significant proton conductivity.[66]

In this work, we present the ferroelectriciy and piezoelectricity of CsBiNb$_2$O$_7$ ceramics by direct evidence of ferroelectric domain switching and piezoelectric activity. The ferroelectric domain structures of CsBiNb$_2$O$_7$ were investigated using PFM images. The Curie point for CsBiNb$_2$O$_7$ was found to be 1033±5 by studying the temperature dependence of permittivity and thermal depoling.

5.1.2 Experimental Procedure

The $CsBiNb_2O_7$ powders were prepared by heating stoichiometric amounts of Cs_2CO_3 (4% excess), Bi_2O_3 and Nb_2O_5 in air at 1000 ℃ for 4 hours using a conventional furnace. The ceramics were sintered between 800 ~ 900 ℃ using an SPS furnace. A heating rate of 100 ℃/min was used and a pressure of 50 MPa was applied during the SPS process to obtain ceramics with high density. For ceramics with grain orientation, the direction of a plane with a normal line parallel to the SPS pressing direction is defined as the parallel direction (//) and the normal line perpendicular to the pressing direction is the perpendicular direction (⊥). Raman spectra were detected by a Nicolet Almega XR dispersive Raman Spectrometer. An X-ray photoelectron spectroscopy meter was used to determine the chemical state of different elements in the samples. Piezoresponse force microscopy (PFM) was used to observe the ferroelectric domain structure. Samples were fired with a platinum paste to produce electrodes for electrical properties measurements.

5.1.3 Results and Discussion

The XRD data of CsBiNb$_2$O$_7$ powders calcined at 1000 ℃ were refined using the Rietveld method. The non-centrosymmetric orthorhombic space group *P2₁am* was used as the refinement model.[62, 66] The refinement results are shown in Fig. 5.1.1, and the crystal data and refinement parameters are shown in Table 5.1.1. The calculated pattern fits well with the experimental data, and the relatively low χ^2 and *R* factors indicate that the CsBiNb$_2$O$_7$ powders have a pure non-centrosymmetric orthorhombic structure. Preferred (0 0 *l*) orientation correction was considered to improve the fit during the refinement. The (0 0 *l*) orientation in the XRD pattern is caused by the relative large plate-like grains which is shown in Fig. 5.1.3(a).
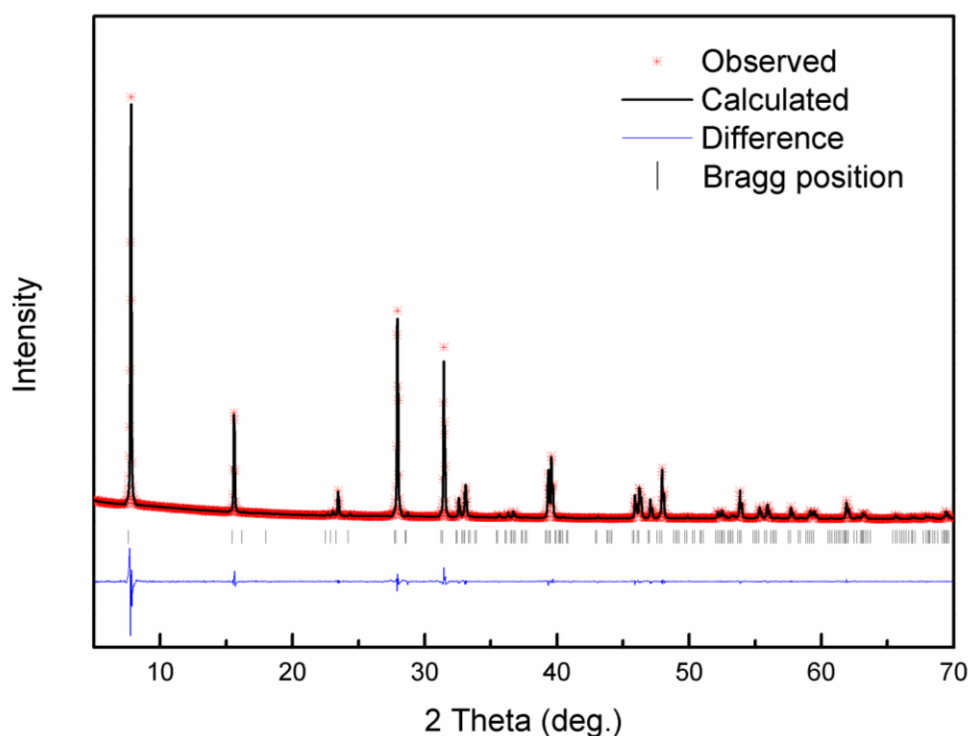

Fig. 5.1.1 Rietveld refinement result of CsBiNb$_2$O$_7$ powders.

Table 5.1.1 Crystal data and refinement parameters of $CsBiNb_2O_7$.

Compound	$CsBiNb_2O_7$
Crystal system	Orthorhombic
Space group	*P2₁am* (26)
a (Å)	5.49645(14)
b (Å)	5.42242(14)
c (Å)	11.37704(16)
V (Å³)	339.020(13)
Z	2
Reduced χ^2	4.989
No. of variables	30
R_{wp} (%)	8.66
R_p (%)	5.66
R_F2	9.73

Fig. 5.1.2 shows the XRD patterns of $CsBiNb_2O_7$ ceramics from both the planes perpendicular and parallel to the SPS pressing direction. A small impurity diffraction peak is observed around 30 °, which is indexed to be Bi_2O_3. The impurity is supposed to be caused by the volatilization of Cs^+ due to the high vacuum environment during the SPS process. Because of the plate-like grains and high pressure during the SPS, all of the $CsBiNb_2O_7$ ceramics after SPS were highly textured. The preferred orientation factor from (0 0 *l*) planes of $CsBiNb_2O_7$ ceramics is 0.7.
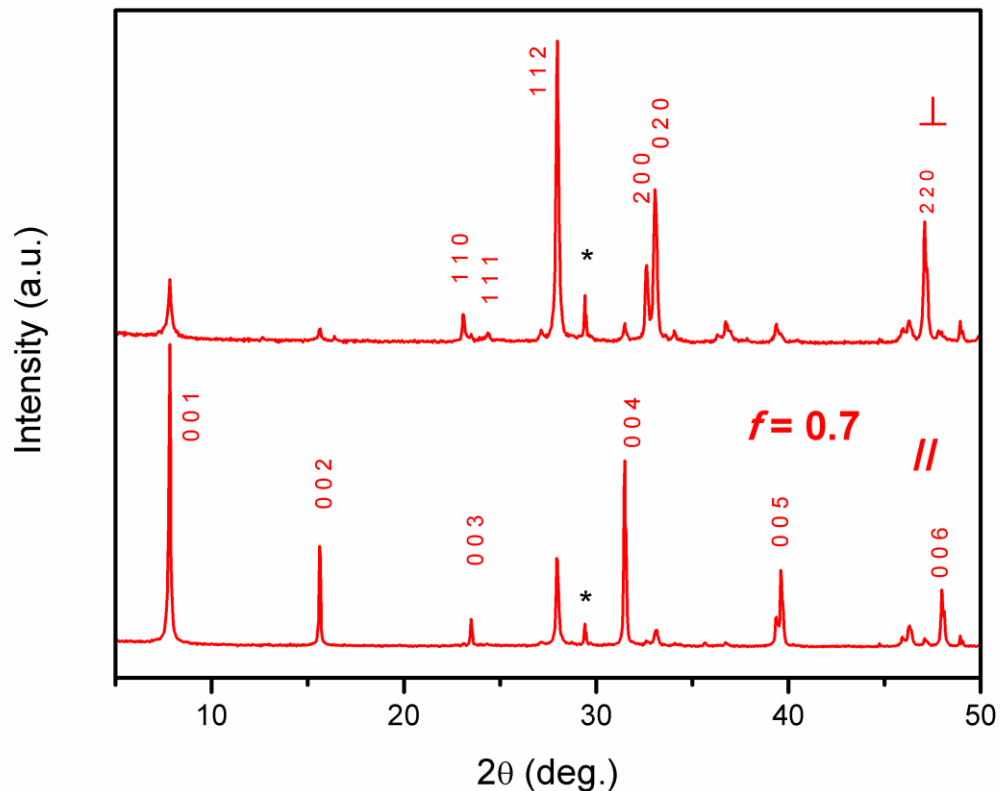
Fig. 5.1.2 XRD patterns of CsBiNb$_2$O$_7$ ceramics from both the planes perpendicular and parallel to the SPS pressing direction.

Fig. 5.1.3 shows the SEM and HRTEM images of CsBiNb$_2$O$_7$ powders and ceramics. Fig 5.1.3(a) shows the plate-like grains of calcined CsBiNb$_2$O$_7$ powders. Fig 5.1.3(c) and (d) shows fractured surface of the sintered ceramics from the planes parallel and perpendicular to the SPS pressing directions, respectively. The plate-like powders were highly textured after SPS due to the pressure. Fig 5.1.3(b) shows a HRTEM image of CsBiNb$_2$O$_7$ ceramic. Unfaulted lattice planes are observed. The *d*-pacing of the lattice planes was measured to be 1.12±0.02 nm. A selected area electron diffraction pattern is shown in inset in Fig. 5.1.3(b). The linear reflections were indexed to be (0 0 *l*) lattice

planes. The *d*-spacing of the (0 0 *l*) plane, which corresponds to the length of *c* axis of
the unit cell, was measured to be 1.13±0.02 nm.
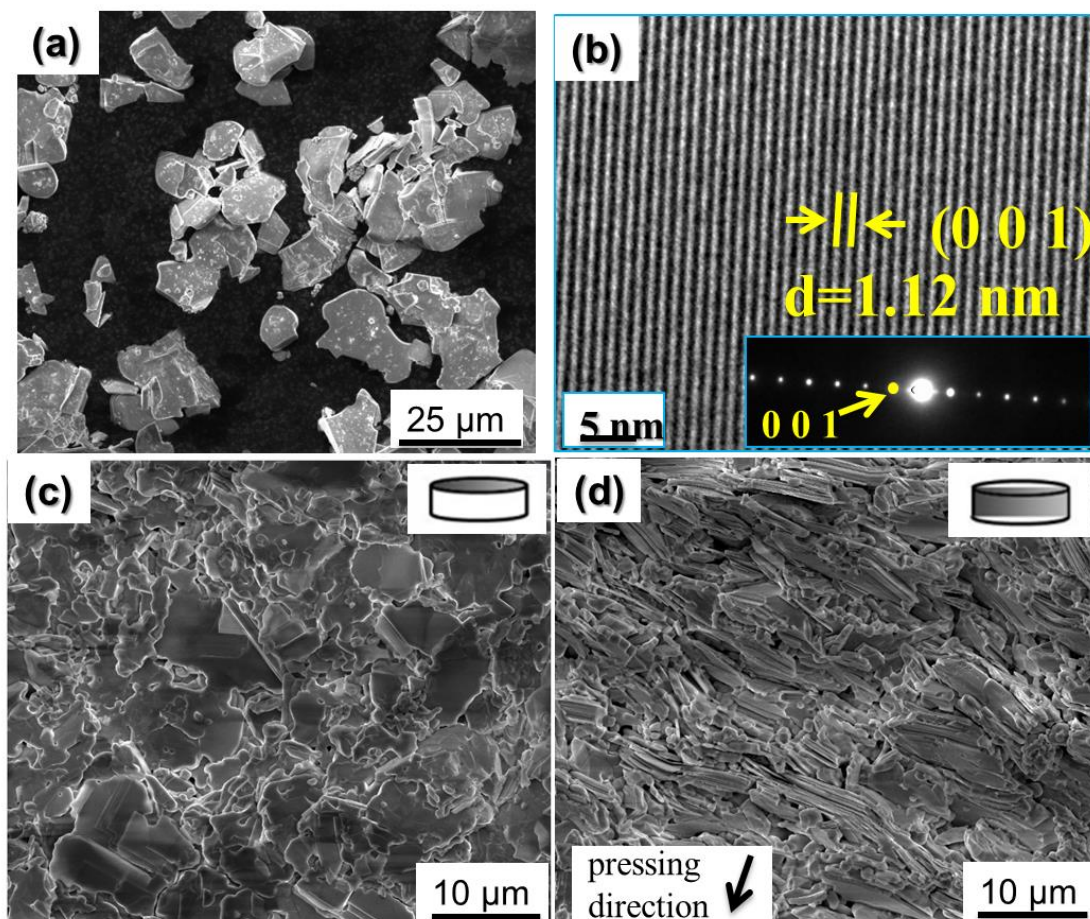
Fig. 5.1.3 SEM images of $CsBiNb_2O_7$: (a) calcined powders; (b) HRTEM image of the ceramic;
(c) ceramic surface fractured along the direction parallel to the pressing direction; (d) ceramic
surface fractured along the direction perpendicular to the pressing direction.

Fig. 5.1.4 and 5.1.5 show the XPS spectra of $CsBiNb_2O_7$ powders and ceramics.
Doublet components due to spin-orbit splitting can be observed from the spectra of Cs
3d, Bi 4f and Nb 3d as shown in Fig. 5.1.4.[92, 105] No obvious difference between powder
and ceramic can be observed from the spectra of those three elements. The 5/2 and 3/2

spin-orbit doublet components of Cs 3d are located at 724.5 and 738.5 eV, respectively. The binding energy (BE) of Cs 3d agrees with the reported values for Cs^{1+}.[113] The spin-obit splitting of the Cs 3d core level is 14 eV (13.9 eV for CsOH).[113] The BE of Bi 4f doublet components and Nb 3d doublet components and their spin-orbit splitting energies are similar to those reported values for Bi^{3+} and Nb^{5+} in Aurivillius compounds such as $Na_{0.5}Bi_{2.5}Nb_2O_9$ [92] and $Bi_4Ti_3O_{12}$.[114-116]

Fig. 5.1.5 shows the O 1s spectra of $CsBiNb_2O_7$. After Gauss-Lorentz fitting, two different component peaks are identified for the powders and three different component peaks are identified for the ceramic. For the powders, the first peak at lower BE side (~529 eV) corresponds to the Nb-O bond inside the perovskite layer. Similar O 1s spectra were reported for Aurivillius compounds. According to their explanations, the peak with lower BE corresponds to the Nb-O or Ti-O bonds and the peak with higher BE is attributed to the oxygen attached to the *A*-site cation.[92, 114] Because Dion-Jacobson materials have similar perovskite layer with Aurivillius materials in their structures, it is reasonable to assign the O 1s peak with higher BE (~530.8 eV) to the contribution from the oxygen attached to Cs^+. For the ceramic, the two peaks at lower BE part are consistent with their powders. The component peak with high BE (~532.9 eV) can be assigned to surface adsorbed water or oxygen vacancies.[116-118] As no O 1s peak associated with surface adsorbed water can be observed in the powder spectra, the high BE peak is assigned to oxygen vacancies which is caused by the vacuum environment during SPS process.
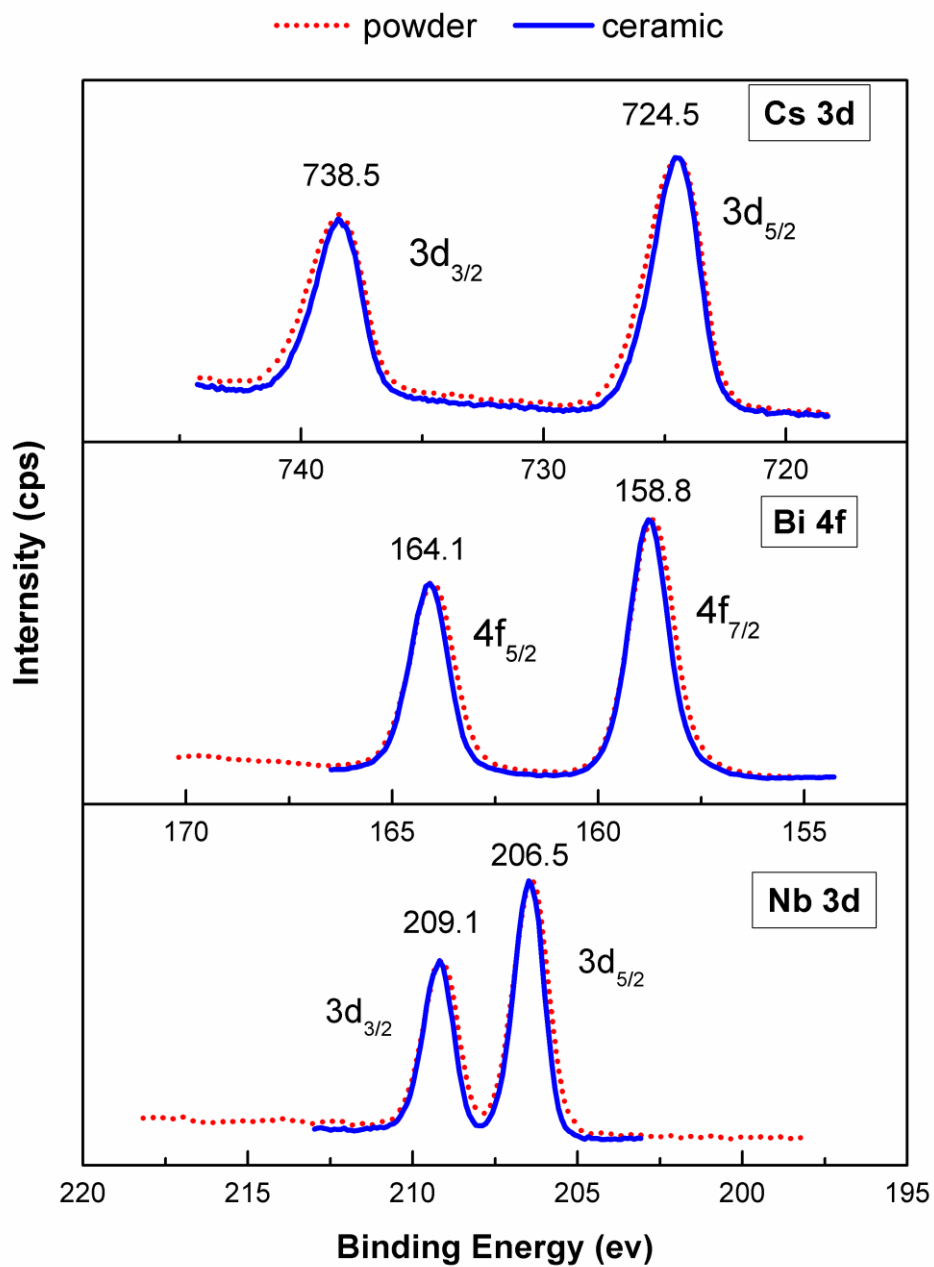
Fig. 5.1.4 X-ray photoelectron spectra of Cs 3d, Bi 4f and Nb 3d in $CsBiNb_2O_7$.
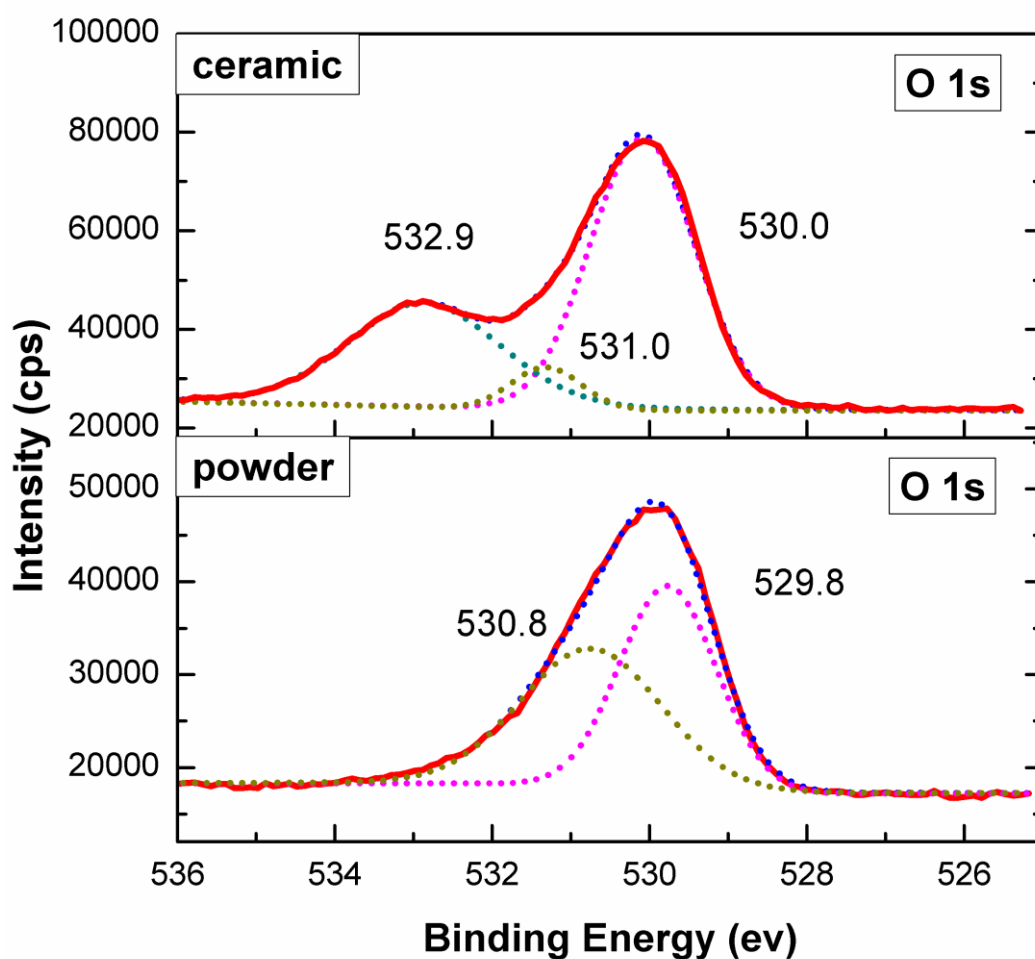
Fig. 5.1.5 X-ray photoelectron spectra of O 1s in $CsBiNb_2O_7$.

The temperature dependence of the dielectric constants and loss of $CsBiNb_2O_7$ are shown in Fig. 5.1.6. The Curie point of $CsBiNb_2O_7$ is 1033±5 °C. The ferroelectric-to-paraelectric phase transition temperature for $CsBiNb_2O_7$ is demonstrated for the first time. Goff *et al*. reported that the orthorhombic phase of $CsBiNb_2O_7$ was stable from room temperature to 900 °C and no ferroelectric orthorhombic to paraelectric tetragonal phase transition was observed using high-temperature XRD,[66] which is in agreement with our result that the T_c (~1033 °C) of $CsBiNb_2O_7$ is above 900 °C.
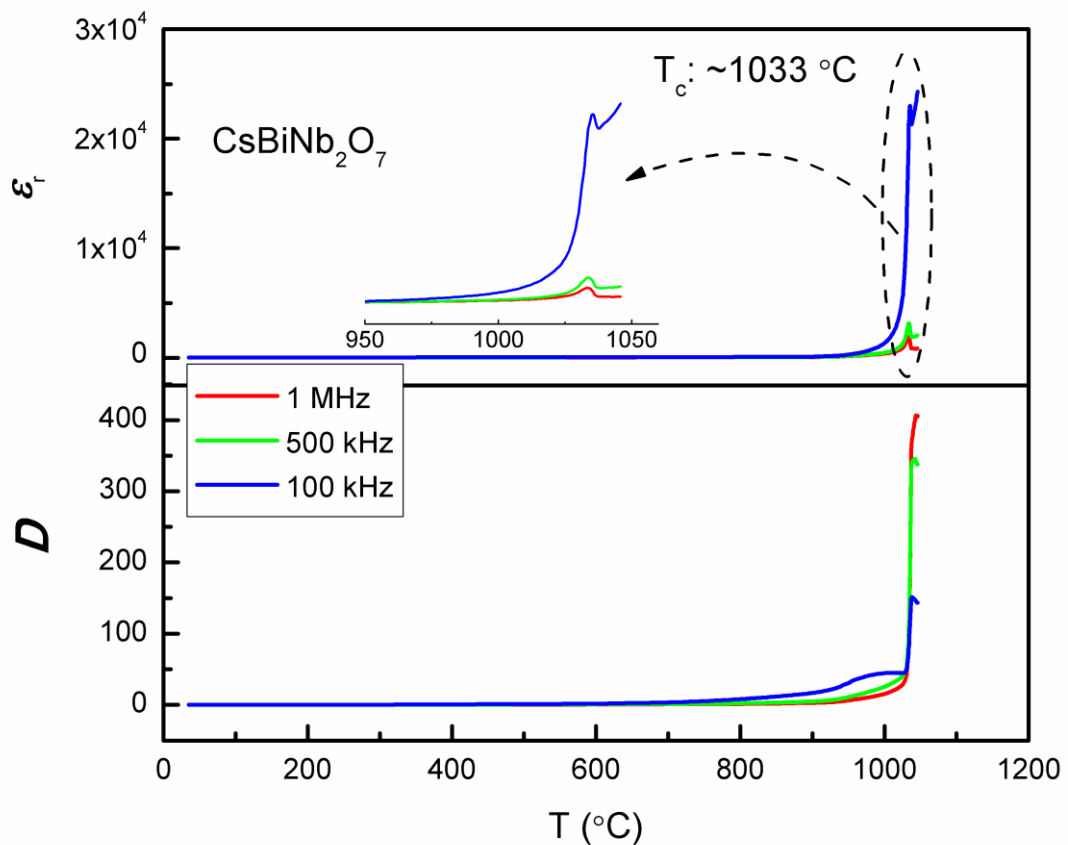
Fig. 5.1.6 Temperature dependence of dielectric constant and loss of $CsBiNb_2O_7$ ceramic.

The electric displace placement (*D*) for ferroelectrics mainly consists of three contributions from ferroelectric domain switching (*P*), electric conductivity (*D*₁) and dielectric displacement (*D*₂). For most ferroelectric ceramics, the contributions from D_1 and D_2 are negligible, *D-E* hysteresis loops are usually described as *P-E* hysteresis loops,[119] but in this case for $CsBiNb_2O_7$ ceramics, the contribution from electric conductivity cannot be neglected due to their high electric loss at room temperature. Fig. 5.1.7 shows the current-electric field (*I-E*) and electric displacement-electric field (*D-E*) hysteresis loops of $CsBiNb_2O_7$. The *I-E* and *D-E* loops were measured at 110 ℃ and 10 Hz. A typical, unsaturated, ferroelectric *D-E* loop was obtained for $CsBiNb_2O_7$. In its *I-*

E loop, a current peak (marked by arrow) produced by ferroelectric domain switching is observed.
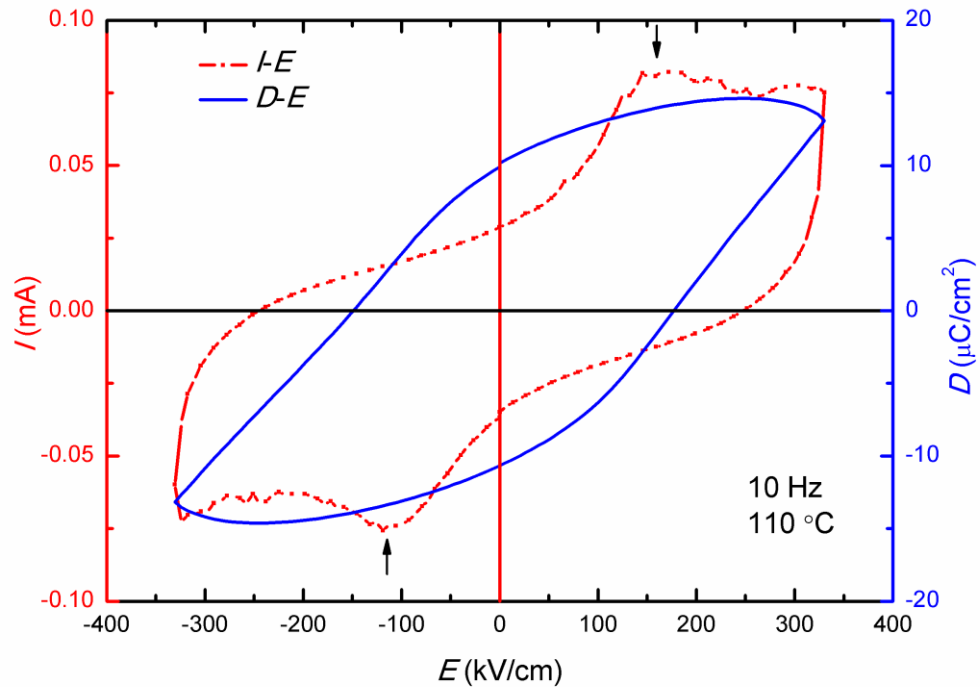
Fig. 5.1.7 *I-E* and *D-E* hysteresis loops of CsBiNb$_2$O$_7$ ceramic measured at 110 ℃ and 10 Hz. The arrows indicate the current peaks produced by ferroelectric domain switching.

CsBiNb$_2$O$_7$ has the polar orthorhombic structure *P2$_1$am*. Due to the off-centre displacements of *A*-site Bi ions and octahedral tilting of NbO$_6$, a spontaneous polarization develops along the *a*-axis. Recently, Benedek reported that the origin of ferroelectricity in polar oxides with Dion-Jacobson phases is induced by a combination of octahedral distortions and cation ordering.[60] The macroscopic polarization of CsBiNb$_2$O$_7$ was reported to be 48 µC/cm^2 using symmetry principles, crystal chemical models, and first-principles calculations. Here the spontaneous polarization was calculated to be 43.8 µC/cm^2 for CsBiNb$_2$O$_7$ according to Shimakawa's model,[97, 120] which is in good agreement with Benedek's report. The ion displacements along the *a*-

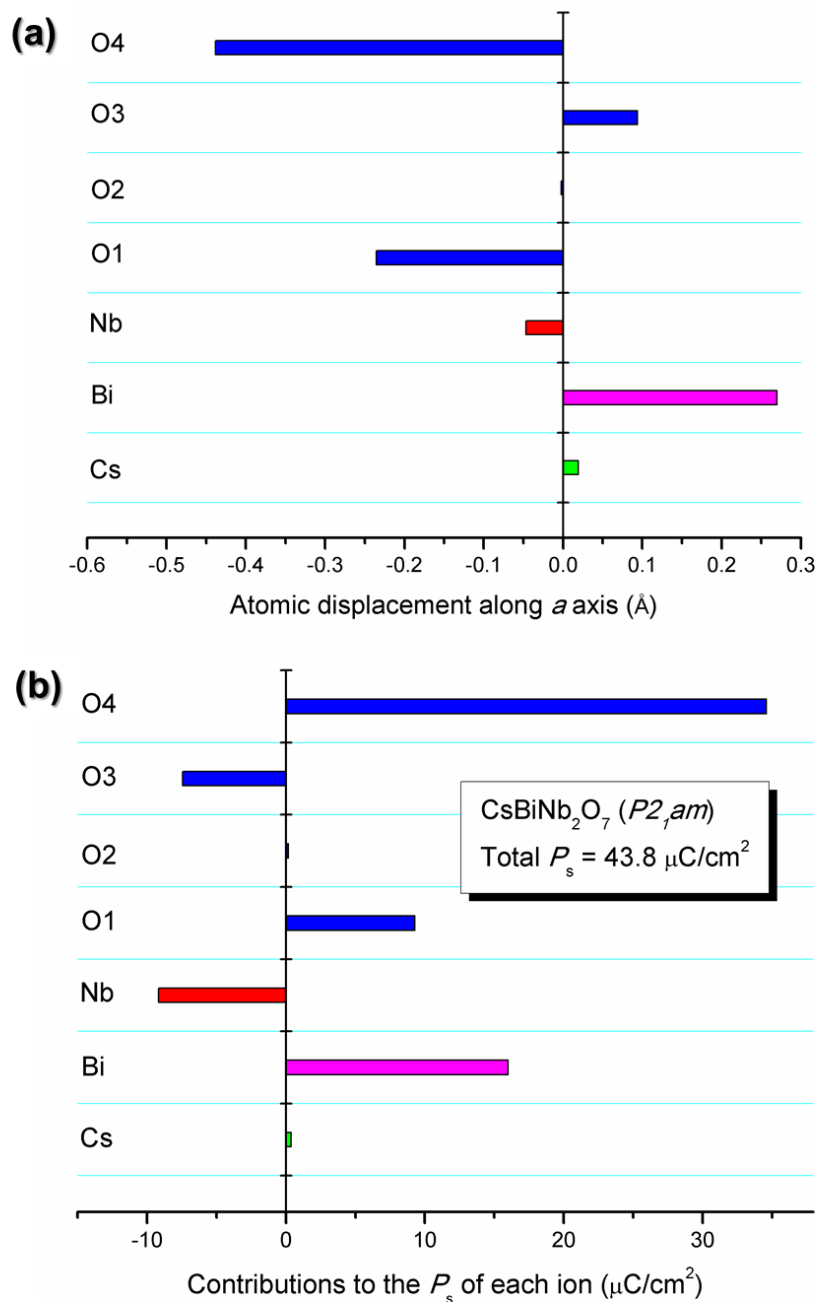axis and the contributions of each ion to the total ferroelectric polarization are shown in

Fig. 5.1.8.

Fig. 5.1.8 Ion displacement and contribution to the total spontaneous polarization of each ion of

$CsBiNb_2O_7$.

Fig. 5.1.9 shows vertical-mode PFM images of $CsBiNb_2O_7$ ceramic. Because the SPS sintered ceramics were highly textured on the (0 0 *l*) plane and the polar axis is in the *a*-direction, samples with surfaces perpendicular to the SPS pressing direction were prepared to investigate the ferroelectric domain structure with PFM. Several grains with clear grain boundaries can be observed in the topography image shown in Fig. 5.1.9(a). Ferroelectric domain morphology is clearly observed in the PFM amplitude and phase images (Fig. 5.1.9(b) and (c)). Bright areas in the amplitude image reveal the stripe domains with vertical piezo-response signal. Some of the dark areas reveal regions with in-plane polarization. The bright and dark areas in the phase image reveal the up and down out-of-plane polarization, respectively. Comparing the PFM amplitude and phase images with the topography image, clear ferroelectric domains can be observed in several grains (A to E), and stripe domains with different orientations show strong contrast in each grain. Fig. 5.1.9(d) shows the schematic of the out-of-plane and in-plane polarization in grain A. The black, yellow and orange stripes represent the dark, bright and grey areas. The polarization direction can be indexed through comparing the phase and amplitude images. The width of the domains was typically from 10 to 600 nm.
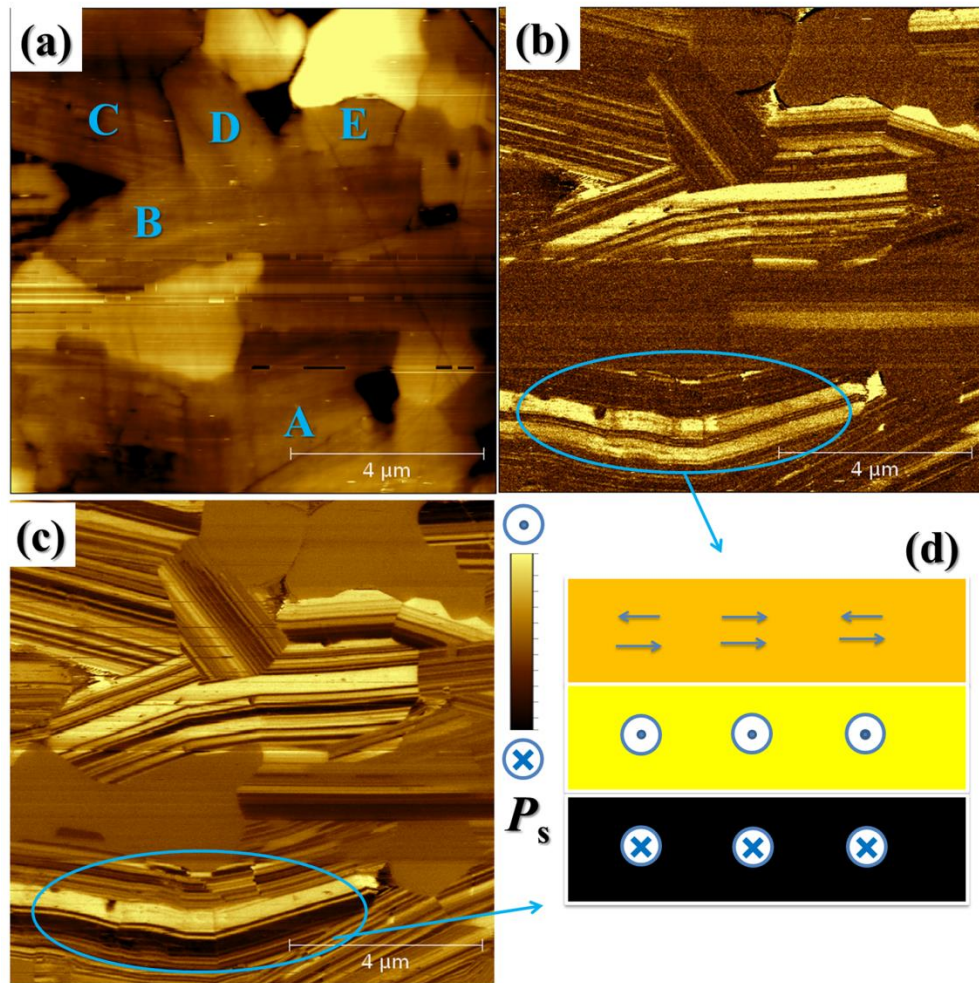
Fig. 5.1.9 Vertical-mode PFM images of CsBiNb$_2$O$_7$ ceramic: (a) topography; (b) amplitude; (c)

phase and (d) schematic of the selected area from (c).

The measured piezoelectric constant d_{33} at room temperature was 8±0.5 pC/N for

CsBiNb$_2$O$_7$. Fig. 5.1.10 shows the thermal depoling results for poled CsBiNb$_2$O$_7$. All of

the samples poled at room temperature were annealed at different temperatures for 2

hours. Then their d_{33} values were measured at room temperature. The d_{33} values of

CsBiNb$_2$O$_7$ are very stable with increasing depoling temperature. The d_{33} starts to drop

when the depoling temperature is close to T_c and tends to zero above T_c.
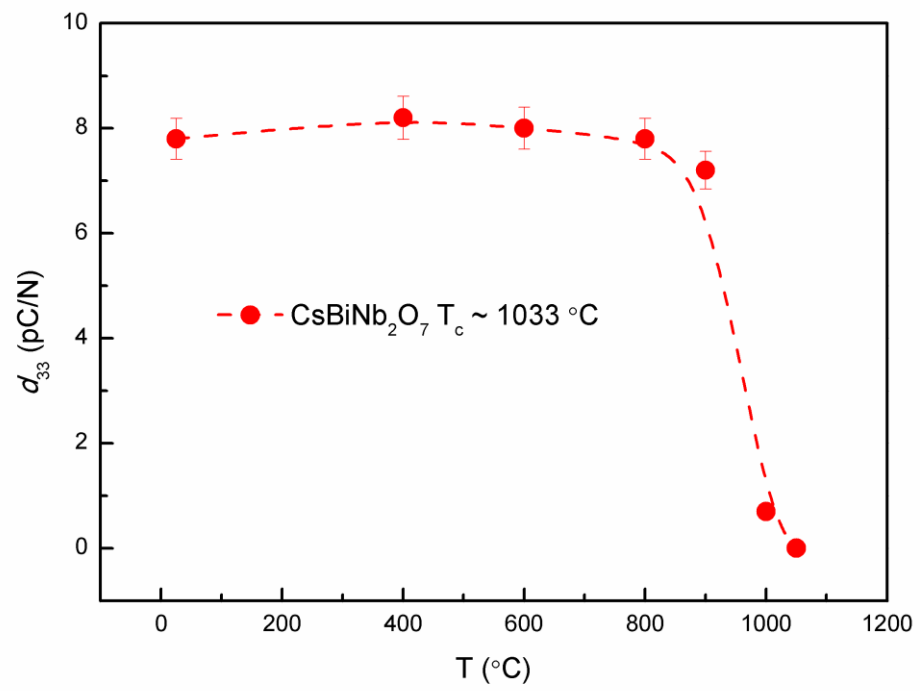
Fig. 5.1.10 Thermal depoling results of poled CsBiNb$_2$O$_7$ ceramic.

5.1.4 Conclusions

In summary, 2-layer Dion-Jacobson $CsBiNb_2O_7$ powders were synthesized and found to have pure *P2₁am* orthorhombic structure using Rietveld refinement. Highly textured $CsBiNb_2O_7$ ceramics were prepared by one-step spark plasma sintering with pressure due to their layered crystal structure, which was demonstrated using XRD. High resolution TEM showed well ordered (0 0 1) lattice planes. The ferroelectricity and piezoelectricity of $CsBiNb_2O_7$ are demonstrated for the first time. The T_c of $CsBiNb_2O_7$ is 1033±5 °C. The piezoelectric constant of $CsBiNb_2O_7$ is approximately 8 pC/N. Striped ferroelectric domains were observed using PFM. Thermal depoling studies confirm the T_c measurements and the stability of the piezoelectricity.

5.2 RbBiNb$_2$O$_7$ Compound

5.2.1 Introduction

RbBiNb$_2$O$_7$ was reported to have the same structure as CsBiNb$_2$O$_7$.[61] The RbBiNb$_2$O$_7$ ceramics were recently reported to be ferroelectric by Li, *et al*. recently.[64] The Curie point of RbBiNb$_2$O$_7$ was determined to be 945 °C from measurements of the dielectric constant with increasing the temperature. They also demonstrated the ferroelectricity using *P-E* loops tests, but no saturated *P-E* loop or clear polarization switching signal can be observed. In this work, we demonstrate the ferroelectricity of RbBiNb$_2$O$_7$ ceramics by direct evidence of ferroelectric switching in *P-E* and *I-E* loops. The ferroelectric domain structures of RbBiNb$_2$O$_7$ were also investigated using PFM images. The Curie point of RbBiNb$_2$O$_7$ was found to be 1098±5 °C by studying the temperature dependence of permittivity and thermal depoling. This result corrects the inaccurate T_c result reported by Li.

5.2.2 Experimental Procedure

The RbBiNb$_2$O$_7$ powders were prepared by heating stoichiometric amounts of Rb$_2$CO$_3$ (4% excess), Bi$_2$O$_3$ and Nb$_2$O$_5$ in air at 1000 ℃ for 4 hours using a conventional furnace. The ceramics were sintered between 800 ~ 900 ℃ using an SPS furnace. A heating rate of 100 ℃/min was used and a pressure of 50 MPa was applied during the SPS process to obtain ceramics with high density. Raman spectra were detected by a Nicolet Almega XR dispersive Raman Spectrometer. An x-ray photoelectron spectroscopy meter was used to determine the chemical state of different elements in the samples. Piezoresponse force microscopy (PFM) was used to observe the ferroelectric domain structure. Samples were fired with a platinum paste to produce electrodes for electrical properties measurements.

5.2.3 Results and Discussion

Fig. 5.2.1 shows the XRD pattern of $RbBiNb_2O_7$ powders calcined at 1000 ℃ and SPS sintered ceramics from orientations perpendicular and parallel to the SPS pressing direction. The $RbBiNb_2O_7$ powders have a pure orthorhombic structure *P2$_1$am* indexed with PDF#45-0039. No obvious impurity peaks from Bi_2O_3 are observed from the sintered ceramics. Like $CsBiNb_2O_7$, $RbBiNb_2O_7$ powders have plate-like grains (Fig. 5.2.2(a)), and the SPS sintered ceramics shows strong grain orientation. The preferred orientation factor from (0 0 *l*) planes of $RbBiNb_2O_7$ ceramics is 0.9.

Fig. 5.2.2 shows the SEM and HRTEM images of $RbBiNb_2O_7$ powders and ceramics. Fig 5.2.2(c) and (d) show fractured surfaces of the sintered $RbBiNb_2O_7$ ceramics from orientations parallel and perpendicular to the SPS pressing directions, respectively. Strong grains orientation is observed, which is consistent with the XRD results shown in Fig 5.2.1. Fig 5.2.2(b) shows a HRTEM image of $RbBiNb_2O_7$ ceramic. Perfect lattice planes, similar with $CsBiNb_2O_7$ (Fig. 5.1.3(b)), are also observed in $RbBiNb_2O_7$ ceramic. The *d*-pacing of the lattice planes was measured to be 1.08±0.02 nm. The inset in Fig. 5.1.3(b) shows the corresponding selected area electron diffraction pattern. The linear reflections were indexed to be (0 0 *l*) lattice planes. The *d*-spacing of the (0 0 *l*) plane, which corresponds to the length of *c* axis of the unit cell, was measured to be 1.10±0.02 nm.
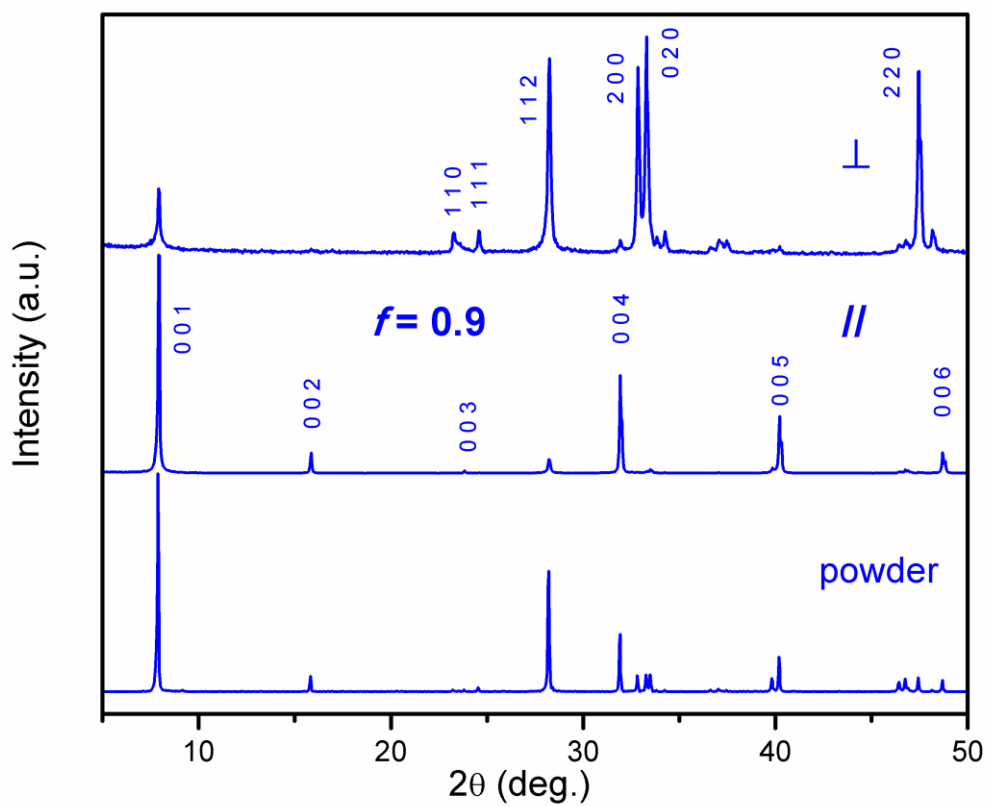
Fig. 5.2.1 XRD patterns of RbBiNb$_2$O$_7$ powder, and ceramics from both the planes

perpendicular and parallel to the SPS pressing direction.
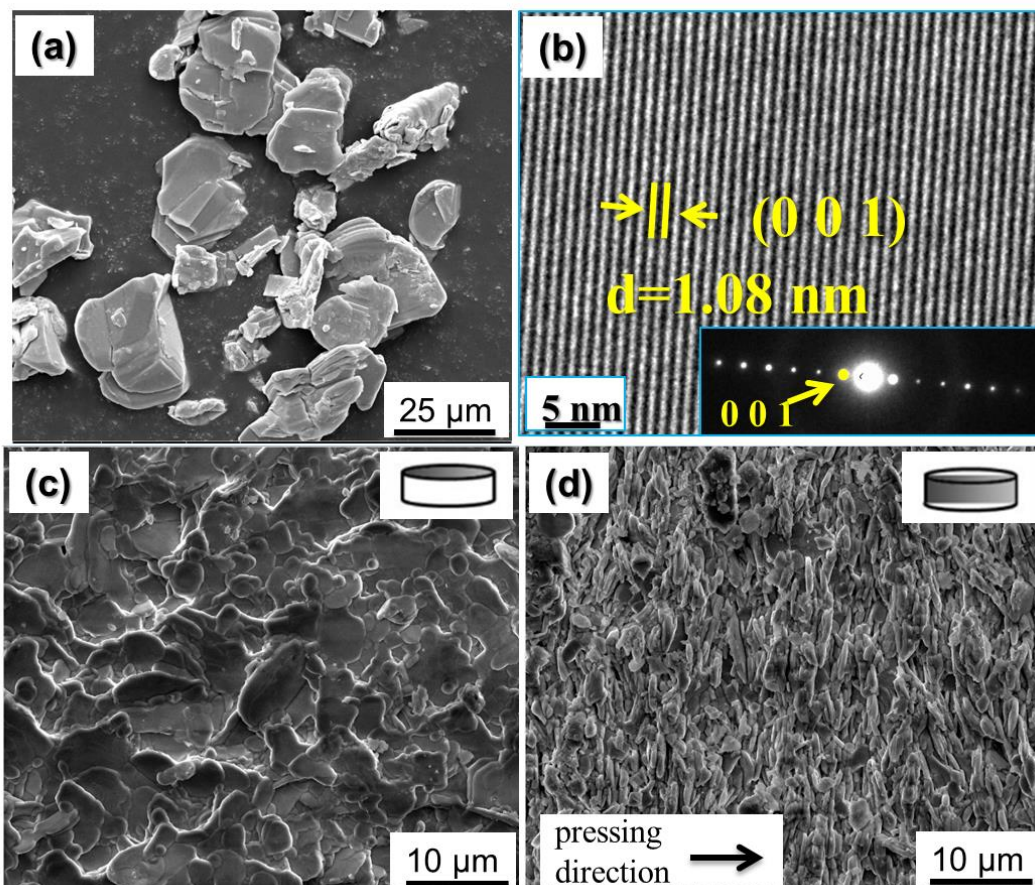
Fig. 5.2.2 SEM images of $RbBiNb_2O_7$: (a) calcined powders; (b) HRTEM image of the ceramic; (c) ceramic surface fractured along the direction parallel to the pressing direction; (d) ceramic surface fractured along the direction perpendicular to the pressing direction.

The XPS spectra of Bi 4f and Nb 3d of $RbBiNb_2O_7$ are shown in Fig. 5.2.3. The BE of Bi 4f ($4f_{5/2}$: 164.0 eV, $4f_{7/2}$: 158.7 eV) and Nb 3d ($3d_{3/2}$: 209.2 eV, $3d_{5/2}$: 206.4 eV) in $RbBiNb_2O_7$ are similar with that in $CsBiNb_2O_7$ (Bi $4f_{5/2}$: 164.1 eV, $4f_{7/2}$: 158.8 eV, and Nb $3d_{3/2}$: 209.1 eV, $3d_{5/2}$: 206.5 eV) shown in Fig. 5.1.4. This is because that $CsBiNb_2O_7$ and $RbBiNb_2O_7$ have the same perovskite-like layered structure. In their crystal structures, both the A-site Bi^{3+} in 12-fold coordination and B-site Nb^{5+} in 6-fold coordination are inside the perovskite layer. According to some reports, Bi^{3+} and Nb^{5+}

in almost all of the PLS materials show similar BE and spin-orbit splitting due to their similar perovskite layers.[92, 105, 114-116, 121]
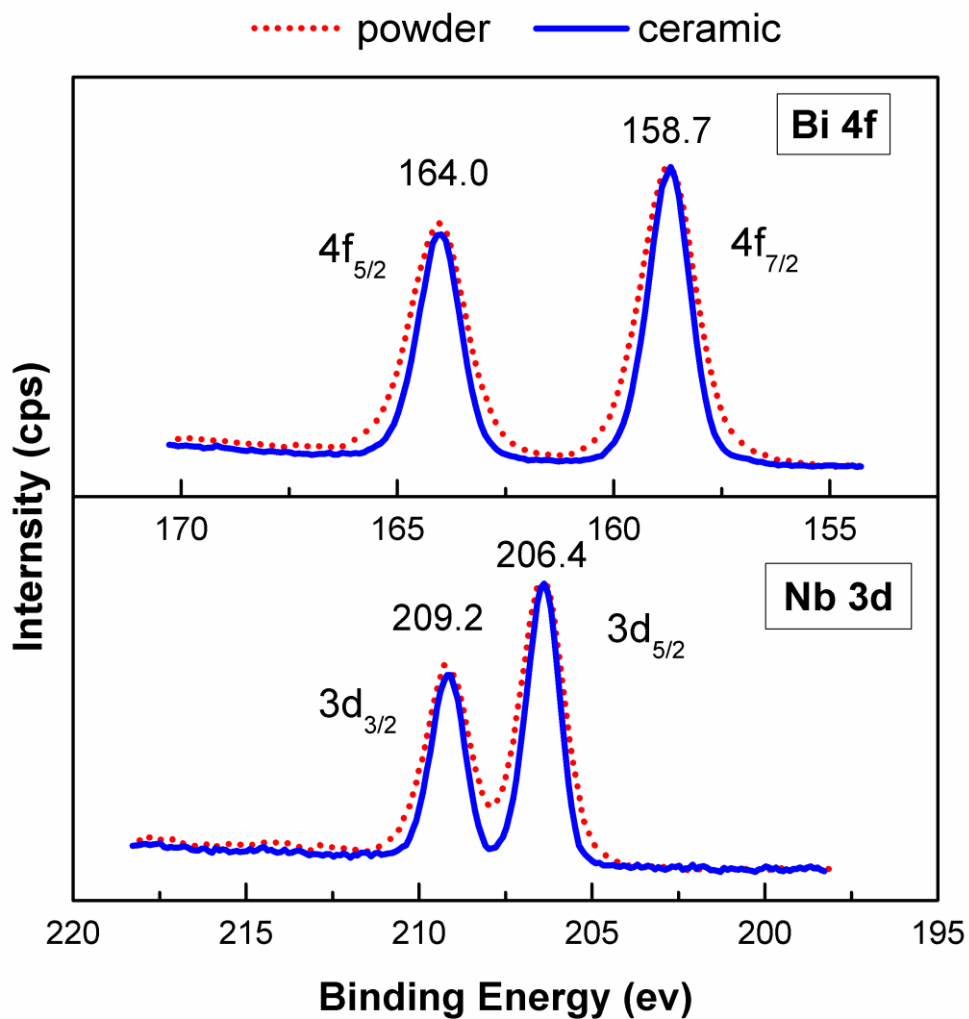
Fig. 5.2.3 X-ray photoelectron spectra of Bi 4f and Nb 3d in $RbBiNb_2O_7$.

Fig. 5.2.4 shows the spectra of Rb 3d for the $RbBiNb_2O_7$ powder and ceramic. Two spin-orbit splitting peaks are obtained using a Gauss-Lorentz method fitting. The BE of Rb 3d of the powder are similar with that of the ceramic. It can be observed from the Rb

3d, Bi 4f and Nb 3d spectra of $RbBiNb_2O_7$ ceramic that their peaks are narrower than that of the powders.
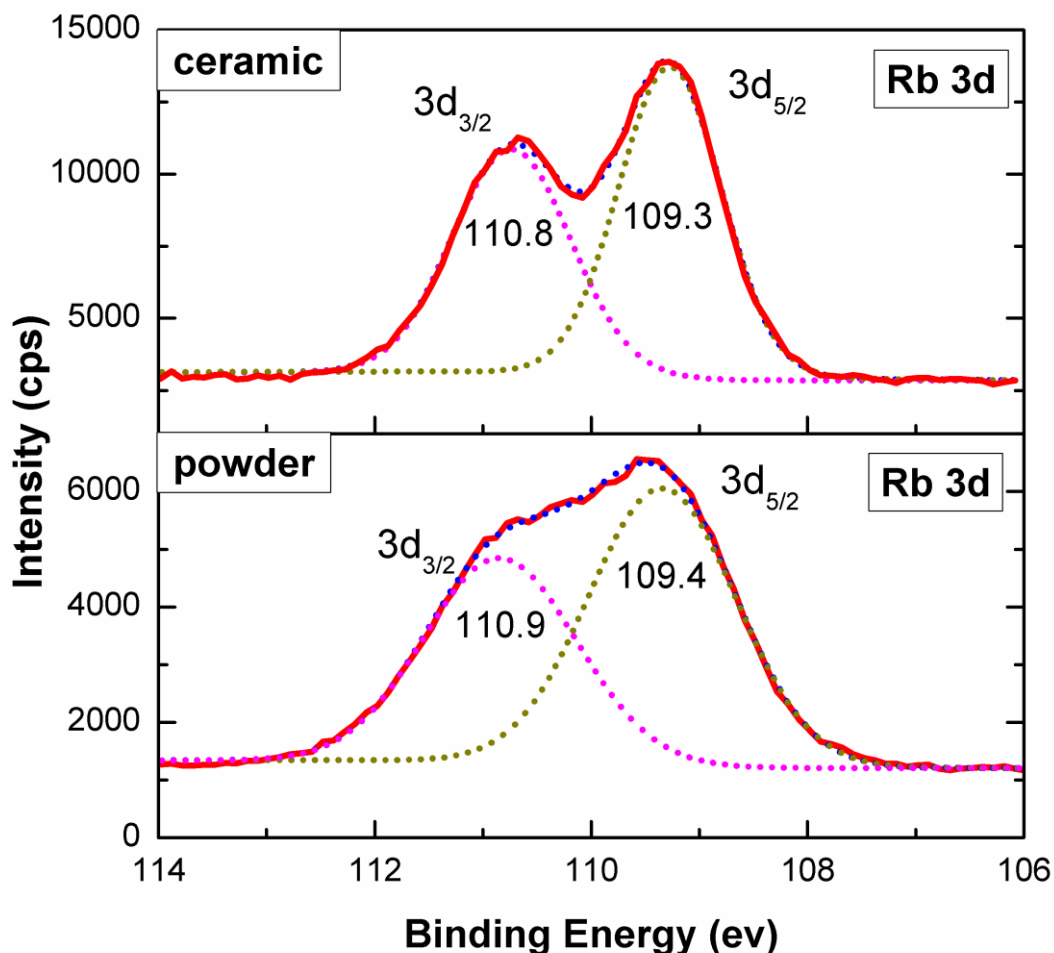
Fig. 5.2.4 X-ray photoelectron spectra of Rb 3d in $RbBiNb_2O_7$.

Fig. 5.2.5 shows O 1s spectra of $RbBiNb_2O_7$. Like O 1s in $CsBiNb_2O_7$ (Fig. 5.1.5), two component peaks are obtained from the powders and three component peaks are obtained from the ceramics by Gauss-Lorentz fitting. For powders, the O 1s peak with lower BE (~529.8 eV) is assigned to the Nb-O bond inside the perovskite layer, and the peak with higher BE (~531 eV) is assigned to the contribution from the oxygen attached

to Rb^+. For ceramics, the two peaks at low BE part are consistent with their powders. The component peak with high BE (~532.7 eV) is assigned to oxygen vacancies which is caused by the vacuum environment during SPS process.
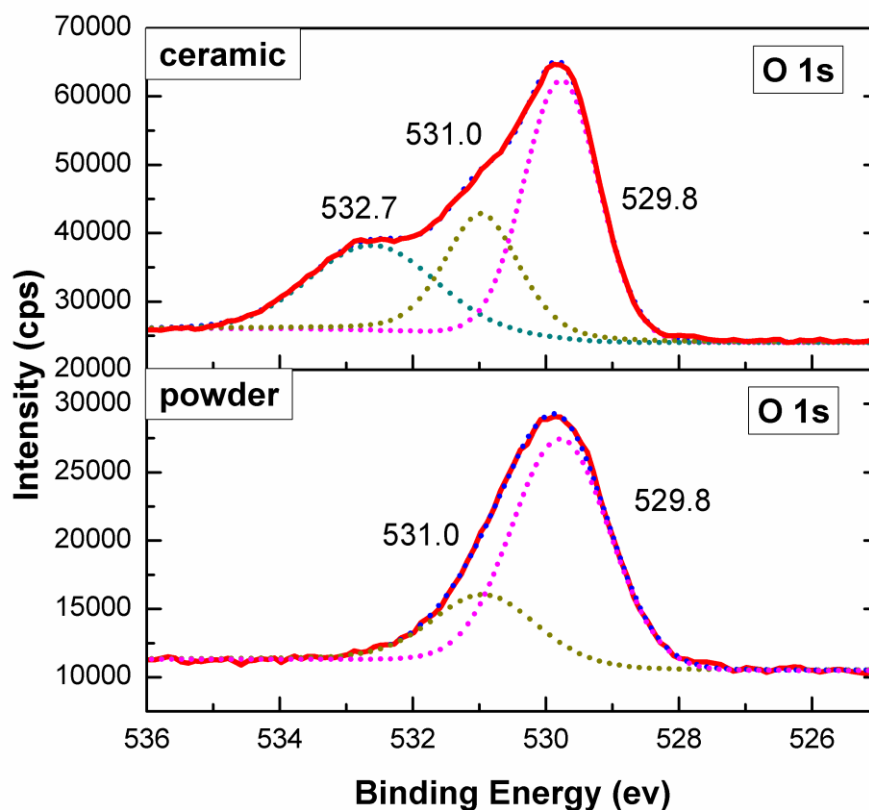
Fig. 5.2.5 X-ray photoelectron spectra of O 1s in $RbBiNb_2O_7$.

For XPS analysis, BE is a useful parameter to analyse the chemical state of elements in materials. But due to different X-ray source, experimental conditions and energy scale calibration, the BE values for the same element with the same chemical state can vary, which makes it not easy to compare results with different references. V.V. Atuchin used BE difference Δ(O-M) = BE(O 1s)- BE(M) to analyse the chemical state of different

elements in oxides and it was demonstrated to be a more effective method.[106, 108, 121, 122]

Table 5.2.1 shows the Δ(O-Nb) = BE(O 1s)- BE(Nb $3d_{5/2}$) and Δ(O-Bi) = BE(O 1s)-

BE(Bi $4f_{7/2}$) for $CsBiNb_2O_7$ and $RbBiNb_2O_7$ and some other materials with perovskite-

layered structure from the literatures. The BE difference Δ(O-Nb) can represent the

chemical sate of the Nb-O bonds in the NbO_6 octahedra. The Δ(O-Nb) of $CsBiNb_2O_7$ is

323.5 eV, which is similar with that of $RbBiNb_2O_7$ (323.4 eV). Compared with that of

$Sr_2Nb_2O_7$ (323 eV) [105], the values are very close. According to the reference,[121] the Δ(O-

Nb) of some oxides with Nb^{5+} show a range from 322.4 to 323.6 eV. The BE difference

Δ(O-Bi) can be used to describe the Bi-O bonds inside the perovskite layers. The Δ(O-

Bi) of $CsBiNb_2O_7$ (371.2 eV) and $RbBiNb_2O_7$ (371.1 eV) are almost the same, which

are also similar with that from the Aurivillius compound $Bi_4Ti_3O_{12}$ (370.6 eV).[123] From

the study of Δ(O-Nb) and Δ(O-Bi) BE difference, it can be concluded that the NbO_6

octahedra and perovskite layers of DJ compounds $CsBiNb_2O_7$ and $RbBiNb_2O_7$ show

similar chemical features with other PLS compounds.

Table 5.2.1 XPS data of $CsBiNb_2O_7$, $RbBiNb_2O_7$ and other PLS compounds

Compound	Binding Energy (eV)				
	O 1s	Nb $3d_{5/2}$	Bi $4f_{7/2}$	Δ(O-Nb)	Δ(O-Bi)
$CsBiNb_2O_7$ (Bulk)	530	206.5	158.8	323.5	371.2
$RbBiNb_2O_7$ (Bulk)	529.8	206.4	158.7	323.4	371.1
$Sr_2Nb_2O_7$ [105]	530	207	/	323	/
$Bi_4Ti_3O_{12}$ [123]	529.8	/	159.2	/	370.6

Raman spectra of $RbBiNb_2O_7$ and $CsBiNb_2O_7$ in the range from 300 cm^{-1} to 1000 cm^{-1}

measured at room temperature are shown in Figure 5.2.6. The spectrum of $CsBiNb_2O_7$

exhibits intense phonon modes at 321, 343, 382, 465, 555, 581, 689, 826, 875 and 935

cm^{-1}. These phonon modes are related to its orthorhombic layer structure, which are similar to those of $KCa_2Nb_3O_{10}$ (3-layer DJ compound).[124] The modes at 935 and 343 cm^{-1} are related to the distorted NbO_6 octahedral structure.[92, 124] For $RbBiNb_2O_7$, the modes at 939 and 345 cm^{-1} are weaker than that of $CsBiNb_2O_7$, which implies that the distortion of NbO_6 octahedra in $RbBiNb_2O_7$ is weaker than that of $CsBiNb_2O_7$. The modes at 826 and 875 cm^{-1} are caused by vibrations of oxygen irons in O-Nb-O chain. There is an obvious shift to lower frequencies (785 and 833 cm^{-1}) for the modes for $RbBiNb_2O_7$. This shift is caused by the lower mass and smaller ionic radius of Rb (0.172 nm) at *A*-site compared with that of Cs (0.188 nm).[93] The modes at 689, 581 and 555 cm^{-1} could be related to the Bi-O force constant, and the mode at 382 cm^{-1} and 321 cm^{-1} are related to the vibration of Cs-O bonds and the vibration of Nb-O bonds, respectively.[93, 125-127]
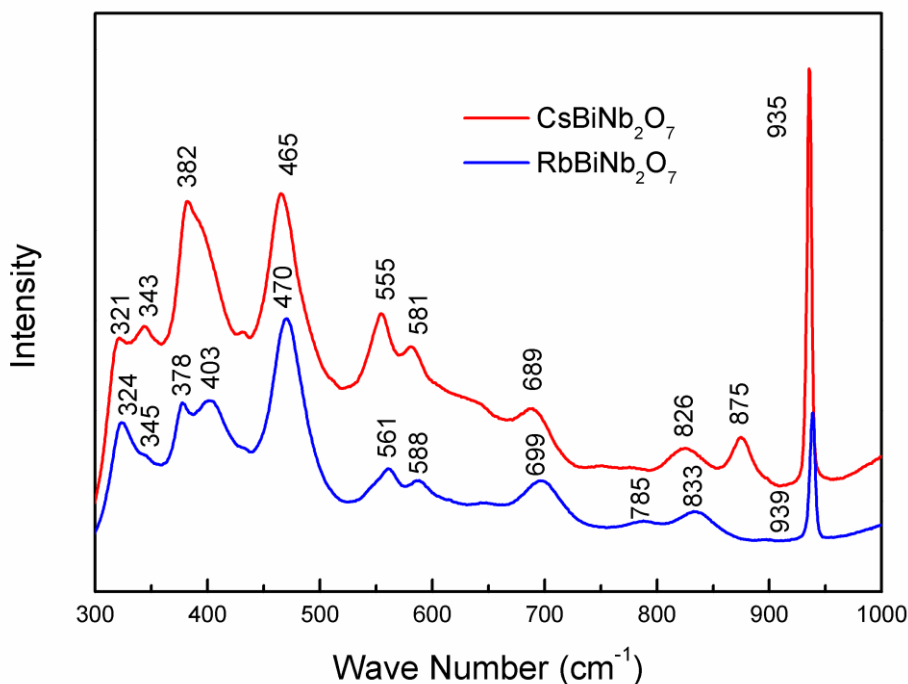
Fig. 5.2.6 Raman spectra of $RbBiNb_2O_7$ and $CsBiNb_2O_7$.

Fig. 5.2.7 shows the temperature dependence of dielectric constants and loss of RbBiNb$_2$O$_7$. The Curie point of RbBiNb$_2$O$_7$ is 1098±5 °C. The T_c of RbBiNb$_2$O$_7$ was first reported to be 943 °C by Li *et al*,[64] which is about 155 °C lower than our result. To calibrate our equipment, the T_c of LiNbO$_3$ single crystal was measured with the same equipment. The T_c of LiNbO3 was measured as ~1138 °C. According to the literature,[128] the T_c of single crystal LiNbO$_3$ is 1140°C, which means that the T_c values we measured are accurate within the errors.
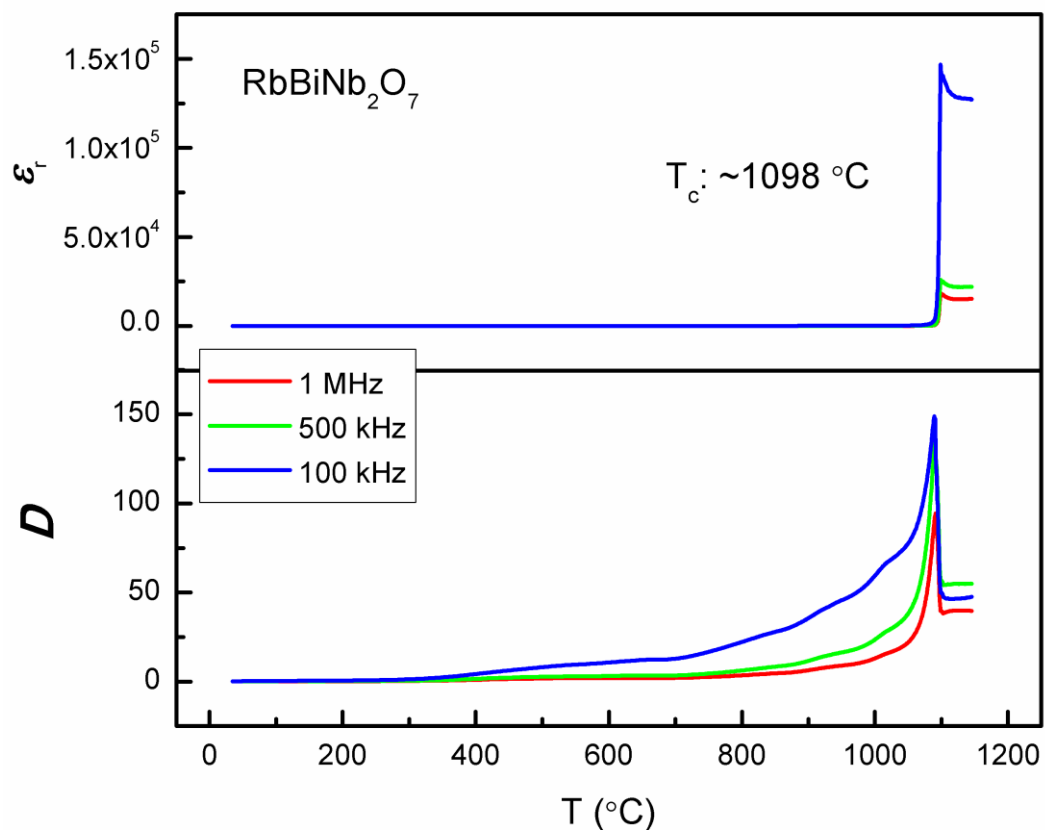
Fig. 5.2.7 Temperature dependence of dielectric constant and loss of RbBiNb$_2$O$_7$ ceramic.

At first *I-E* and *D-E* hysteresis loops of $CsBiNb_2O_7$ and $RbBiNb_2O_7$ were measured at room temperature and 10 Hz. Vesica piscis-shaped *D-E* hysteresis loops due to leakage current were obtained from both $CsBiNb_2O_7$ and $RbBiNb_2O_7$, and no contribution from ferroelectric domain switching was observed from their *I-E* loops.[66, 119] Fig. 5.2.8 shows the *I-E* and *D-E* hysteresis loops of $RbBiNb_2O_7$ measured at 200 ℃ and 10 Hz. A typical vesica piscis-shaped *D-E* loop due to leakage current is observed, but the ferroelectric domain switching is demonstrated by the peak observed in the *I-E* loop.
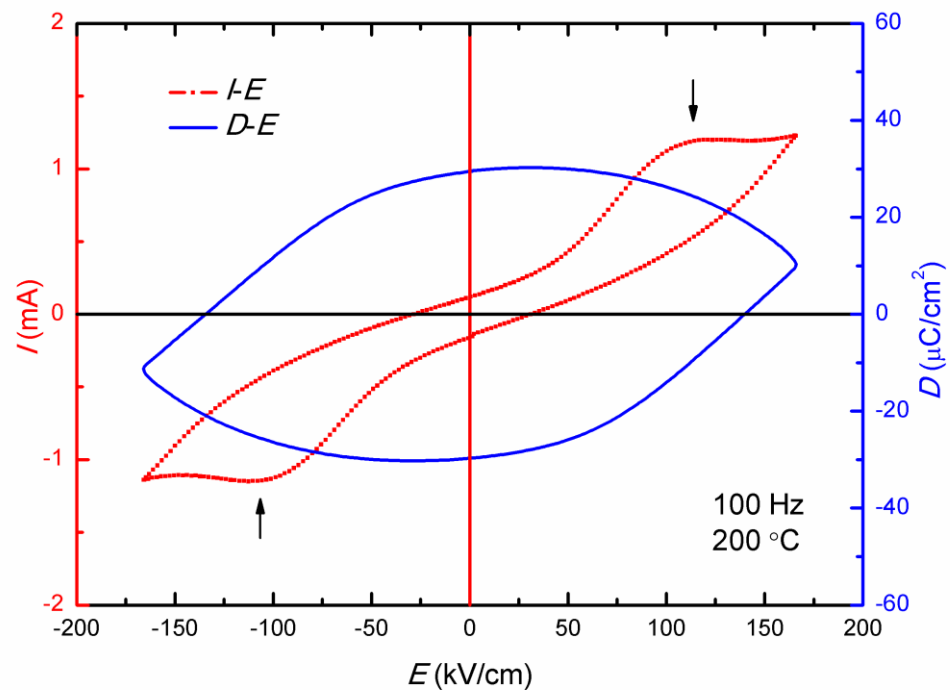
Fig. 5.2.8 *I-E* and *D-E* hysteresis loops of $RbBiNb_2O_7$ ceramic measured at 200 ℃ and 100 Hz. The arrows indicate the current peaks produced by ferroelectric domain switching.

Fig. 5.2.9 shows vertical-mode PFM images of $RbBiNb_2O_7$ ceramic. Due to the high roughness of the surface, no clear grain boundaries can be observed from the

topography (Fig. 5.2.9(a)). Fig. 5.2.9(b) shows the phase image. Clear ferroelectric domain structure can be observed, which is similar with the domain structure in CsBiNb$_2$O$_7$ (Fig. 5.1.9). The bright and dark areas in the phase image reveal the up and down out-of-plane polarization, respectively.
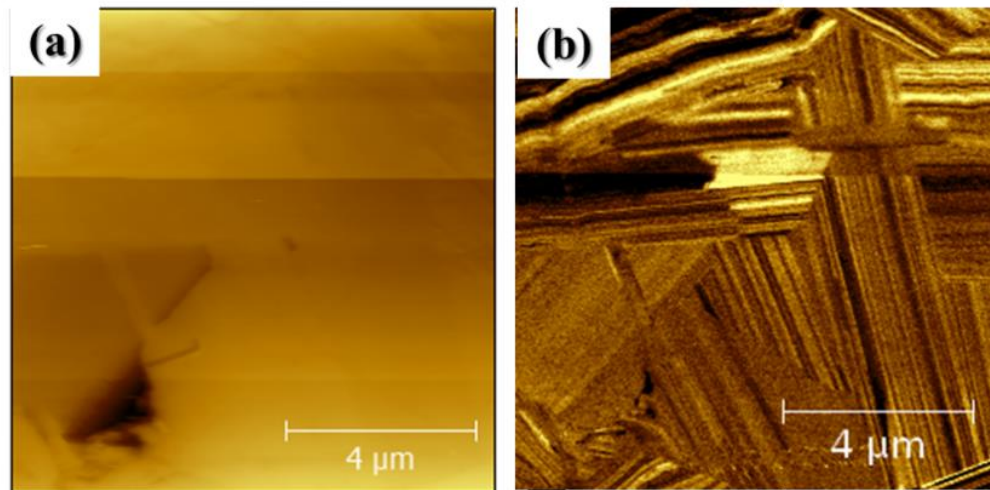
Fig. 5.2.10 Vertical-mode PFM images of RbBiNb$_2$O$_7$ ceramic: (a) topography; (b) phase.

RbBiNb$_2$O$_7$ has the same polar orthorhombic structure *P2$_1$am* with CsBiNb$_2$O$_7$. Its spontaneous polarization develops along its *a*-axis. The macroscopic polarization of RbBiNb$_2$O$_7$ was reported to be 48 μC/cm^2 using symmetry principles, crystal chemical models, and first-principles calculations by Recently Benedek.[60] Here the spontaneous polarization was calculated to be 47 μC/cm^2 for RbBiNb$_2$O$_7$ according to Shimakawa's model,[97, 120] which is in good agreement with Benedek's report. The ion displacements along the *a*-axis and the contributions of each ion to the total ferroelectric polarization are shown in Fig. 5.2.10.
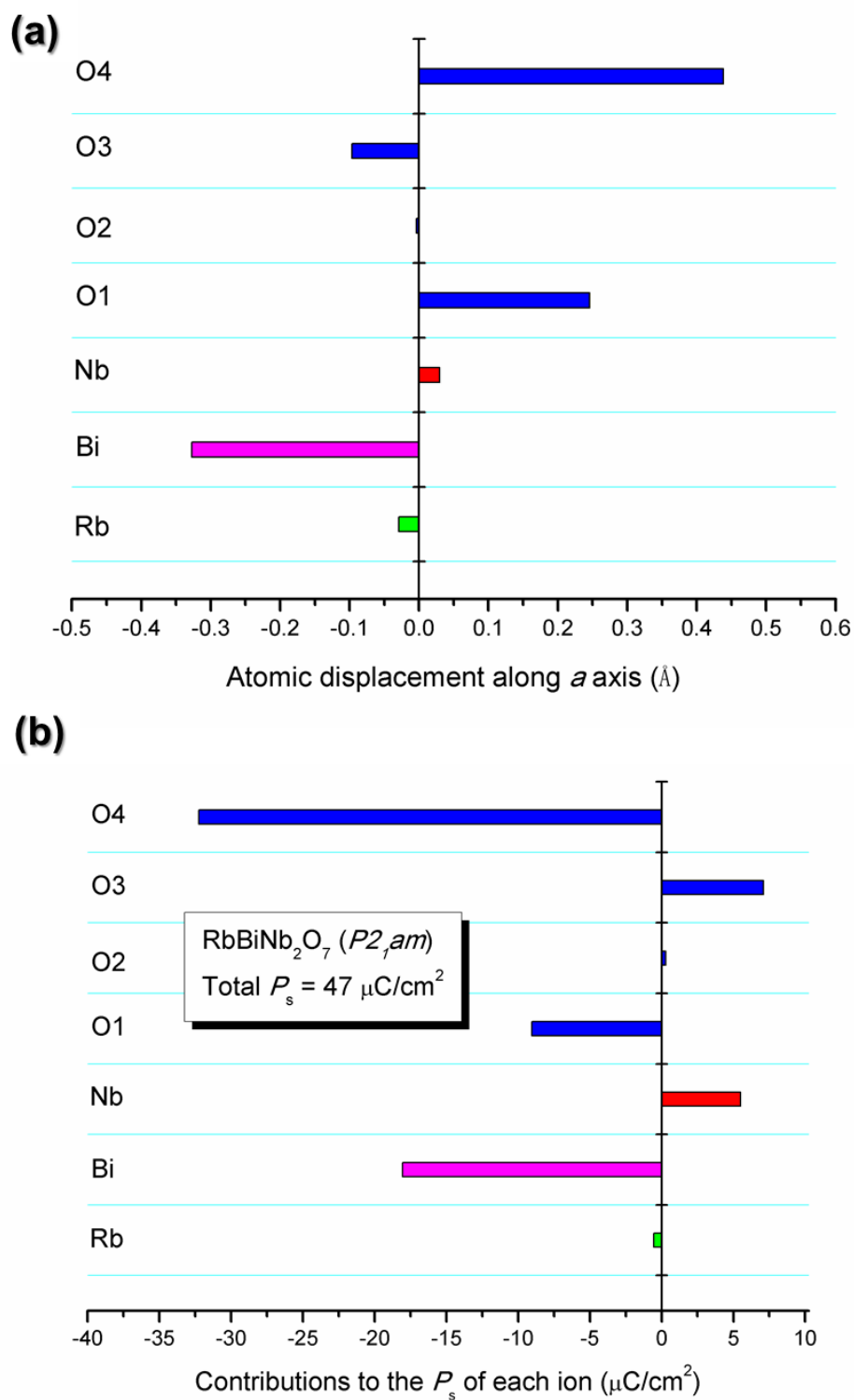
Fig. 5.2.10 Ion displacement and contribution to the total spontaneous polarization of each ion

of RbBiNb₂O₇.

Because the SPS sintered ceramics are highly textured along (0 0 l) planes in the parallel orientation and the spontaneous polarization is along a-axis, all of the samples were poled along the perpendicular direction. The measured piezoelectric constant d_{33} of RbBiNb$_2$O$_7$ at room temperature is 5±0.5 pC/N. The thermal depoling results of poled RbBiNb$_2$O$_7$ are shown in Fig. 5.2.11. The d_{33} values were measured at room temperature after annealed at different temperatures for 2 hours. The d_{33} values of RbBiNb$_2$O$_7$ are very stable with increasing temperature. The d_{33} starts to drop when the depoling temperature is close to T_c and tends to zero above T_c.
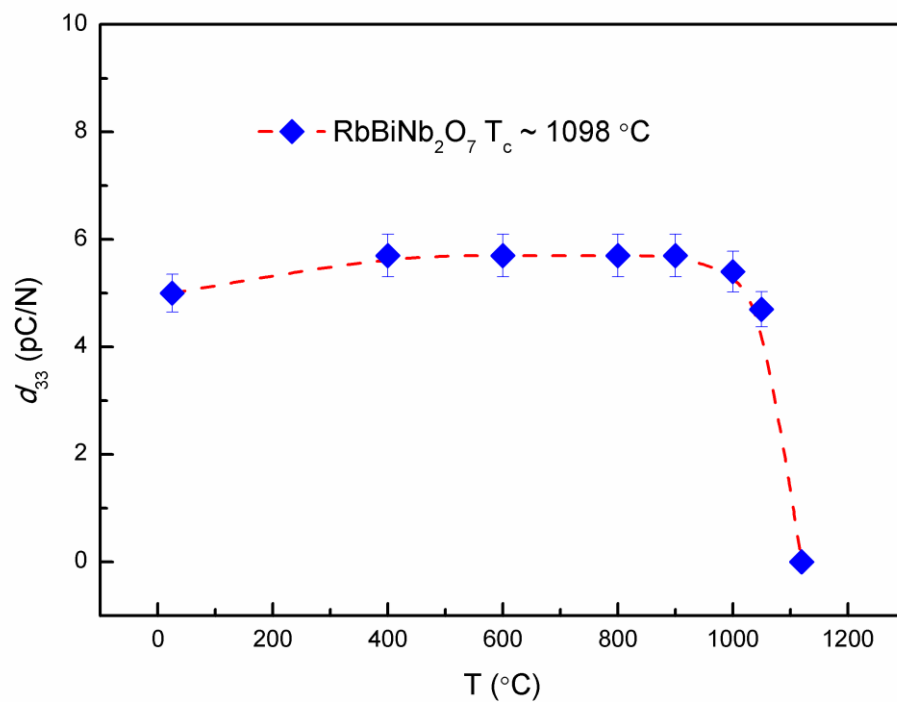
Fig. 5.2.11 Thermal depoling results of poled RbBiNb$_2$O$_7$ ceramic.

5.2.4 Conclusions

2-layer Dion-Jacobson RbBiNb$_2$O$_7$ powders with pure *P2$_1$am* orthorhombic structure were synthesized. RbBiNb$_2$O$_7$ ceramics were prepared by spark plasma sintering with pressure. Strong grain orientation was observed in the ceramics demonstrated by XRD and SEM results. High resolution TEM showed well ordered (0 0 1) lattice planes. The ferroelectricity of RbBiNb$_2$O$_7$ was demonstrated by direct evidence from the ferroelectric domain switching signal in *I-E* loops. Striped ferroelectric domains similar with that in CsBiNb$_2$O$_7$ were observed in RbBiNb$_2$O$_7$ ceramics using PFM. The piezoelectric constant of highly textured RbBiNb$_2$O$_7$ ceramic was approximately 5 pC/N. The Curie point of RbBiNb$_2$O$_7$ was found to be 1098±5 °C by studying the temperature dependence of permittivity and thermal depoling. This result corrects the previous inaccurate T_c result reported by Li, *et al*.

Chapter VI. Results - Hexagonal Compound $Sr_6TiNb_4O_{18}$

6.1 Introduction

A number of the $A_nB_nO_{3n+2}$ type PLS materials have been shown to be ferroelectrics with super high Curie point.[7, 11, 12] The Dion-Jacobson compounds $CsBiNb_2O_7$ and $RbBiNb_2O_7$ have also been demonstrated to be ferroelectrics with high Curie point.[129] No layered perovskite with Hexagonal structure have been reported to be ferroelectric. So far, only two Hexagonal compounds, $Sr_6Nb_4TiO_{18}$ and $La_6Ti_{4.04}Mg_{0.913}O_{18}$, have been reported to be non-centrosymmetric and have the potential to present ferroelectricity.[9] The structure of 6-layer Hexagonal compounds $Sr_6Nb_4TiO_{18}$ was indicated to be non-centrosymmetric space group *R3m* by Drew *et al*. in 1997.[67]

In this work, we prepared the $Sr_6Nb_4TiO_{18}$ ceramics by SSR and SPS method. Microstructures and electrical properties of untextured and textured $Sr_6Nb_4TiO_{18}$ ceramics were studied.

6.2 Experimental Procedure

The $Sr_6Nb_4TiO_{18}$ powders were prepared by SSR method. The starting materials were Sr_2CO_3, Nb_2O_5 and TiO_2. Stoichiometric mixtures of the oxides were ball milled with ethanol at 350 rpm for 3 h. The dried mixtures were first calcined at 1400 °C for 4 h using a conventional furnace. The calcined powders were then re-ball-milled at 350 rpm for 4h and then calcined again at 1400 °C for 4 h to improve the phase impurity.

The calcined powders were sintered using SPS. A heating rate of 100 °C /min was used in all cases. The $Sr_6Nb_4TiO_{18}$ powders were sintered in a 20 mm diameter graphite die for 3 min at 1400 °C, under a pressure of 80 MPa in the SPS furnace. The textured ceramics were prepared using a two-step SPS process.[7, 12, 13] In the first step, the powders prepared by SSR were sintered in a 20 mm diameter graphite die for 3 min under a pressure of 80 MPa at 1300 °C. In the second step, the sintered ceramics were placed in a 30 mm diameter graphite die and sintered for 5 min under a pressure of 80 MPa at 1450 °C. Finally, the sintered ceramics were annealed in air at 1200 °C for 15 h to remove any carbon contamination and reduction produced by SPS.

6.3 Results and Discussion

The XRD pattern of $Sr_6Nb_4TiO_{18}$ powders calcined at 1400 ℃ is shown in Fig. 6.1 C1. Obvious impurities peaks are indexed to be $Sr_5Nb_4O_{15}$ and $SrTiO_3$. To improve the phase purity of the $Sr_6Nb_4TiO_{18}$ powders, the calcined $Sr_6Nb_4TiO_{18}$ powders were re-ball-milled and calcined at 1400 ℃ for several cycles (C2-C5), and their XRD patterns are shown in Fig. 1. The impurities are almost removed in C2. No obvious changes can be observed from C3 to C5. Consequently, $Sr_6Nb_4TiO_{18}$ powders prepared by C3 route were used to prepare ceramics.
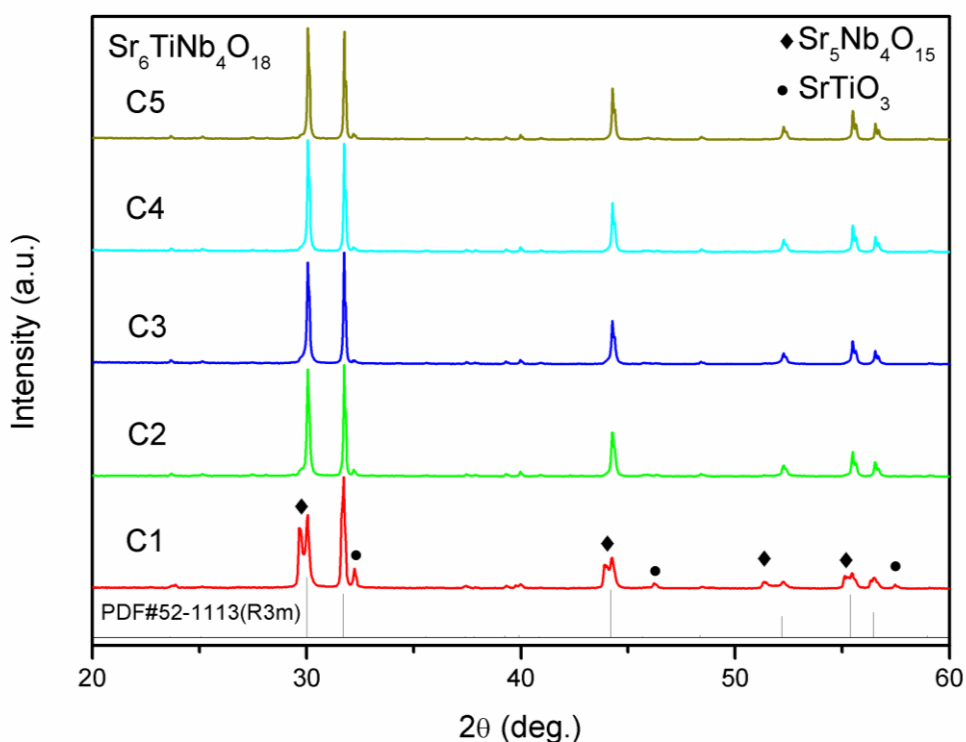
Fig. 6.1 XRD patterns of $Sr_6Nb_4TiO_{18}$ powders calcined at 1400 ℃ for different cycles.

Fig. 6.2 shows the XRD patterns of $Sr_6Nb_4TiO_{18}$ ceramic sintered by SPS at 1400 ℃. No obvious impurities are observed and there is a small (110) orientation. The ceramic XRD pattern was tested along the surface perpendicular to the SPS pressing direction.
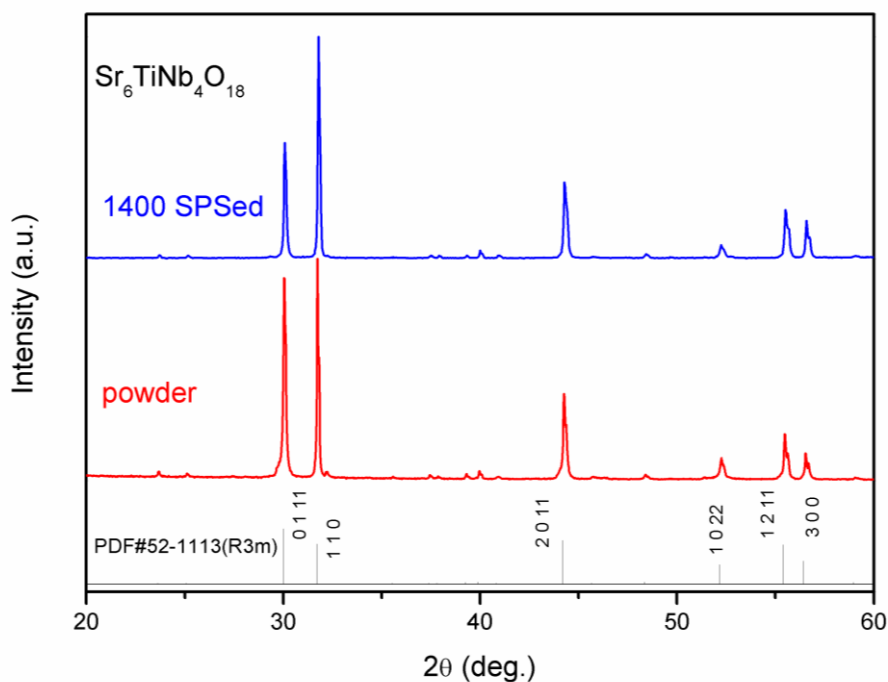
Fig. 6.2 XRD patterns of $Sr_6Nb_4TiO_{18}$ ceramics sintered by SPS at 1400 ℃.

Fig. 6.3(a) shows the SEM images of $Sr_6Nb_4TiO_{18}$ powders. The powders have a plate-like grain shape, which is similar to other PLS materials.[129, 130] Fig. 6.3(b) shows the thermal-etched surface of $Sr_6Nb_4TiO_{18}$ ceramic from the surface with normal parallel to the SPS pressing direction. The grains maintain the plate-like shape of the powders, and some grain orientation can be observed, which is caused by the high pressure during the SPS process. This is consistent with the XRD results from Fig. 6.2.
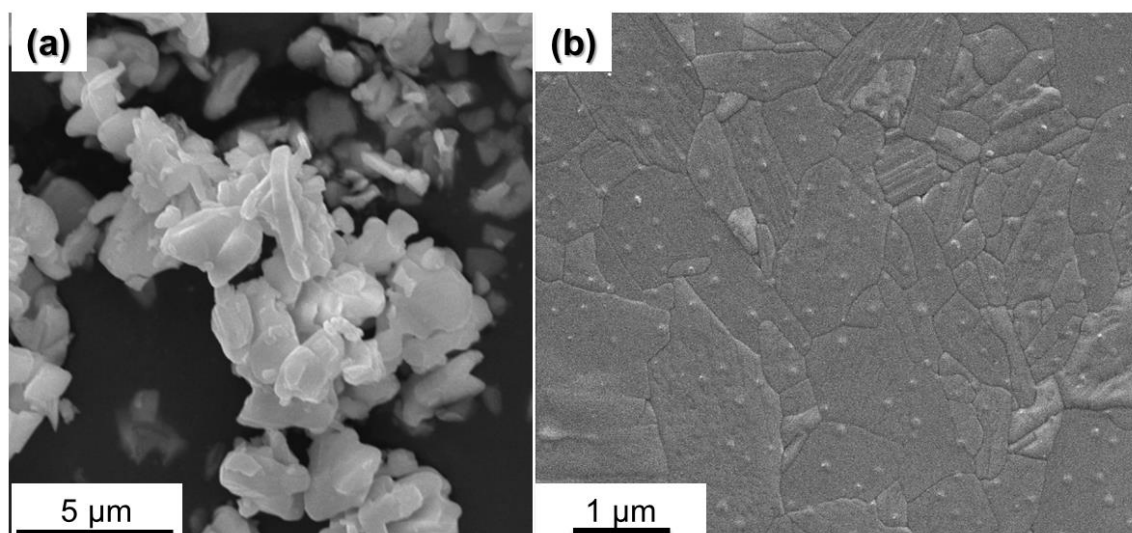
Fig. 6.3 SEM images: (a) $Sr_6Nb_4TiO_{18}$ powders; (b) $Sr_6Nb_4TiO_{18}$ ceramics from the surface

parallel to the SPS pressing direction.

Fig. 6.4 shows the frequency dependence of dielectric permittivity and loss of $Sr_6Nb_4TiO_{18}$ ceramic. The $Sr_6Nb_4TiO_{18}$ ceramic shows very stable permittivity of about 47 in the frequency range from 10^3 to 10^7 Hz. $Sr_6Nb_4TiO_{18}$ ceramic shows low loss (10^3 to 10^7 Hz) like other PLS materials.[12, 95, 130] Fig. 6.5 show the temperature dependence of the dielectric permittivity and loss of $Sr_6Nb_4TiO_{18}$ ceramic. The permittivity increases dramatically when the temperature is above 1200 ℃, but no permittivity peaks or abnormal changes indicating a phase transition are observed. Loss peaks are observed when the temperature is above 1200 ℃, which means that there is probably a ferroelectric to paraelectric phase transition above 1500 ℃.
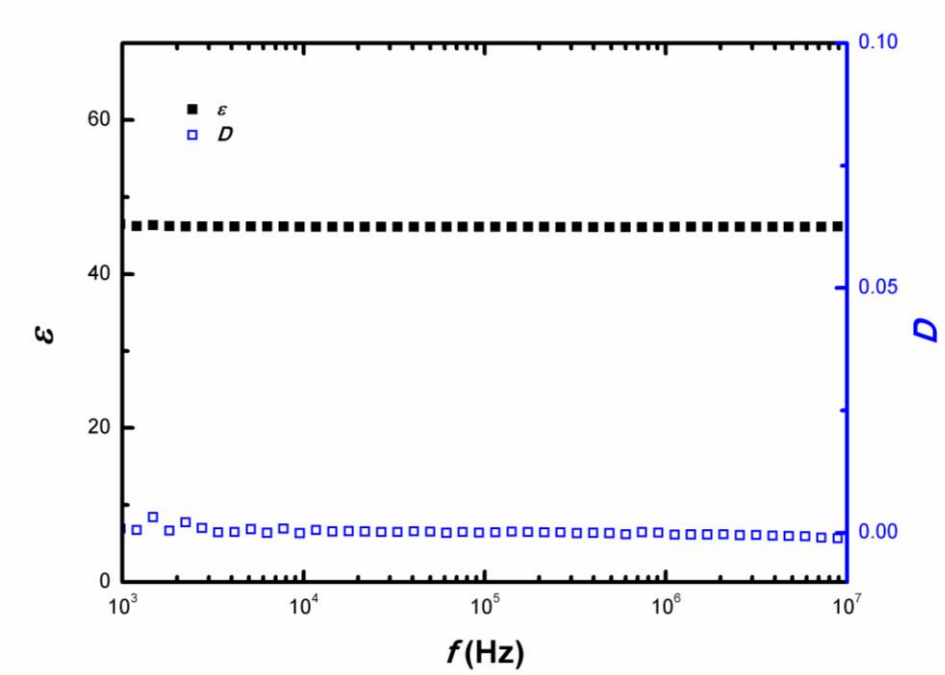
Fig. 6.4 Frequency dependence of permittivity and loss of $Sr_6Nb_4TiO_{18}$ ceramic.
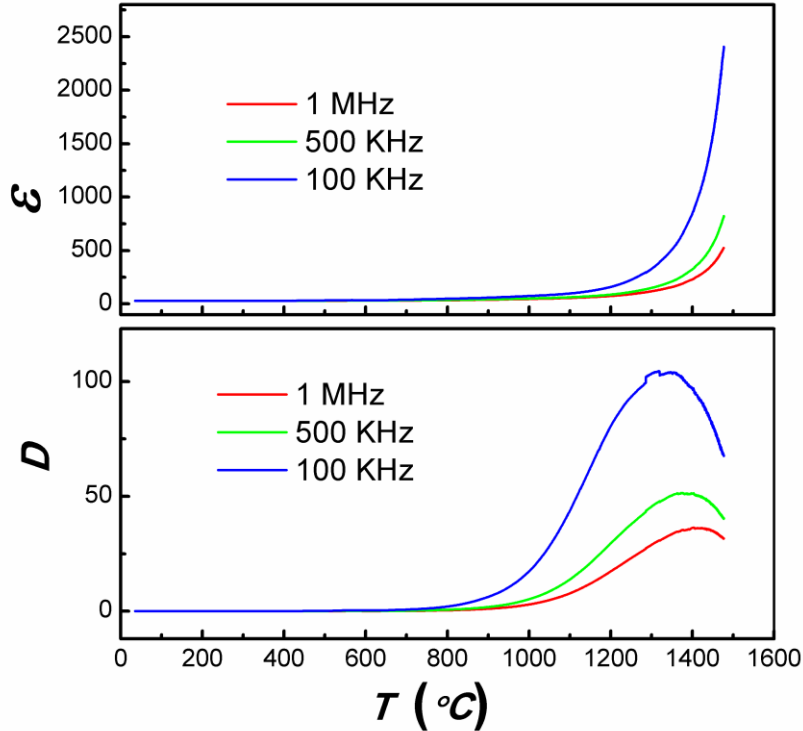
Fig. 6.5 Temperataure dependence of permittivity and loss of $Sr_6Nb_4TiO_{18}$ ceramic.

Fig. 6.6 shows the *I-E* and *P-E* loops of $Sr_6Nb_4TiO_{18}$ ceramic, which were measured at 200 ℃ and 10 Hz. No obvious ferroelectric domain switching is observed when the maximum applied field reaches 300 kV/cm. The *P-E* loop is far less than saturated because of the high coercive field.
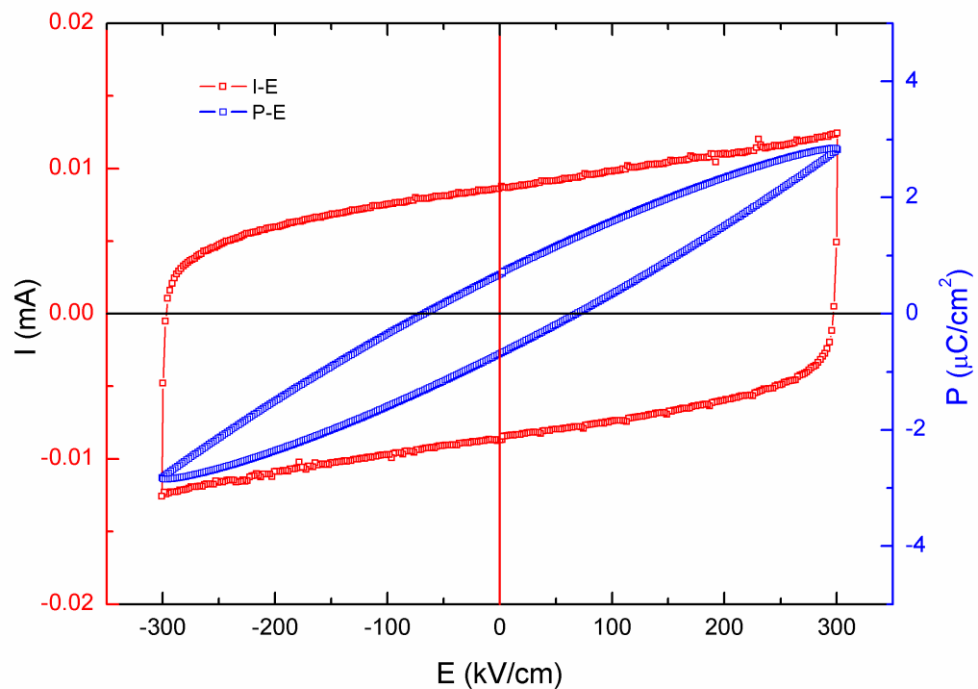
Fig. 6.6 *I-E* and *P-E* loops of $Sr_6Nb_4TiO_{18}$ ceramic measured at 200 ℃ and 10 Hz.

Because $Sr_6Nb_4TiO_{18}$ ceramics have plate-like grains like other PLS compounds, it is possible to texture the ceramics and reduce its coercive field. Fig. 6.7 shows the XRD patterns of textured $Sr_6Nb_4TiO_{18}$ ceramics. The intensity difference between the (0 1 11) and (1 1 0) peaks from the surfaces parallel and perpendicular to the pressing direction clearly show the high preferred grain orientation of the textured $Sr_6Nb_4TiO_{18}$ ceramics. A high orientation of (0 0 l) planes from the surface parallel to the pressing direction is

observed for most of PLS ferroelectrics,[7, 12, 129, 130] but $Sr_6Nb_4TiO_{18}$ ceramics show a high orientation of (0 1 11) planes from the surface parallel to the pressing direction. The spontaneous polarization of $Sr_6Nb_4TiO_{18}$ is along c-axis. It is reasonable to measure the ferroelectricity from the parallel surface, because the angle between (0 0 1) and (0 1 11) planes is very small. Fig. 6.8 shows the SEM images of $Sr_6Nb_4TiO_{18}$ ceramics from the planes parallel and perpendicular to the pressing direction, which also shows that the $Sr_6Nb_4TiO_{18}$ ceramics are highly textured.
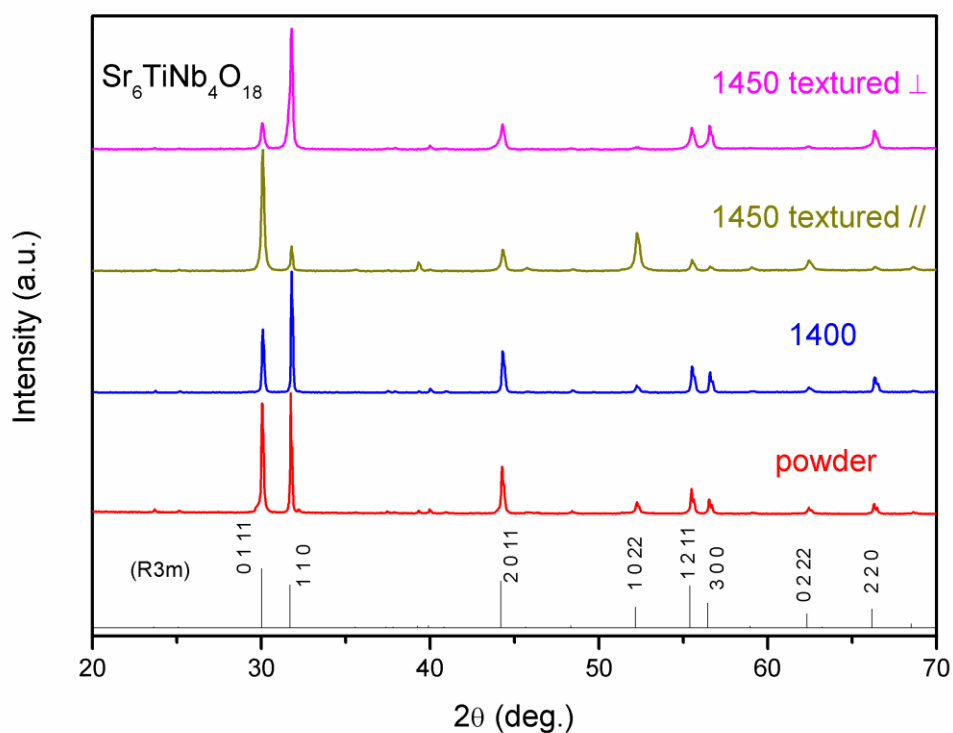
Fig. 6.7 XRD patterns of textured $Sr_6Nb_4TiO_{18}$ ceramics.
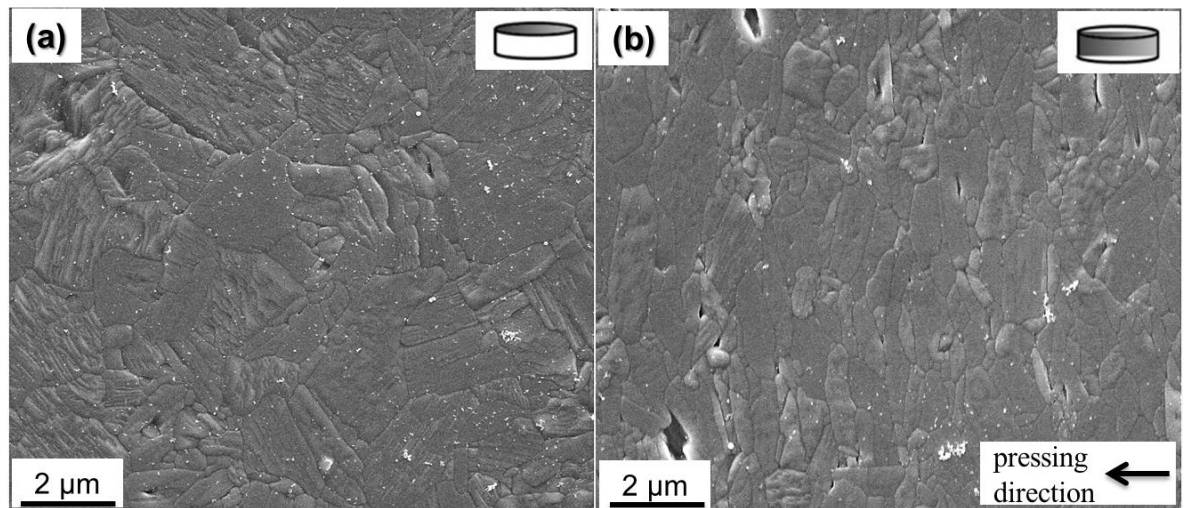
Fig. 6.8 SEM images of textured $Sr_6Nb_4TiO_{18}$ ceramics from the planes parallel (a) and

perpendicular (b) to the pressing direction.

Fig. 6.9 shows the frequency dependence of dielectric permittivity and loss of textured $Sr_6Nb_4TiO_{18}$ ceramic from the planes parallel and perpendicular to the pressing direction. The textured ceramic from both planes show very low losses in the frequency range. Due to the anisotropy of the layered structure, textured ceramics show higher permittivity along the plane perpendicular to the pressing direction and lower permittivity along the plane parallel to the pressing direction than that of the untextured ceramic.
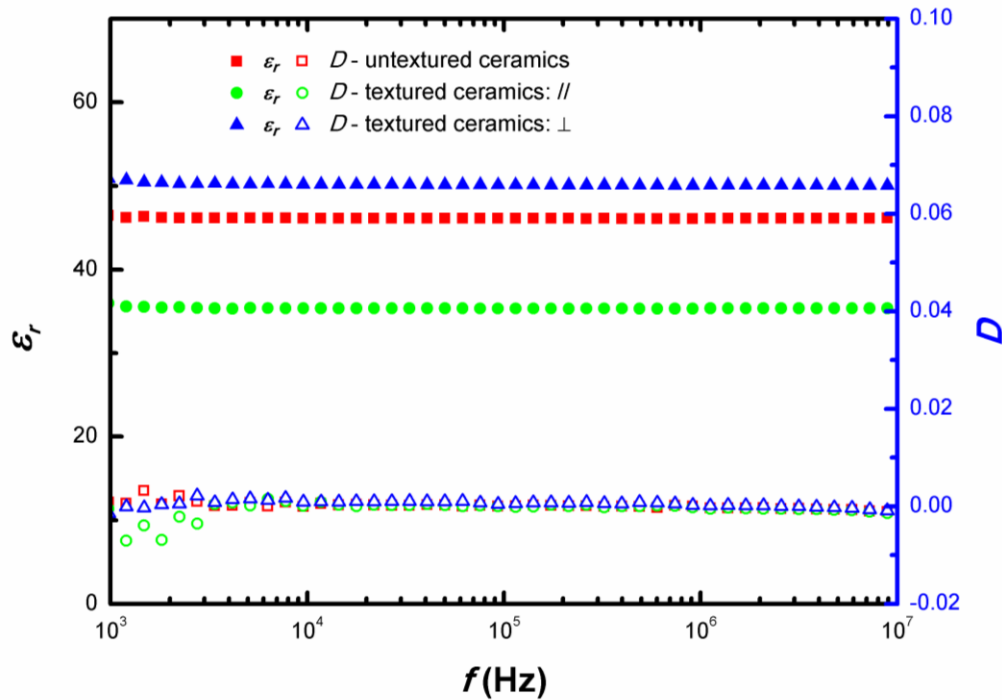
Fig. 6.9 Frequency dependence of permittivity and loss of textured $Sr_6Nb_4TiO_{18}$ ceramic.

Fig. 6.10 shows the *I-E* and *P-E* loops of textured $Sr_6Nb_4TiO_{18}$ ceramic from the plane parallel to the pressing direction measured at 200 ℃ and 10 Hz. No obvious ferroelectric domain switching was observed in the untextured $Sr_6Nb_4TiO_{18}$ ceramic due to its high coercive field. Consequently, the $Sr_6Nb_4TiO_{18}$ ceramic was textured to reduce its coercive field. As discussed before, the spontaneous polarization of $Sr_6Nb_4TiO_{18}$ is along *c*-axis, so the *I-E* and *P-E* loops of textured $Sr_6Nb_4TiO_{18}$ ceramic was measured from the plane parallel to the pressing direction, but still no ferroelectric domain switching is observed when the applied field reaches 300 kV/cm. The samples were poled along the plane parallel to the pressing direction at 200 ℃, but no piezoelectric activity could be detected.
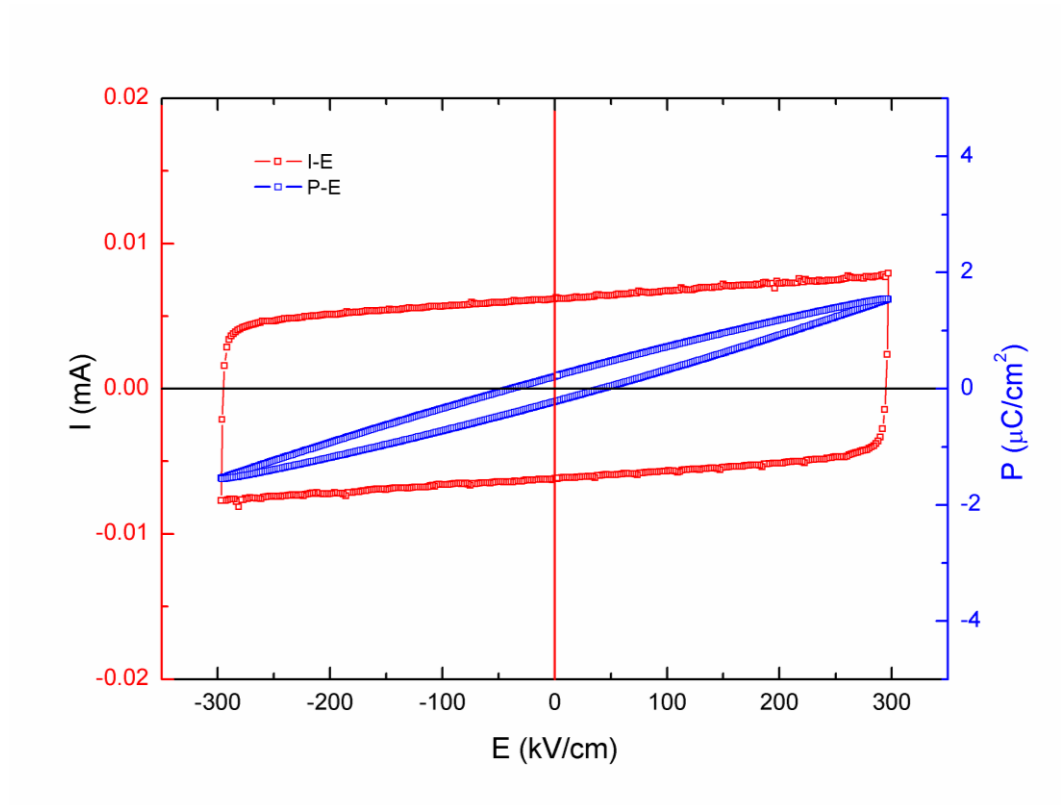
Fig. 6.10 *I-E* and *P-E* loops of textured $Sr_6Nb_4TiO_{18}$ ceramic (//) measured at 200 ℃ and 10 Hz.

6.4 Conclusions

The 6-layer Hexagonal compound $Sr_6Nb_4TiO_{18}$ was prepared by SSR and SPS. Textured $Sr_6Nb_4TiO_{18}$ ceramics were prepared by a 2-step method. High preferred orientation of (0 1 11) planes from the surface parallel to the pressing direction was observed by X-ray diffraction and SEM studies. Like other PLS ferroelectrics, both the untextured and textured ceramics show very low dielectric losses in the frequency range from 10^3 to 10^7 Hz. Anisotropic dielectric permittivity was observed due to the layer structure. The temperature dependence of permittivity and loss suggest that its Curie point is greater than 1500 °C. No ferroelectric properties were observed by studying the *I-E* and *P-E* loops, and no d_{33} was observed after poling.

Chapter VII. Conclusions and Future work

7.1 Conclusions

In this research, the crystallographic structures, microstructures, dielectric, ferroelectric and piezoelectric properties of some perovskite-like layered structured compounds were investigated. $(A_x La_{1-x})Ti_2O_7$ (A = Sm and Eu) solid solutions with 4-layer $A_nB_nO_{3n+2}$ structure were studied to improve the electrical properties of $La_2Ti_2O_7$. $Pr_3Ti_2TaO_{11}$ with 3-layer $A_nB_nO_{3n+2}$ structure and $LaTaO_4$ with 2-layer $A_nB_nO_{3n+2}$ structure were studied to investigate the ferroelectric properties of $A_nB_nO_{3n+2}$ compounds with different perovskite layers. To extend the study of ferroelectric properties on other PLS materials, $ABiNb_2O_7$ (A = Rb and Cs) with Dion-Jacobson structure and $Sr_6TiNb_4O_{18}$ with Hexagonal structure were also studied.

7.1.1 $A_nB_nO_{3n+2}$ Compounds

$(A_x La_{1-x})Ti_2O_7$ (A = Sm and Eu) solid solutions were isomorphous with $La_2Ti_2O_7$ when x was less than 0.5 for $(Eu_x La_{1-x})Ti_2O_7$ and 0.8 for $(Sm_x La_{1-x})Ti_2O_7$. When x was above their solubility limit, a biphase was observed. The XRD and Raman data suggested that the biphase consisted of $(A_x La_{1-x})_2Ti_2O_7$ perovskite-like layered structure and pure $Sm_2Ti_2O_7$ pyrochlore structure. Ferroelectric domain switching was observed in the *I-E* and *P-E* hysteresis loops of textured $(Sm_x La_{1-x})Ti_2O_7$ ($x < 0.2$) ceramics. The highest d_{33} was 2.8 pC/N for $(Sm_{0.1}La_{0.9})Ti_2O_7$.

The $Pr_3Ti_2TaO_{11}$ compound has a 3-layer type II perovskite-like layered structure with space group *Pmc2$_1$*. High resolution TEM images show that the ceramics were highly disordered with faulting in the layer structure of the $n = 3$ type II phase and coexistence of a $n = 4$ phase intergrowths on a fine scale (nm). The Curie point of $Pr_3Ti_2TaO_{11}$ ceramic was indicated to be 1415±5 °C. The disordered structure made it difficult to

ferroelectrically switch and pole the samples. However, by using an electric field of 100 to 200 V/cm at 900 °C it was possible to demonstrate a small piezoelectric activity with d_{33} between 0.1 to 0.2 pC/N.

Pure LaTaO$_4$ powders with orthorhombic phase were be prepared by co-precipitation synthesis. The O-LaTaO$_4$ powders have a 2-layer perovskite-like layered structure with space group $A2_1am$. The single phase O-LaTaO$_4$ ceramic was prepared using SPS with a slow cooling rate (20 °C/min). An irreversible phase transition was detected by studying the temperature dependence of dielectric permittivity and loss, and the O-LaTaO$_4$ ceramic transferred into a biphase structure dominated by monoclinic phase after the T_c measurement. The M-LaTaO$_4$ ceramic can transform into orthorhombic phase under high DC electric field. A d_{33} of 0.3 pC/N was obtained from the electric field induced orthorhombic phase.

7.1.2 Dion-Jacobson Compounds

Highly textured 2-layer Dion-Jacobson ceramics ABiNb$_2$O$_7$ (A = Rb and Cs) were prepared by one-step SPS. High resolution TEM showed well ordered (0 0 1) lattice planes. Striped ferroelectric domains were observed using PFM. The ferroelectricity and piezoelectricity of CsBiNb$_2$O$_7$ has been demonstrated for the first time. The T_c of RbBiNb$_2$O$_7$ and CsBiNb$_2$O$_7$ are 1098±5 and 1033±5 °C, respectively. The piezoelectric constant of RbBiNb$_2$O$_7$ and CsBiNb$_2$O$_7$ were approximately 5 and 8 pC/N. Thermal depoling studies confirmed the Curie point and the stability of the piezoelectricity.

7.1.3 Hexagonal Compounds

Textured Sr$_6$Nb$_4$TiO$_{18}$ ceramics were prepared by a 2-step method. There was high preferred orientation of the (0 1 11) plane from the surface parallel to the pressing direction. Like other PLS ferroelectrics, both the untextured and textured ceramics show

very low dielectric losses in the frequency range from 10^3 to 10^7 Hz. Anisotropic dielectric permittivity was observed due to its layer structure. Through the study on its temperature dependence of permittivity and loss, its Curie point was found to be greater than 1500 ℃. No ferroelectric properties were observed by studying of *I-E* and *P-E* loops, and no d_{33} was observed after poling.

In summary, the piezoelectric constant of $La_2Ti_2O_7$ was improved from 1.6 to 2.8 pC/N by doping Sm. The crystallographic structure of $(Eu_{1-x}La_x)_2Ti_2O_7$ and $(Sm_{1-x}La_x)_2Ti_2O_7$ solid solutions were well studied. The $Pr_3Ti_2TaO_{11}$ compound was demonstrated to have a 3-layer type II $A_nB_nO_{3n+2}$ PLS structure, and its ferroelectric properties were investigated. In the second part of this work, the ferroelectricity and piezoelectricity of $CsBiNb_2O_7$ with Dion-Jacobson type PLS structure was successfully demonstrated for the first time. The ferroelectricity and piezoelectricity of $RbBiNb_2O_7$, which have similar structure with $CsBiNb_2O_7$, were also fully studied. In the last part, $Sr_6Nb_4TiO_{18}$ ceramics with non-centrosymmetric structure were successfully prepared, but no obvious evidence was found to prove its ferroelectricity.

7.2 Future Work

7.2.1 Further Study on Dion-Jacobson Materials

The Dion-Jacobson materials have been studied for a long time, but the ferroelectricity of Dion-Jacobson materials was firstly discussed in detail in the 2-layer DJ compounds ABiNb$_2$O$_7$ (A = Rb and Cs) in this research. Consequently, it leads to a further interest to study the ferroelectricity of other DJ compounds. CsLaNb$_2$O$_7$, RbLaNb$_2$O$_7$ and RbNdNb$_2$O$_7$ have been reported to have polar structure below room temperature in a recent report.[60] During this work, RbBiNb$_2$O$_7$ was also observed to have a phase transition below room temperature (25 ℃). Therefore, the phase structure and ferroelectricity of DJ compounds below room temperature should be investigated.

Compared with A_2B_2O$_7$ compounds, most of the DJ compounds including ABiNb$_2$O$_7$ (A = Rb and Cs) show obvious leakage and proton conductivity, which always makes the study of ferroelectricity difficult. Impedance spectroscopy is a useful tool to study the electrical conductivity of DJ compounds. Low temperature I-E and P-E measurements can be applied to reduce the effects from current leakage.

7.2.2 PFM Study on A_2B_2O$_7$ Compounds

In the study of ABiNb$_2$O$_7$ (A = Rb and Cs) DJ compounds, PFM was used to observe the ferroelectric domain structures. Clear and unique stripe ferroelectric domains were observed in the PFM images. The ferroelectricity of 4-layer A_2B_2O$_7$ compounds, like La$_2$Ti$_2$O$_7$ and Sr$_2$Nb$_2$O$_7$, have been well studied in our previous work, but their ferroelectric domain structures have not been observed. TEM was used to study ferroelectric domain structures, but no evidence of domains was found. Consequently, PMF should be used to study the ferroelectric domain structures of La$_2$Ti$_2$O$_7$ and Sr$_2$Nb$_2$O$_7$.

7.2.3 High Pressure Study on (A_xLa$_{1-x}$)Ti$_2$O$_7$ Solid Solutions

In this research, XRD and Raman spectroscopy have been used to study the phase structure of (A_xLa$_{1-x}$)Ti$_2$O$_7$ solid solutions. When x was above their solubility limit, a biphase which consists of PLS and pyrochlore structure was observed. As reported, Sm$_2$Ti$_2$O$_7$ and Eu$_2$Ti$_2$O$_7$ with pyrochlore structure can be transformed into PLS under very high pressure (>10 GPa). Therefore, high pressure can be used to extend the range of PLS phase in (A_xLa$_{1-x}$)Ti$_2$O$_7$ solid solutions. High pressure Raman is another way to study the phase transition process from pyrochlore to PLS in (A_xLa$_{1-x}$)Ti$_2$O$_7$ solid solutions.

7.2.4 Further Study on Hexagonal Materials

There is one disadvantage of $A_2B_2O_7$ and DJ ferroelectrics, the distortion of their spontaneous polarization is along the *a-* or *b-*axis, supposing that the *c-*axis is the longest axis and perpendicular to the perovskite layers. This means that the P_s direction always shows lower electrical resistivity than the *c* direction due to the anisotropy of the layer structure. The Hexagonal compound Sr$_6$Nb$_4$TiO$_{18}$ has a polar structure *R3m* which has a spontaneous polarization along the *c-*axis, which should have a higher resistivity. In this work, ceramics of the hexagonal compound Sr$_6$Nb$_4$TiO$_{18}$ with polar structure *R3m* was prepared, but no obvious ferroelectricity was observed. To further study its ferroelectricity, high temperature poling can be used. The ferroelectric properties of other hexagonal compound with polar structure, La$_6$Ti$_{4.04}$Mg$_{0.913}$O$_{18}$, should also be studied on its ferroelectricity.

List of Publications

1. **Chen, C.**, Jiang, Q., Wei, X., Abrahams, I., Yan, H. and Reece, M. J., *Journal of the American Ceramic Society*, 2014, **97**, 3624-3630.

2. **Chen, C.**, Ning, H., Lepadatu, S., Cain, M., Yan, H. and Reece, M. J., *J. Mater. Chem. C*, 2015, **3**, 19-22.

3. **Chen, C.**, Gao, Z., Yan, H. and Reece, M. J., *Journal of the American Ceramic Society*. (Under review)

4. Gao, Z., Ning, H., **Chen, C.**, Wilson, R., Shi, B., Ye, H., Yan, H. and Reece, M. J., *Journal of the American Ceramic Society*, 2012, 1163-1170.

Reference

1. Anton, S. R. and Sodano, H. A., *Smart Materials and Structures*, 2007, 16, R1.

2. Saito, Y., Takao, H., Tani, T., Nonoyama, T., Takatori, K., Homma, T., Nagaya, T. and Nakamura, M., *Nature*, 2004, 432, 84-87.

3. Zylberberg, J., A. Belik, A., Takayama-Muromachi, E. and Ye, Z.-G., *Chemistry of Materials*, 2007, 19, 6385-6390.

4. Takenaka, T. and Nagata, H., *Journal of the European Ceramic Society*, 2005, 25, 2693-2700.

5. Zhang, S. and Yu, F., *Journal of the American Ceramic Society*, 2011, 94, 3153-3170.

6. Damjanovic, D., Muralt, P. and Setter, N., *Sensors Journal, IEEE*, 2001, 1, 191-206.

7. Yan, H., Ning, H., Kan, Y., Wang, P. and Reece, M. J., *Journal of the American Ceramic Society*, 2009, 92, 2270-2275.

8. Lichtenberg, F., Herrnberger, A., Wiedenmann, K. and Mannhart, J., *Progress in Solid State Chemistry*, 2001, 29, 1-70.

9. Lichtenberg, F., Herrnberger, A. and Wiedenmann, K., *Progress in Solid State Chemistry*, 2008, 36, 253-387.

10. Nanamatsu, S., Kimura, M. and Kawamura, T., *J. Phys. Soc. Jpn.*, 1975, 38, 817-824.

11. Nanamatsu, S., Kimura, M., Doi, K., Matsushita, S. and Yamada, N., *Ferroelectrics*, 1974, 8, 511-513.

12. Ning, H., Yan, H. and Reece, M. J., *Journal of the American Ceramic Society*, 2010, 93, 1409-1413.

13. Yan, H. X., Ning, H. P., Zhang, H. T. and Reece, M. J., *Advances in Applied Ceramics*, 2010, 109, 139-142.

14. Levin, I. and Bendersky, L. A., *Acta Crystallographica Section B*, 1999, 55, 853-866.

15. Titov, Y. A., Sych, A. M., Kapshuk, A. A. and Yashchuk, V. P., *Inorganic Materials*, 2001, 37, 294-297.

16. Titov, Y. A., Sych, A. M., Markiv, V. Y., Belyavina, N. M., Kapshuk, A. A. and Yaschuk, V. P., *Journal of Alloys and Compounds*, 2001, 316, 309-315.

17. Titov, Y. A., Sych, A. M., Markiv, V. Y., Belyavina, N. M., Kapshuk, A. A., Yaschuk, V. P. and Slobodyanik, M. S., *Journal of Alloys and Compounds*, 2002, 337, 89-93.

18. Damjanovic, D., *Reports on Progress in Physics*, 1998, 61, 1267.

19. Haertling, G. H., *Journal of the American Ceramic Society*, 1999, 82, 797-818.

20. Kong, L. B., Zhang, T. S., Ma, J. and Boey, F., *Progress in Materials Science*, 2008, 53, 207-322.

21. Valasek, J., *Physical Review*, 1921, 17, 475-481.

22. Scott, J. F., *Science*, 2007, 315, 954-959.

23. Rödel, J., Jo, W., Seifert, K. T. P., Anton, E.-M., Granzow, T. and Damjanovic, D., *Journal of the American Ceramic Society*, 2009, 92, 1153-1177.

24. Bell, A. J., *Journal of the European Ceramic Society*, 2008, 28, 1307-1317.

25. Nyman, M., Rodriguez, M. A., Rohwer, L. E. S., Martin, J. E., Waller, M. and Osterloh, F. E., *Chemistry of Materials*, 2009, 21, 4731-4737.

26. Cahill, D. G., Melville, A., Schlom, D. G. and Zurbuchen, M. A., *Applied Physics Letters*, 2010, 96, 121903.

27. Ukita, T., Hirose, Y., Ohno, S., Hatabayashi, K., Fukumura, T. and Hasegawa, T., *J. Appl. Phys.*, 2012, 111, 07D909.

28. Nanamats.S and Kimura, M., *J. Phys. Soc. Jpn.*, 1974, 36, 1495-1495.

29. Drews, A. R., WongNg, W., Vanderah, T. A. and Roth, R. S., *Journal of Alloys and Compounds*, 1997, 255, 243-247.

30. Dion, M., Ganne, M. and Tournoux, M., *Revue De Chimie Minerale*, 1986, 23, 61-69.

31. Cava, R. J. and Roth, R. S., *J Solid State Chem*, 1981, 36, 139-147.

32. Titov, Y. A., Sych, A. M. and Kapshuk, A. A., *Inorganic Materials*, 1998, 34, 496-498.

33. Drews, A. R., Wong-Ng, W., Roth, R. S. and Vanderah, T. A., *Materials Research Bulletin*, 1996, 31, 153-162.

34. Levin, I., Bendersky, L. A., Vanderah, T. A., Roth, R. S. and Stafsudd, O. M., *Materials Research Bulletin*, 1998, 33, 501-517.

35. Bruyer, E. and Sayede, A., *J. Appl. Phys.*, 2010, 108.

36. Gao, Z. P., Yan, H. X., Ning, H. P. and Reece, M. J., *Advances in Applied Ceramics*, 2012.

37. Zhang, F. X., Manoun, B., Saxena, S. K. and Zha, C. S., *Applied Physics Letters*, 2005, 86, 181906.

38. Porotnikov, N. V. and Bazuev, G. V., *Russian Journal of Inorganic Chemistry*, 1989, 34, 142-143.

39. Sych, A. M., Stefanovich, S. Y., Titov, Y. A., Bondarenko, T. N. and Melnik, V. M., *Inorganic Materials*, 1991, 27, 2229-2230.

40. Dasgupta, P., Jana, Y. M., Nag Chattopadhyay, A., Higashinaka, R., Maeno, Y. and Ghosh, D., *Journal of Physics and Chemistry of Solids*, 2007, 68, 347-354.

41. Kimura, M., Nanamatsu, S., Doi, K., Matsushita, S. and Takahashi, M., *Japanese Journal of Applied Physics*, 1972, 11, 904.

42. Ishizawa, N., Marumo, F., Iwai, S., Kimura, M. and Kawamura, T., *Acta Crystallographica Section B*, 1982, 38, 368-372.

43. Zhang, F. X., Lian, J., Becker, U., Ewing, R. C., Wang, L. M., Hu, J. and Saxena, S. K., *J Solid State Chem*, 2007, 180, 571-576.

44. López-Pérez, J. and Íñiguez, J., *Phys Rev B*, 2011, 84, 075121.

45. Messing, G. L., Trolier-McKinstry, S., Sabolsky, E. M., Duran, C., Kwon, S., Brahmaroutu, B., Park, P., Yilmaz, H., Rehrig, P. W., Eitel, K. B., Suvaci, E., Seabaugh, M. and Oh, K. S., *Crit. Rev. Solid State Mat. Sci.*, 2004, 29, 45-96.

46. Ali, C., *Materials Research Bulletin*, 2008, 43, 1623-1629.

47. Chen, G., Fu, C. L., Peng, X. D., Ran, S. N., Cai, W. and Deng, X. L., *Integr. Ferroelectr.*, 2013, 141, 45-49.

48. Shao, Z., Saitzek, S., Blach, J.-F., Sayede, A., Roussel, P. and Desfeux, R., *European Journal of Inorganic Chemistry*, 2011, 2011, 3569-3576.

49. BONDARENKO, T. N., UVAROV, V. N., BORISENKO, S. V., TETERIN, Y. A., DZEGANOVSKI, V. P., Sych, A. M. and TITIVE, Y. A., *Journal of the Korean Physical Society*, 1998, 32, 65-67.

50. Henderson, N. L., Baek, J., Halasyamani, P. S. and Schaak, R. E., *Chemistry of Materials*, 2007, 19, 1883-1885.

51. Li, C. and Wei, X., *Journal of Materials Science*, 2012, 47, 4200-4204.

52. Li, C., Wei, X., Yan, H. and Reece, M. J., *Journal of the European Ceramic Society*, 2012, 32, 4015-4020.

53. Titov, Y. A., Sych, A. M., Sokolov, A. N., Kapshuk, A. A. and Yashchuk, V. P., *Inorganic Materials*, 2000, 36, 625-628.

54. Titov, Y. A., Sych, A. M., Sokolov, A. N., Markiv, V. Y., Belyavina, N. M. and Kapshuk, A. A., *High Pressure Res*, 2001, 21, 175-181.

55. Jian, L. and Wayman, C. M., *Journal of the American Ceramic Society*, 1997, 80, 803-806.

56. Santoro, A., Marezio, M., Roth, R. S. and Minor, D., *J Solid State Chem*, 1980, 35, 167-175.

57. Titov, Y. A., Sych, A. M., Sokolov, A. N., Kapshuk, A. A., Markiv, V. Y. and Belyavina, N. M., *Journal of Alloys and Compounds*, 2000, 311, 252-255.

58. Vullum, F., Nitsche, F., Selbach, S. M. and Grande, T., *J Solid State Chem*, 2008, 181, 2580-2585.

59. Gasparotto, G., Nascimento, N. M., Cebim, M. A., Varela, J. A. and Zaghete, M. A., *Journal of Alloys and Compounds*, 2011, 509, 9076-9078.

60. Benedek, N. A., *Inorganic Chemistry*, 2014, 53, 3769-3777.

61. Subramanian, M. A., Gopalakrishnan, J. and Sleight, A. W., *Materials Research Bulletin*, 1988, 23, 837-842.

62. Snedden, A., Knight, K. S. and Lightfoot, P., *J Solid State Chem*, 2003, 173, 309-313.

63. Fennie, C. J. and Rabe, K. M., *Applied Physics Letters*, 2006, 88, 262902.

64. Li, B.-W., Osada, M., Ozawa, T. C. and Sasaki, T., *Chemistry of Materials*, 2012, 24, 3111-3113.

65. Kako, T. and Ye, J. H., *Mater. Trans.*, 2005, 46, 2694-2698.

66. Goff, R. J., Keeble, D., Thomas, P. A., Ritter, C., Morrison, F. D. and Lightfoot, P., *Chemistry of Materials*, 2009, 21, 1296-1302.

67. Drews, A. R., Wong-Ng, W., Vanderah, T. A. and Roth, R. S., *Journal of Alloys and Compounds*, 1997, 255, 243-247.

68. Vanderah, T. A., Miller, V. L., Levin, I., Bell, S. M. and Negas, T., *J Solid State Chem*, 2004, 177, 2023-2038.

69. Rahaman, M. N., *Ceramic Processing and Sintering*, CRC Press, USA, 2003.

70. Gaikwad, S. P., Dhesphande, S. B., Khollam, Y. B., Samuel, V. and Ravi, V., *Materials Letters*, 2004, 58, 3474-3476.

71. Gupta, U. N., Pradhan, S., Muthurajan, H., Kumar, H. H., Kharat, D. K. and Ravi, V., *Journal of the American Ceramic Society*, 2007, 90, 2661-2663.

72. Dimitriev, Y., Ivanova, Y. and Iordanova, R., *journal of the University fo CHemical Technology and Metallurgy*, 2008, 43, 181-192.

73. Andrianov, N. T., *Glass and Ceramics*, 2003, 60, 320-325.

74. Hench, L. L. and West, J. K., *Chemical Reviews*, 1990, 90, 33-72.

75. Guillon, O., Gonzalez-Julian, J., Dargatz, B., Kessel, T., Schierning, G., Räthel, J. and Herrmann, M., *Adv. Eng. Mater.*, 2014, 830-849.

76. Munir, Z. A., Quach, D. V. and Ohyanagi, M., *Journal of the American Ceramic Society*, 2011, 94, 1-19.

77. Garay, J. E., *Annual Review of Materials Research*, 2010, 40, 445-468.

78. Hulbert, D. M., Anders, A., Dudina, D. V., Andersson, J., Jiang, D., Unuvar, C., Anselmi-Tamburini, U., Lavernia, E. J. and Mukherjee, A. K., *J. Appl. Phys.*, 2008, 104, 033305.

79. Hulbert, D. M., Anders, A., Andersson, J., Lavernia, E. J. and Mukherjee, A. K., *Scripta Materialia*, 2009, 60, 835-838.

80. Munir, Z., Anselmi-Tamburini, U. and Ohyanagi, M., *Journal of Materials Science*, 2006, 41, 763-777.

81. Kan, Y., Wang, P., Li, Y., Cheng, Y.-B. and Yan, D., *Materials Letters*, 2002, 56, 910-914.

82. German, R. M., in *Sintering: from Empirical Observations to Scientific Principles*, ed. R. M. German, Butterworth-Heinemann, Boston, 2014, pp. 71-130.

83. Louër, D., in *Encyclopedia of Spectroscopy and Spectrometry (Second Edition)*, ed. J. C. Lindon, Academic Press, Oxford, 1999, pp. 2253-2262.

84. Larson, A. C. and Dreele, R. B. V., *Los Alamos National Laboratory Report LAUR*, 1994, 86-748.

85. Toby, B. H., *J. Appl. Cryst*, 2001, 34, 210-213.

86. Lotgering, F. K., *Journal of Inorganic and Nuclear Chemistry*, 1959, 9, 113-123.

87. Smith, K. L., Blackford, M. G., Lumpkin, G. R., Whittle, K. and Zaluzec, N. J., *Microscopy and Microanalysis*, 2006, 12, 1094.

88. Shannon, R., *Acta Crystallographica Section A*, 1976, 32, 751-767.

89. Gupta, H. C., Brown, S., Rani, N. and Gohel, V. B., *Journal of Raman Spectroscopy*, 2001, 32, 41-44.

90. Krishnankutty, K. and Dayas, K. R., *Bull Mater Sci*, 2008, 31, 907-918.

91. Liang, K., Qi, Y. and Lu, C., *Journal of Raman Spectroscopy*, 2009, 40, 2088-2091.

92. Long, C., Fan, H. and Ren, P., *Inorganic Chemistry*, 2013, 52, 5045-5054.

93. Das, R. R., Pérez, W., Katiyar, R. S. and Bhalla, A. S., *Journal of Raman Spectroscopy*, 2002, 33, 219-222.

94. Gao, Z. P., Yan, H. X., Ning, H. P., Wilson, R., Wei, X. Y., Shi, B., Ye, H. and Reece, M. J., *Journal of the European Ceramic Society*, 2013, 33, 1001-1008.

95. Gao, Z., Ning, H., Chen, C., Wilson, R., Shi, B., Ye, H., Yan, H. and Reece, M. J., *Journal of the American Ceramic Society*, 2012, n/a-n/a.

96. Härdtl, K. H., *Ceramics International*, 1982, 8, 121-127.

97. Yan, H., Zhang, H., Ubic, R., Reece, M. J., Liu, J., Shen, Z. and Zhang, Z., *Advanced Materials*, 2005, 17, 1261-1265.

98. Cai, L., Arias, A. L. and Nino, J. C., *Journal of Materials Chemistry*, 2011, 21, 3611-3618.

99.   Suarez, D. Y., Reaney, I. M. and Lee, W. E., *J. Mater. Res.*, 2001, 16, 3139-3149.

100.   Titov, Y. A., Slobodyanik, N. S. and Chumak, V. V., *Theor Exp Chem*, 2006, 42, 102-105.

101.   Zhang, H., Yan, H. and Reece, M. J., *J. Appl. Phys.*, 2010, 108, 014109.

102.   Maso, N., Woodward, D. I., Thomas, P. A., Varez, A. and West, A. R., *Journal of Materials Chemistry*, 2011, 21, 2715-2722.

103.   Maso, N., Woodward, D. I., Varez, A. and West, A. R., *Journal of Materials Chemistry*, 2011, 21, 12096-12102.

104.   Yadav, T. K., Singh, A. K., Kumar, K. and Yadav, R. A., *Optical Materials*, 2011, 33, 1732-1736.

105.   Atuchin, V. V., Grivel, J. C., Korotkov, A. S. and Zhang, Z., *J Solid State Chem*, 2008, 181, 1285-1291.

106.   Atuchin, V. V., Gavrilova, T. A., Grivel, J.-C. and Kesler, V. G., *Journal of Physics D: Applied Physics*, 2009, 42, 035305.

107.   Atuchin, V. V., Gavrilova, T. A., Grivel, J. C., Kesler, V. G. and Troitskaia, I. B., *J Solid State Chem*.

108.   Atuchin, V. V., Grivel, J. C. and Zhang, Z., *Chemical Physics*, 2009, 360, 74-78.

109.   Rouahi, A., Kahouli, A., Challali, F., Besland, M. P., Vallee, C., Pairis, S., Yangui, B., Salimy, S., Goullet, A. and Sylvestre, A., *J. Appl. Phys.*, 2012, 112, 094104.

110.   Wang, Y. M. and Yu, R. C., *Phys. Status Solidi A-Appl. Mat.*, 2009, 206, 31-35.

111.   Retoux, R., Rodriguez-Carvajal, J. and Lacorre, P., *J Solid State Chem*, 1998, 140, 307-315.

112.   Yan, H., Reece, M. J., Liu, J., Shen, Z., Kan, Y. and Wang, P., *J. Appl. Phys.*, 2006, 100, 076103.

113. Moulder, J. F., Stickle, W. F., Sobol, P. E. and Bomben, K. D., *Physical Electronics Inc*, 1995, 213.

114. Jovalekić, Č., Pavlović, M., Osmokrović, P. and Atanasoska, L., *Applied Physics Letters*, 1998, 72, 1051-1053.

115. Park, B. H., Hyun, S. J., Bu, S. D., Noh, T. W., Lee, J., Kim, H.-D., Kim, T. H. and Jo, W., *Applied Physics Letters*, 1999, 74, 1907-1909.

116. Chu, M.-W., Ganne, M., Caldes, M. T. and Brohan, L., *J. Appl. Phys.*, 2002, 91, 3178-3187.

117. O'Mahony, L., Curtin, T., Zemlyanov, D., Mihov, M. and Hodnett, B. K., *Journal of Catalysis*, 2004, 227, 270-281.

118. Hu, W. B., Liu, Y., Withers, R. L., Frankcombe, T. J., Noren, L., Snashall, A., Kitchin, M., Smith, P., Gong, B., Chen, H., Schiemer, J., Brink, F. and Wong-Leung, J., *Nat. Mater.*, 2013, 12, 821-826.

119. Yan, H., Fawad, I., Giuseppe, V., Ning, H., Zhang, H., Jiang, Q., Zeng, T., Gao, Z. and Reece, M., *Journal of Advanced Dielectrics*, 2011, 1, 107-118.

120. Shimakawa, Y., Kubo, Y., Nakagawa, Y., Goto, S., Kamiyama, T., Asano, H. and Izumi, F., *Phys Rev B*, 2000, 61, 6559-6564.

121. Atuchin, V. V., Kalabin, I. E., Kesler, V. G. and Pervukhina, N. V., *Journal of Electron Spectroscopy and Related Phenomena*, 2005, 142, 129-134.

122. Atuchin, V. V., Kesler, V. G., Pervukhina, N. V. and Zhang, Z., *Journal of Electron Spectroscopy and Related Phenomena*, 2006, 152, 18-24.

123. Wang, L., Ma, W., Fang, Y., Zhang, Y., Jia, M., Li, R. and Huang, Y., *Procedia Environmental Sciences*, 2013, 18, 547-558.

124. Jehng, J. M. and Wachs, I. E., *Chemistry of Materials*, 1991, 3, 100-107.

125. Gupta, H. C., Archana and Luthra, V., *Vibrational Spectroscopy*, 2011, 56, 235-240.

126. Verma, M., Sreenivas, K. and Gupta, V., *J. Appl. Phys.*, 2009, 105, 024511.

127. Volanti, D. P., Cavalcante, L. S., Paris, E. C., Simoes, A. Z., Keyson, D., Longo, V. M., Figueiredo, A. T. d., Longo, E., Varela, J. A., Vicente, F. S. D. and Hernandes, A. C., *Applied Physics Letters*, 2007, 90, 261913.

128. Gallagher, P. K., O'Bryan, H. M. and Brandle, C. D., *Thermochimica Acta*, 1988, 133, 1-10.

129. Chen, C., Ning, H., Lepadatu, S., Cain, M., Yan, H. and Reece, M. J., *J. Mater. Chem. C*, 2015, 3, 19-22.

130. Chen, C., Jiang, Q., Wei, X., Abrahams, I., Yan, H. and Reece, M. J., *Journal of the American Ceramic Society*, 2014, 97, 3624-3630.